学 位 論 文

A study of aerosol properties on global scale using satellite remote sensing

(衛星リモートセンシングによるエアロゾル特性の全球解析)

平成 9 年 12 月　博士 (理学) 申請

東 京 大 学 理 学 系 研 究 科
地 球 惑 星 物 理 学 専 攻

日　暮　明　子

Contents

Acknowledgment

Chapter 1

General Introduction

1 General Introduction

Aerosols play an important role in formation of the earth's climate, for they significantly affect the fraction of the solar incidence at the top of the atmosphere reaching the earth's surface and the fraction of the thermal radiation escaping to the space. The direct and indirect effects of aerosols on the climate are estimated about -0.5 and -1.5 W/m^2, respectively, indicating the magnitude of the total aerosol forcing is almost comparable but opposite to the sign of the effect of greenhouse gases, i.e., 2.5 W/m^2 (IPCC95, 1996). These effects, however, don't cancel each other and will generate a complex impact on the atmospheric circulation (Mitchell et al., 1995; Santer et al., 1996), since aerosols are distributed unevenly in the atmosphere.

Early studies of the aerosol direct forcing have focused on anthropogenic sulfate aerosols, which will cause a large cooling effect due to its high light-scattering efficiency (Charlson et al, 1992; Kiehl and Briegleb, 1993; Taylor and Penner, 1994). The strong spatial and temporal variations of aerosol distributions are, however, not only in concentrations but also in compositions, and besides, with their different radiative properties. Therefore, we have to pay attention to the positive radiative forcing of strongly absorbing aerosols, such as dust and soot, even though the direct radiative forcing of aerosols is generally believed to be controlled by non-absorbing sulfate aerosols which cause a significant cooling effect. With this recognition, recent attention has been paid to the radiative effects of mineral dust, especially anthropogenically generated mineral dust, i.e., originating from land-use change (Tegen et al, 1996; Li et al., 1996; Sokolik and Toon, 1996). The radiative effects of mineral dust are important relative to those of other aerosols due to their widespread distribution and large optical thickness. Estimations of their direct radiative forcing, however, still have a large uncertainty of a factor of 2-3 or more, due to lack of our knowledge about the spatial and temporal distributions of aerosol optical properties. Furthermore, the effect of aerosol-cloud interaction remains scarcely known, with very few satellite studies (Twomey et al., 1984; Kaufman and Nakajima, 1993).

To understand these complex climate effects of natural and anthropogenic aerosols,

their geophysical properties, such as concentration, composition, optical and physical properties, have to be well studied. The aerosol monitoring on global scale with satellite data will be the most powerful tool for this purpose. Although ground based measurements are also important to obtain the detailed optical and physical properties of aerosols, it will be difficult to evaluate the global aerosol characteristics from the ground-based measurement data, because of strong spatial and temporal variations in aerosol distributions. Present satellite measurements of aerosols are, however, mostly limited to estimation of the aerosol optical thickness, which corresponds to the column total cross section, from reflectance in one or two channels of geostationary, e.g., Meteosat, or polar orbiter satellites, e.g., NOAA / AVHRR (Stowe et al, 1992; Durkee et al., 1991; Moulin et al., 1997). If we consider the radiative transfer process in an aerosol-laden atmosphere, it is found that aerosol properties have to be described by optical thickness, size distribution, and complex refractive index in most applications. In these satellite-retrieval algorithms, therefore, aerosol parameters other than optical thickness, such as size distribution and complex refractive index, are prefixed at a typical value before starting retrievals. Since there are large variabilities in aerosol characteristics as mentioned above, such an assumption of the aerosol size distribution and refractive index, and corresponding scattering phase function, generates a large error in the derived aerosol optical thickness (Ignatov et al., 1995).

Several multi-channel satellite-borne sensors, such as ADEOS / OCTS, SeaWiFS, EOS / MODIS, ADEOS-II / GLI have been launched recently or are planned to be launched in near future. A use of spectral radiance data provided by those sensors could lead to estimating more aerosol optical parameters and, at the same time, to realizing more accurate retrieval of aerosol optical thickness. Data analyses of NOAA / AVHRR are also interesting even with only two channels in visible and near-infrared spectral regions, since there are data records of more than ten years, which are extremely valuable for researches of the climatological impact of aerosols.

Being motivated by the above mentioned situation of aerosol remote sensing, we have developed an aerosol retrieval algorithm with two channel radiance data. Although our two channel algorithm can be applied to any of recent multi-channel satellite-borne radiometers, it will be the most unique benefit that our algorithm can be applied to the long-term data of the AVHRR radiometer on board the NOAA polar orbiter series. For this purpose we have

made an intensive effort for interpreting AVHRR-received radiances, which include complicated effects of aerosols, gases and geometries due to its large band widths. To our knowledge our algorithm is the first two channel algorithm in the history which can suitably retrieve the aerosol optical thickness and a size index, i.e. Ångström exponent, although there are on-going several projects in the world for developing a similar algorithm.

This thesis is organized as follows. Chapter 2 summarizes the radiative transfer theory used in this thesis.

The paper entitled "A study on synthesizing satellite-received radiances for aerosol and ocean color remote sensing" by A. Higurashi, T. Nakajima and T. Tanaka, which is being submitted to *Appl. Opt.*, is put in chapter 3. In the chapter 3, the structure of the radiance field in the atmosphere-ocean surface system is discussed in detail with the knowledge of radiative transfer processes and we present a new technique for synthesizing satellite-received radiances accurately and efficiently for aerosol remote sensing.

In chapter 4, the paper entitled "Development of a two channel aerosol retrieval algorithm on global scale using NOAA / AVHRR" by A. Higurashi and T. Nakajima (in press, *J. Atmos. Sci.*) is presented. Estimation of the aerosol optical thickness and Ångström exponent from two channel radiances is discussed and an algorithm for global aerosol monitoring is developed, using the synthesizing method developed in chapter 3. Retrieved global distributions of aerosol optical thickness and Ångström exponent in 10 days of January and of July 1988 are shown as a preliminary result.

The paper entitled "A global characterization of aerosols with a two channel remote sensing" by A. Higurashi and T. Nakajima, which is being submitted to *J. Clim.*, is presented in chapter 5. The algorithm developed in chapter 4 is applied to NOAA-11 / AVHRR data for four months in 1990 and retrieval results are fully investigated in detail along with ground-based sunphotometry data for validation. It is found that a tuning of parameters for size distribution and sensor calibration is needed to reproduce small Ångström exponents for mineral dust aerosols. The retrieved distributions of aerosol optical thickness and Ångström exponent became more realistic as compared with the 10 day retrievals obtained in chapter 4.

Finally, a general conclusion is given in chapter 6.

References

Charlson, R. J., S. E. Schwartz, J. M. Hales, R. D. Cess, J. A. Coakley, Jr., J. E. Hansen, and D. J. Hofmann, 1992: Climate forcing by anthropogenic aerosols. *Science*, **255**, 423-430.

Durkee, P. A., F. Pfeil, E. Frost and R. Shema, 1991: Global analysis of aerosol particle characteristics. *Atmos. Environ*, **25A**, 2457-2471.

Ignatov, A. M., L. L. Stowe, S. M. Sakerin, and G. K. Korotaev, 1995: Validation of the NOAA/ NESDIS satellite aerosol product over the North Atlantic in 1989. *J. Geophys. Res.*, **100**, 5123-5132.

IPCC95, Climate Change 1995, 1996: The Science of Climate Change. Eds. J. T. Houghton et al., Cambridge Univ. Press.

Kaufman, Y. J., and T. Nakajima, 1993: Effect of Amazon Smoke on Cloud Microphysics and Albedo - Analysis from Satellite Imagery. *J. Appl. Meteor.*, **32**, 729-744.

Kiehl, J. T., and B. P. Briegleb, 1993: The relative roles of sulfate aerosols and greenhouse gases in climate forcing. *Science*, **260**, 311-314.

Li, X., H. Maring, D. Savoie, K. Voss, and J. M. Prospero, 1996: Dominance of mineral dust in aerosol light-scattering in the North Atlantic trade winds. *Nature*, **380**, 416-419.

Mitchell, J. F. B., T. C. Johns, J. M. Gregory, and S. F. B. Tett, 1995: Climate response to increasing levels of greenhouse gases and sulphate aerosols. *Nature*, **376**, 501-504.

Moulin, C., F. Dulac, C. E. Lambert, P. Chazette, I. Jankowiak, B. Chatenet, and F. Lavenu, 1997: Long-term daily monitoring of Saharan dust load over ocean using Meteosat ISCCP-B2 data 2. Accuracy of the method and validation using sun photometer measurements. *J. Geophys. Res.*, **102**, 16959-16969.

Santer, B. D., K. E. Taylor, T. M. L. Wigley, T. C. Johns, P. D. Jones, D. J. Karoly, J. F. B. Mitchell, A. H. Oort, J. E. Penner, V. Ramaswamy, M. D. Schwarzkopf, R. J. Stouffer, and S. Tett, 1996: A Search for Human Influences on the Thermal Structure of the Atmosphere. *Nature*, **382**, 39-46.

Sokolik, I. N., and O. B. Toon, 1996: Direct radiative forcing by anthropogenic airborne mineral aerosol. *Nature*, **381**, 681-683.

Stowe, L. L., R. M. Cavoy, and P. P. Pelliguino, 1992: Monitoring the Mt. Pinatubo aerosol layer with NOAA-11/AVHRR data. *Geophys. Res. Lett*, **19**, 159-162.

Taylor, K. E., and J. E. Penner, 1994: Response of the climate system to atmospheric aerosols and greenhouse gases. *Nature*, **369**, 734-737.

Tegen, I., A. A. Lacis, and I. Fung, 1996: The influence on climate forcing of mineral aerosols from disturbed soils. *Nature*, **380**, 419-422.

Twomey, S. A., M. Piepgrass and T. L. Wolfe, 1984: An assessment of the impact of pollution on global cloud albedo. *Tellus*, **36B**, 356-366.

Chapter 2

Radiative Transfer Code

2 Radiative Transfer Code

The state of polarization, i. e., the degree of polarization, the plane of polarization, and the ellipticity of the radiation, is not generally included in the description of the radiation field. This is because impacts of the polarization on radiances are not significant in most cases, whereas computing the polarization field takes much time as compared with the scaler field case. There are, however, several applications that do not allow such a simplification. Therefore, we used in this thesis two different radiative transfer codes, i. e., *Rstar-5b* and *Pstar-1b*, depending appropriately on each situation. *Rstar-5b* is a general radiative transfer code developed by CCSR (Center for Climate System Research), Univ. of Tokyo, which solves the scalar radiative transfer with a combined discrete - ordinate / matrix - operator method taking into account the multiple scattering in the atmosphere (Nakajima and Tanaka, 1986; 1988), gaseous absorption with Lowtran-7 absorption model (Kneizys et al., 1988), and the ocean surface reflection by the rough ocean algorithm (Nakajima and Tanaka, 1983), but without polarization effects. *Pstar-1b* has been developed for calculating polarized radiation field, expanding *Rstar-5b* with a matirix operator method. In this chapter, we briefly summerize the radiative transfer calculation, especially by *Pstar-1b*, used in this thesis.

2. 1 The Radiative transfer equation in a polarized field

For describing the state of polarization, we start with the electric field representation as,

$$\begin{bmatrix} E_r \\ E_l \end{bmatrix} = \begin{bmatrix} E_{0r} \exp\left[i(\omega t - \varepsilon_r)\right] \\ E_{0l} \exp\left[i(\omega t - \varepsilon_l)\right] \end{bmatrix}, \tag{1}$$

where E_r and E_l are the components of the vibration along two directions, which are the vertical and horizontal to the scattering plane, respectively, ω is the circular frequency of the vibration, t is a time, and E_{0r}, E_{0l}, ε_r, and ε_l are constants, Stokes parameters are defined by,

$$I_r \equiv E_{0r}^2, \quad I_l \equiv E_{0l}^2, \quad U \equiv 2E_{0r}E_{0l}\cos(\varepsilon_l - \varepsilon_r), \quad V \equiv 2E_{0r}E_{0l}\sin(\varepsilon_l - \varepsilon_r), \tag{2}$$

or

$$I_r \equiv |E_r|^2, \quad I_l \equiv |E_l|^2, \quad U + iV \equiv 2E_l^* E_r, \tag{3}$$

where an asterisk denotes the conjugate complex value. In an alternative system, $I = I_l + I_r$ and $Q = I_l - I_r$ are used instead of I_l and I_r. Denoting the incident light by a vector,

$$\mathbf{I} = (I, Q, U, V), \tag{4}$$

the equation of radiative transfer for a plane-parallel atmosphere can be written as

$$\mu \frac{d\mathbf{I}(\tau, \mu, \phi)}{d\tau} = -\mathbf{I}(\tau, \mu, \phi) + \omega \int_{4\pi} d\mu' d\phi' \mathbf{P}(\mu, \phi; \mu', \phi') \mathbf{I}(\tau, \mu', \phi') + [1 - \omega]\mathbf{B}(T), \tag{5}$$

where τ shows the optical depth measured from the atmospheric top, ω is the single scattering albedo of the air mass, μ and ϕ are cosine of the zenith angle and the azimuth angle, respectively, and the contribution of thermal emission $\mathbf{B}(T)$ is expressed as follows,

$$\mathbf{B}(T) = (B(T), 0, 0, 0), \tag{6}$$

where $B(T)$ indicates the plank function at the temperature T. And, the phase matrix $\mathbf{P}(\mu, \phi; \mu', \phi')$ is given by

$$\mathbf{P}(\mu, \phi; \mu', \phi') = \mathbf{C}(-\chi)\tilde{\mathbf{P}}(\Theta)\mathbf{C}(\chi'). \tag{7}$$

where $\tilde{\mathbf{P}}(\Theta)$ is the phase matrix for the scattering angle Θ referred to the scattering plane, and $\mathbf{C}(\chi')$ and $\mathbf{C}(-\chi)$ show the transformation of the axes through angles χ' and $-\chi$, respectively, in the clockwise direction (see Fig. 1 for the definition of angles). For example, $\mathbf{C}(\chi')$ is given as follows,

8
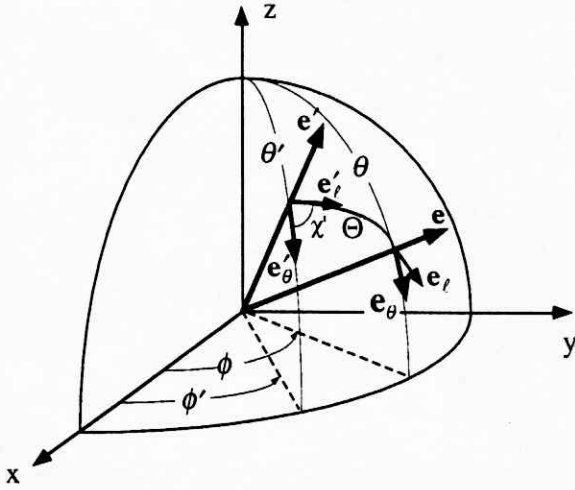
Fig. 1   Coordiante systems

$$C(\chi') = \begin{bmatrix} 1 & 0 & 0 & 0 \\ 0 & \cos 2\chi' & -\sin 2\chi' & 0 \\ 0 & \sin 2\chi' & \cos 2\chi' & 0 \\ 0 & 0 & 0 & 1 \end{bmatrix}. \tag{8}$$

χ' is the angle between the meridian plane including the incident vector $\mathbf{e}'$ and the scattering plane; χ is the angle between the scattering plane and the meridian plane including the emitted vector. Hence we have the following equations to relate those angular variables,

$$\cos \chi = \frac{\cos \theta' - \cos \theta \cos \Theta}{\sin \theta \sin \Theta}, \quad \cos \chi' = -\frac{\cos \theta - \cos \theta' \cos \Theta}{\sin \theta' \sin \Theta}, \tag{9}$$

$$\sin \chi = \sin \theta' \frac{\sin(\phi - \phi')}{\sin \Theta}, \quad \sin \chi' = \sin \theta \frac{\sin(\phi - \phi')}{\sin \Theta}, \tag{10}$$

$$\cos \Theta = \cos \theta \cos \theta' + \sin \theta \sin \theta' \cos(\phi - \phi'). \tag{11}$$

In order to solve Eq. (5), it is important to study the symmetric properties of $\mathbf{I}$ and $\mathbf{P}$ with respect to operations around the vertical plane, We consider two conditions; one is the ' mirroring', in which the coordinate system is mirrored with respect to the meridian plane,

9

another is the 'positioning', in which incident vector **e** and emitted vector **e´** are positioned at $-\phi$ and $-\phi'$, respectively. If there is the symmetry with respect to ϕ, description of these phenomena should be same in both conditions. Denoting a scattering process by

$$\begin{bmatrix} E_r \\ E_l \end{bmatrix} = \frac{e^{-ikr}}{ikr} \begin{bmatrix} S_{11} & S_{12} \\ S_{21} & S_{22} \end{bmatrix} \begin{bmatrix} E_{0r} \\ E_{0l} \end{bmatrix}, \tag{12}$$

in the 'mirroring' and the ' positioning' systems, the scattering phenomenon is written as

$$\begin{bmatrix} mirror(E_r) \\ mirror(E_l) \end{bmatrix} = \frac{e^{-ikr}}{ikr} \begin{bmatrix} S_{11} & S_{12} \\ S_{21} & S_{22} \end{bmatrix} \begin{bmatrix} mirror(E_{0r}) \\ mirror(E_{0l}) \end{bmatrix}, \tag{13}$$

and

$$\begin{bmatrix} pos(E_r) \\ pos(E_l) \end{bmatrix} = \frac{e^{-ikr}}{ikr} \begin{bmatrix} S_{11} & -S_{12} \\ -S_{21} & S_{22} \end{bmatrix} \begin{bmatrix} pos(E_{0r}) \\ pos(E_{0l}) \end{bmatrix}, \tag{14}$$

respectively. From these equations, **P** in both systems are related by

$$pos(\mathbf{P}) = \mathbf{Q}[mirror(\mathbf{P})]\mathbf{Q}, \tag{15}$$

where **Q** is given by

$$\mathbf{Q} = \begin{bmatrix} 1 & 0 & 0 & 0 \\ 0 & 1 & 0 & 0 \\ 0 & 0 & -1 & 0 \\ 0 & 0 & 0 & -1 \end{bmatrix}. \tag{16}$$

Equation (15) indicates that the top left and bottom right fourth parts of **P** are even-functions of ϕ and others are odd-functions of ϕ. The symmetric properties of the Stokes parameters are similarly shown as follows,

$$mirror(I) = pos(I), \qquad mirror(Q) = pos(Q),$$
$$mirror(U) = -pos(U), \quad mirror(V) = -pos(V) \text{'}$$
<div style="text-align: right">(17)</div>

i. e. , first two elements of the Stokes parameters are even-functions of ϕ and others are odd-functions.

Expanding **I** and **P** with Fourier series regarding ϕ as,

$$\mathbf{I}(\tau;\mu,\phi) = \sum_{m=0}^{\infty} \left[\mathbf{I}_c^{(m)}(\tau;\mu) \frac{\cos m(\phi - \phi_0)}{\pi(1 + \delta_{0,m})} + \mathbf{I}_s^{(m)}(\tau;\mu) \frac{\sin m(\phi - \phi_0)}{\pi(1 + \delta_{0,m})} \right],$$
<div style="text-align: right">(18)</div>

$$\mathbf{P}(\mu,\phi;\mu',\phi') = \sum_{m=0}^{\infty} \left[\mathbf{P}_c^{(m)}(\mu;\mu') \frac{\cos m(\phi - \phi')}{\pi(1 + \delta_{0,m})} + \mathbf{P}_s^{(m)}(\mu;\mu') \frac{\sin m(\phi - \phi')}{\pi(1 + \delta_{0,m})} \right],$$
<div style="text-align: right">(19)</div>

Eq. (5) splits into the following independent equations,

$$\mu \frac{d}{d\tau} \mathbf{I}_c^{(m)}(\tau,\mu) = -\mathbf{I}_c^{(m)}(\tau,\mu) + 2\pi\delta_{0,m}[1 - \omega]\mathbf{B}(T)$$
$$+\omega \int_{-1}^{1} \left[\mathbf{P}_c^{(m)}(\mu;\mu')\mathbf{I}_c^{(m)}(\tau,\mu') - \mathbf{P}_s^{(m)}(\mu;\mu')\mathbf{I}_s^{(m)}(\tau,\mu') \right] d\mu',$$
<div style="text-align: right">(20)</div>

and

$$\mu \frac{d}{d\tau} \mathbf{I}_s^{(m)}(\tau,\mu) = -\mathbf{I}_s^{(m)}(\tau,\mu)$$
$$+\omega \int_{-1}^{1} \left[\mathbf{P}_c^{(m)}(\mu;\mu')\mathbf{I}_s^{(m)}(\tau,\mu') + \mathbf{P}_s^{(m)}(\mu;\mu')\mathbf{I}_c^{(m)}(\tau,\mu') \right] d\mu'.$$
<div style="text-align: right">(21)</div>

For the symmetic properties of **I** and **P** with respect to ϕ mentioned above, it is convenient to define $\mathbf{I}^{(m)}$ and $\mathbf{P}^{(m)}$ by

$$\mathbf{I}^{(m)}(\tau;\mu) = \mathbf{I}_c^{(m)}(\tau;\mu) + \mathbf{I}_s^{(m)}(\tau;\mu),$$
<div style="text-align: right">(22)</div>

and

11

$$\mathbf{P}^{(m)}(\mu,\mu') = \mathbf{P}_c^{(m)}(\mu,\mu') + \mathbf{P}_s^{(m)}(\mu,\mu')\mathbf{Q}.$$ (23)

Finally the equation of the radiative transfer for the polarized field can be written in the form

$$\mu\frac{d}{d\tau}\mathbf{I}^{(m)}(\tau,\mu) = -\mathbf{I}^{(m)}(\tau,\mu) + \omega\int_{-1}^{1}\mathbf{P}^{(m)}(\mu;\mu')\mathbf{I}^{(m)}(\tau,\mu')d\mu'$$

$$+2\pi\delta_{0,m}[1-\omega]\mathbf{B}(T).$$ (24)

From such consideration, we can treat the radiative transfer of the polarization field in the same way as the scaler transfer case. In *Pstar*-1b, the equation of the radiative transfer is solved with a doubling-adding method (Wiscombe, 1976), in which a solution of the second order scattering is adopted as an initial solution.

2. 2 The reflection and transmission matrices of the rough ocean surface

The reflection and transmission matrices of the rough ocean surface can be written as an extension of the rough ocean model by Nakajima and Tanaka (1983) as,

$$\tilde{\mathbf{R}}(\mu,\phi;\mu',\phi') = \frac{1}{4\mu_n\mu}G(v,v')p(\mu_n)\tilde{\mathbf{r}}(\cos\beta,\tilde{m}),$$ (25)

$$\tilde{\mathbf{T}}(\mu,\phi;\mu',\phi') = \frac{\tilde{m}^2\cos^2\beta_t}{\mu\mu_n(\cos\beta - \tilde{m}\cos\beta_t)^2}G(v,v')p(\mu_n)\tilde{\mathbf{t}}(\cos\beta,\tilde{m})$$

$$\times H((\tilde{m}-1)(\tilde{m}\mu-\mu'))H(\alpha-1/m),$$ (26)

where μ_n is the cosine of the zenith angle of the surface normal vector, β, β_t, and $\tilde{m}$ indicate incident and emergent angles with respect to the surface and the relative complex refractive index of the ocean to the atmosphere, respectively, and they are related as follows,

$$\sin\beta = \tilde{m}\sin\beta_t,$$ (27)

12

$$\cos\beta_t = \frac{1}{\tilde{m}}\sqrt{\tilde{m}^2 - \sin^2\beta}\,, \tag{28}$$

p is the density function of the wave slope given by

$$p(\mu_n) \equiv \frac{1}{\pi\sigma^2\mu_n^3}\exp\left(-\frac{1-\mu_n^2}{\sigma^2\mu_n^2}\right), \tag{29}$$

$$\sigma^2 = 0.00534u_{10}, \tag{30}$$

where u_{10} is the surface wind velocity at 10 m height above the ocean surface, G and H, which are introduced to express the shadowing effects by wave facets, are give as follows,

$$G(v,v') = \frac{1}{1 + F(v) + F(v')}, \tag{31}$$

$$F(v) = \frac{1}{2}\left[\frac{\exp(-v^2)}{\sqrt{\pi}v^2} - \frac{2}{\sqrt{\pi}}\int_0^\infty e^{t^2}\,dt\right], \tag{32}$$

$$v = \frac{\mu}{\sigma\sqrt{1-\mu^2}}, \quad v' = \frac{\mu'}{\sigma\sqrt{1-\mu'^2}}, \tag{33}$$

and

$$\alpha = \mu\mu' + \sqrt{1-\mu^2}\sqrt{1-\mu'^2}\cos(\phi-\phi'), \tag{34}$$

$\tilde{r}$ and $\tilde{t}$ are the Fresnel's reflection and transmission matrices given as follows:

if $\tilde{m} > 1$ or $\tilde{m} < 1$ and $\beta < \beta_c$, $\beta > \beta_c$, where $\sin\beta_c = \tilde{m}$,

$$\tilde{r}(\cos\beta,\tilde{m}) = \begin{bmatrix} r_\parallel^2 & 0 & 0 & 0 \\ 0 & r_\perp^2 & 0 & 0 \\ 0 & 0 & r_\parallel r_\perp & 0 \\ 0 & 0 & 0 & r_\parallel r_\perp \end{bmatrix}, \tag{35}$$

13

$$r_\| = \frac{\tilde{m}^2 \cos\beta - \sqrt{\tilde{m}^2 - \sin^2\beta}}{\tilde{m}^2 \cos\beta + \sqrt{\tilde{m}^2 - \sin^2\beta}}, \quad r_\perp = \frac{\cos\beta - \sqrt{\tilde{m}^2 - \sin^2\beta}}{\cos\beta + \sqrt{\tilde{m}^2 - \sin^2\beta}}, \tag{36}$$

$$\tilde{t}(\cos\beta, \tilde{m}) = \begin{bmatrix} \tilde{m}t_\|^2 & 0 & 0 & 0 \\ 0 & \tilde{m}t_\perp^2 & 0 & 0 \\ 0 & 0 & \tilde{m}t_\| t_\perp & 0 \\ 0 & 0 & 0 & \tilde{m}t_\| t_\perp \end{bmatrix}, \tag{37}$$

$$t_\| = \frac{2\tilde{m}\cos\beta}{\tilde{m}^2 \cos\beta + \sqrt{\tilde{m}^2 - \sin^2\beta}}, \text{ and } t_\perp = \frac{2\cos\beta}{\cos\beta + \sqrt{\tilde{m}^2 - \sin^2\beta}}, \tag{38}$$

and if $\tilde{m} < 1$ and $\beta > \beta_c$,

$$\tilde{r}(\cos\beta, \tilde{m}) = \begin{bmatrix} 1 & 0 & 0 & 0 \\ 0 & 1 & 0 & 0 \\ 0 & 0 & \cos(\delta_\perp - \delta_\|) & -\sin(\delta_\perp - \delta_\|) \\ 0 & 0 & \sin(\delta_\perp - \delta_\|) & \cos(\delta_\perp - \delta_\|)_\perp \end{bmatrix}, \tag{39}$$

$$\cos\frac{\delta}{2} = (1 - \tilde{m}^2)\sin^2\beta, \quad \sin\frac{\delta}{2} = (1 - \tilde{m}^2)\cos\beta\sqrt{|\tilde{m}^2 - \sin^2\beta|}, \tag{40}$$

and

$$\tilde{t}(\cos\beta, \tilde{m}) = 0. \tag{41}$$

Note these are in the (I_r, I_p, Q, U)-system.

Since the reflection and transmission by a rough ocean surface mentioned above are expressed in the coordinate system on a wave face, it is necessary to operate the rotation matrix on Eqs. (25) and (26) similar to Eq. (7) for the earth's coordinate system. Finally, the reflection and transmission matrix of the rough ocean surface are represented by

$$\mathbf{R}(\mu,\phi;\mu',\phi') = \hat{\mathbf{C}}(-\chi)\tilde{\mathbf{R}}(\mu,\phi;\mu',\phi')\hat{\mathbf{C}}(\chi'), \tag{42}$$

and

14

$$\mathbf{T}(\mu,\phi;\mu',\phi') = \hat{\mathbf{C}}(-\chi)\tilde{\mathbf{T}}(\mu,\phi;\mu',\phi')\hat{\mathbf{C}}(\chi'), \tag{43}$$

where $\hat{\mathbf{C}}(\chi')$ shows the transformation of axes through angles χ' as same as in Eq. (8), but for the (I_r, I_p, Q, U)-system, as given by

$$\hat{\mathbf{C}}(\chi') = \frac{1}{2}\begin{bmatrix} 2\cos^2\chi' & 2\sin^2\chi' & \sin 2\chi' & 0 \\ 2\sin^2\chi' & 2\cos^2\chi' & -\sin 2\chi' & 0 \\ -2\sin 2\chi' & 2\sin 2\chi' & 2\cos 2\chi' & 0 \\ 0 & 0 & 0 & 2 \end{bmatrix}. \tag{44}$$

2. 3 Truncation of the phase function

In *Rstar*-5b, the forward peak of the phase function is truncated by MS or TMS methods (Nakajima and Tanaka, 1988) in order to remove the strong forward scattering by Mie scattering which needs higher-order terms of the Fourier expansions in Eqs. (18) and (19) . In the same manner we have to truncate the forward peak in the polarization phase matrix. The phase matrix in the plane of the scattering by Mie scattering can be written as

$$\mathbf{P}(\Theta) = \begin{pmatrix} \frac{1}{2}(P_1 + P_2) & \frac{1}{2}(P_2 - P_1) & & \\ \frac{1}{2}(P_2 - P_1) & \frac{1}{2}(P_1 + P_2) & & \\ & & P_3 & P_4 \\ & & -P_4 & P_3 \end{pmatrix} = \begin{pmatrix} \overline{P_1} & \overline{P_2} & & \\ \overline{P_2} & \overline{P_1} & & \\ & & P_3 & P_4 \\ & & -P_4 & P_3 \end{pmatrix}. \tag{45}$$

It can be also decomposed as follows,

$$\mathbf{P}(\Theta) \equiv \mathbf{P}_d(\Theta) + \mathbf{P}_u(\Theta), \tag{46}$$

where $\mathbf{P}_d$ and $\mathbf{P}_u$ are given by

15

$$\mathbf{P}_d(\Theta) \equiv \begin{pmatrix} \overline{P_1} & & & \\ & \overline{P_1} & & \\ & & P_3 & \\ & & & P_3 \end{pmatrix}, \text{ and } \mathbf{P}_u(\Theta) = \begin{pmatrix} \overline{P_2} & & & \\ \overline{P_2} & & & \\ & & & P_4 \\ & & -P_4 & \end{pmatrix}. \tag{47}$$

We use the same truncation factor for all diagonal elements of the phase matrix, since diagonal elements take the same value at $\Theta = 0$. The truncation factor f is defined as follows,

$$f = 2\pi \int_{\Theta=0}^{\Theta'} \left[\overline{P_1} - (1-f')\overline{P_1}^* \right] d(\cos\Theta), \tag{48}$$

$$\overline{P_1}^* = \frac{1}{4\pi} \sum_{n=0}^{m^*} (2n+1) g_n^* p_n, \tag{49}$$

and

$$f' = g_{m+1}^*, \tag{50}$$

where g_n^* and p_n are the n-th order moment of the phase function and Legendre polynomial, respectively. Denoting $B(\Theta)$ by

$$B(\Theta) = \begin{cases} \overline{P_1}(\Theta) - (1-f')\overline{P_1}^*(\Theta) & 0 \le \Theta \le \Theta' \\ 0 & \Theta' \le \Theta \end{cases}, \tag{51}$$

the elements of the truncated phase matrix $\mathbf{P}_d^t$, $\overline{P_1}$ and P_3, can be written as

$$\overline{P_1}^t(\Theta) = \frac{\overline{P_1}(\Theta) - B(\Theta)}{1-f}, \tag{52}$$

and

$$P_3^t(\Theta) = \frac{P_3(\Theta) - B(\Theta)}{1-f}. \tag{53}$$

16

Finally the phase matrix is described as follows,

$$\mathbf{P}(\Theta) = f\delta(\Theta) + (1-f)\mathbf{P}_d'(\Theta) + \mathbf{P}_u(\Theta). \tag{54}$$

where $\mathbf{E}$ indicates a unit matrix. By such a treatment, the equation of the radiative transfer can be written as

$$\mu\frac{d\mathbf{I}(\tau,\mu,\phi)}{d\tau^*} = -\mathbf{I}(\tau,\mu,\phi) + \omega^* \int d\Omega' \mathbf{P}^*(\mu,\phi;\mu',\phi')\mathbf{I}(\tau,\mu',\phi'), \tag{55}$$

$$\mathbf{P}^*(\mu,\phi;\mu',\phi') = \mathbf{P}_d'(\mu,\phi;\mu',\phi') + \frac{1}{1-f}\mathbf{P}_u(\mu,\phi;\mu',\phi'), \tag{56}$$

$$\tau^* = (1-\omega f)\tau, \tag{57}$$

and

$$\omega^* = \frac{(1-f)\omega}{1-f\omega}. \tag{58}$$

Spliting Eq. (55) into the direct and the diffuse component, we can get following formulae,

$$\mathbf{I}_{direct} = \mathbf{F}_0 e^{-\frac{\tau^*}{\mu}}, \tag{59}$$

$$\mu\frac{d\mathbf{I}_{diffuse}}{d\tau^*} = -\mathbf{I}_{diffuse} + \omega^* \int d\Omega' \mathbf{P}^*(\Omega,\Omega')\mathbf{I}_{diffuse} + \omega^*\mathbf{P}^*(\Omega,\Omega_0)\mathbf{F}_0 e^{-\frac{\tau^*}{\mu}}, \tag{60}$$

where F_0 describe the extraterrestrial solar flux. Finally we solve Eq. (60) with adding/doubling techniques of the matrix operator method.

References

Kneizys, F. X., E. P. Shettle, L. W. Abreu, J. H. Chetwynd, G. P. Anderson, W. O. Gallery, J. E. A. Selby, and S. A. Clough, 1988: Users Guide to LOWTRAN 7. AFGL-TR-88-0177.

Nakajima, T., and M. Tanaka, 1983: Effect of wind-generated waves on the transfer of solar radiation in the atmosphere-ocean system. *J. Quant . Spectrosc. Radiat. Transfer* **29**, 521-537.

Nakajima, T., and M. Tanaka, 1986: Matrix formulations for the transfer of solar radiation in a plane-parallel scattering atmosphere. *J. Quant, Spectrosc. Radiat. Transfer* **35**, 13-21.

Nakajima, T., and M. Tanaka, 1988: Algorithms for radiative for intensity calculations in moderately thick atmospheres using a truncation approximation. *J. Quant . Spectrosc. Radiat. Transfer* **40**, 51-69.

Wiscombe, W. J., 1976: On initialization, error and flux conservation in the doubling method, *J. Quant. Spectrosc. Radiat. Transfer*, **16**, 637-658.

Chapter 3

A Study on Synthesizing Satellite-Received Radiances for Aerosol and Ocean Color Remote Sensing

3 A Study on Synthesizing Satellite-Received Radiances for Aerosol and Ocean Color Remote Sensing

ABSTRACT

A look-up table method for synthesizing satellite-received radiances, which is accurate and efficient, has been proposed on the basis of considerations to the structure of radiance fields in the atmosphere-ocean system. One of characteristics of the method is a decomposition of radiances at TOA into single and multiple scattering components, assuming the exact analytic single scattering solution, contrary to the decomposition in the traditional ocean color remote sensing algorithms in which a linearized single scattering approximation is used. The accuracy of synthesized aerosol multiple scattering radiances is significantly improved by an introduction of a small exponential term associated with the exact single scattering solution in addition to a polynomial function of aerosol optical thickness. Furthermore, a decomposition of radiances into contributions of Rayleigh scattering and specular reflection by a rough ocean surface significantly reduces the dependence of tabulated coefficient values on geophysical and angular parameters. The total error in synthesized satellite-received radiances as a result of all the parameterizations is less than 0.0005 in reflectance unit, that is accurate enough for most applications of aerosol and ocean color remote sensing.

3. 1 Introduction

Aerosol effects on climate is one of important subjects we have to study for understanding the earth's climate formation (e. g., Mitchell et al., 1995). According to the IPCC 1995 report, the direct effect of aerosols is estimated to be -0.5W/m^2 with factor of 2 uncertainties and the indirect effect to be in a range of 0 to -1.5W/m^2. Such large uncertainties in the estimation are caused by lack of our knowledge about aerosol properties on global scale. This situation has been rapidly changed, however, by the recent extensive uses of satellite data, which cover the whole earth on daily base, for aerosol remote sensing (Stowe et al., 1992; Huser et al., 1997; Moulin et al., 1997). In addition to the one channel algorithms,

multi-channel algorithms also have been developed for increasing the detection ability of aerosols (Herman et al., 1997; Durkee et al., 1991;Higurashi and Nakajima, 1997).

Those progresses in aerosol remote sensing will need elaborate yet efficient interpretation of satellite-received spectral radiances by theoretical calculations. Especially, studying an efficient expression for the angular dependence of satellite-received radiances is important for optically thin aerosol-laden atmospheres. This subject is also important for the atmospheric correction for ocean color remote sensing as considered in early studies (Gordon et al., 1983; Wang and Gordon, 1993).

Studies on synthesizing techniques of satellite-received radiances will become important more and more for remote sensing of aerosol and ocean color with increasing volume of spectral radiance data. Next generation satellite-borne radiometers, such as EOS-AM1 / MODIS (MODerate resolution Imaging Spectroradiometer) and ADEOS2 (ADvanced Earth Observing Satellite) / GLI (GLobal Imager), will carry 36 channels with a spatial resolution of 250 m to 1km. The data volume of those radiometers are six to ten times larger than that of ADEOS / OCTS (Ocean Color and Temperature Scanner). At the same time, the sensitivity of the radiometer is increased significantly, so that the accuracy of synthesized radiances with a look-up table (LUT) method also has to be increased. The required accuracy of synthesized apparent reflectances for AVHRR, OCTS and SeaWiFS is the order of 0.001 with 10 bit A/D coverters. MODIS and GLI need more accuracy with their 12 bit A/D converters.

In this paper, we reconsider the structure of the radiance field in the atmosphere - ocean surface system with the physical consideration of radiative transfer processes and present a new method for synthesizing satellite-received radiances efficiently for aerosol remote sensing over the ocean.

3. 2 Structure of the radiance field in atmosphere- ocean system

We begin with the definition of the apparent reflectance R:

$$R = \frac{\pi L}{\mu_0 F}, \tag{1}$$

where L is the radiance, μ_0 is the cosine of the solar zenith angle θ_0, and F_0 is the extraterrestrial solar flux. The satellite-received radiance over the ocean R_t, consists of the contribution from Rayleigh scattering R_r, scattering by aerosols in the atmosphere R_a, the direct solar radiation specularly reflected from a rough ocean surface (sun glitter) R_g, the reflection by form R_f, and the ocean-leaving radiance R_w,

$$R_t = R_r + R_a + R_g + R_f + R_w. \tag{2}$$

3. 2. 1 Atmospheric radiance

In Eq. (2), the Rayleigh scattering component is easily synthesized by a three-term Fourier sum as (Chandrasekhar, 1949),

$$R_r = \sum_{m=0}^{2} R_r^{(m)} \cos m\phi, \tag{3}$$

where ϕ is the relative azimuth angle and m shows the fourier order. In the ocean color remote sensing algorithms (Gordon et al.,1983; Wang and Gordon, 1993), the aerosol scattering component has been synthesized with a linearized single scattering approximation $R_{a,ls}$, or its second order polynomial as,

$$R_a = R - R_r = \sum_{n=0}^{2} a_n R_{a,ls}^n, \tag{4}$$

where $R_{a,ls}$ is defined by a linear function of the aerosol optical thickness,

$$R_{a,ls} = \frac{\pi \omega_a \tau_a P_a}{\mu \mu_0}, \tag{5}$$

where ω_a, τ_a, and P_a show the aerosol single scattering albedo, optical thickness and scattering phase function, respectively, and μ is the cosine of the satellite zenith angle θ. Wang and Gordon (1993) found that the multiple scattering by aerosols is almost proportional to the linearized single scattering component, so that the first two terms of the r.h.s of Eq. (4) can

22

explain most of radiances due to aerosol scattering. The second order term in Eq. (4) becomes important for cases of absorbing aerosols. In the operational algorithm of ADEOS / OCTS, the aerosol multiple scattering component $R_{a,m}$ is formulated by a polynomial function of τ_a combining Eqs. (4) and (5) as follows,

$$R_{a,m} = R_t - R_r - R_g - R_{a,ls} = \sum_{n=1}^{N} b_n \tau_a^n .$$ (6)

Compared with Eq. (4), this formula is more convenient for retrieving τ_a. Also it should be noted that the coefficients b_n, are expected to be a weaker function of angular parameters than a_n in Eq. (4), since the multiple scattering component has less angular dependence than $R_{a,ls}$. This feature is important when we discretize the angular dependence of the coefficients to make a LUT of the coefficients. The approximation Eq. (6) with $N = 3$ reproduces radiances accurately in most angular geometries as shown in Figs. 1(a) and (b), which indicate absolute error distributions in the apparent reflectance at the wavelength of 0.5μm for various θ and θ_0, ranging from 0° to 70°, at $\phi = 0°$ (Fig. 1(a)), and for various θ and ϕ at $\theta_0 = 60°$ (Fig. 1(b)).

Calculations in Fig. 1 have been made by a general radiative transfer code, *RSTAR-5b*, which solves the radiative transfer with a combined discrete-ordinate / matrix-operator method
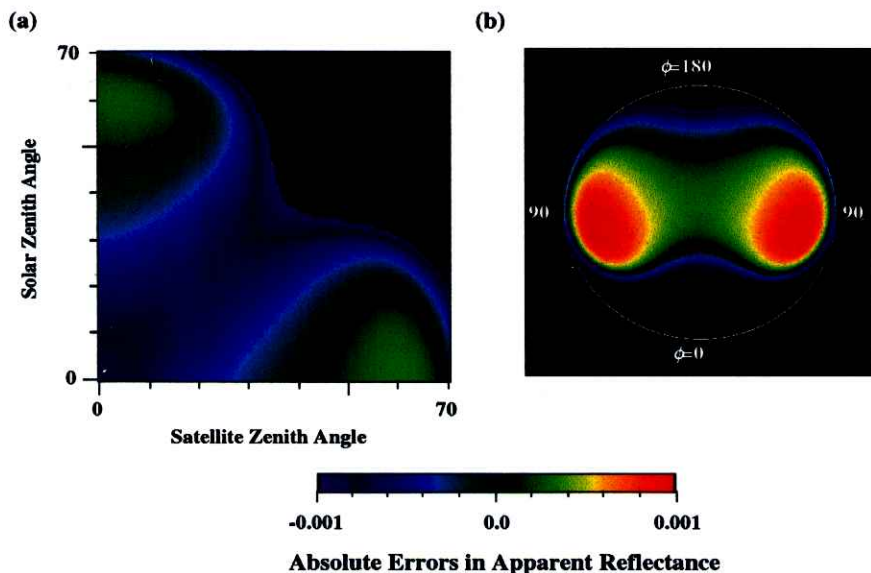

Fig. 1   Absolute errors in R_m synthesized by Eq. (6) with $N = 3$ and $\tau_a = 0.1$. A plot in (θ, θ_0)-plane with $\phi = 0°$ (a); a plot in (θ, ϕ)-plane with $\theta_0 = 60°$ (b).

taking into account the multiple scattering in the atmosphere (Nakajima and Tanaka, 1986; 1988), gaseous absorption with Lowtran-7 absorption model (Kneizys et al., 1988), and the ocean surface reflection calculated by the rough ocean algorithm of Nakajima and Tanaka (1983). In the calculations, we assumed a rough ocean surface with surface wind velocity at 10m height, u_{10}, of 7m/s. Note that the flat ocean surface is assumed in the operational algorithm for NIMBUS / CZCS (Coastal Zone Color Scanner) and OCTS. The US-standard atmosphere was assumed with a loading of Mie aerosols having a complex refractive index of 1.5-0.005i, aerosol optical thickness of 0.1, and bimodal size distribution as follows,

$$\frac{dV}{d\ln r} = \sum_{n=1}^{2} C_n \exp\left[-\frac{1}{2}\left(\frac{\ln r - \ln r_{m,n}}{\ln s_n}\right)^2\right],$$

(7)

where subscript n indicates the mode number and we adopt $r_{m.1} = 0.17$, $r_{m.2} = 3.44$, $s_1 = 1.96$, and $s_2 = 2.37$. Although the peak ratio, $\gamma(= C_2 / C_1)$ is a variable in the realistic atmosphere, we assumed $\gamma=1$ as a typical case.

It is found in Fig. 1 that the approximation Eq. (6) with $N = 3$ becomes worse rapidly with increasing θ and θ_0, and large errors exceeding ±0.001 appear in the region of

$$\theta + \theta_0 \geq 90°.$$

(8)

Numerical simulations have shown the large errors are caused by the introduction of the linearized single scattering component $R_{a,ls}$, in Eq. (6), because the angular dependence of $R_{a,ls}$ is not suitable for such large zenith angles. To improve the approximation for synthesizing the atmospheric path radiance, we propose to divide R_t, into single and multiple scattering components using the exact single scattering solutions R_s, of which formula is known analytically as,

$$R_t = R_s + R_m + R_g,$$

(9)

$$R_s = \frac{\pi\omega P}{\tau} \frac{1 - \exp\{-\tau(1/\mu + 1/\mu_0)\}}{1/\mu + 1/\mu_0},$$
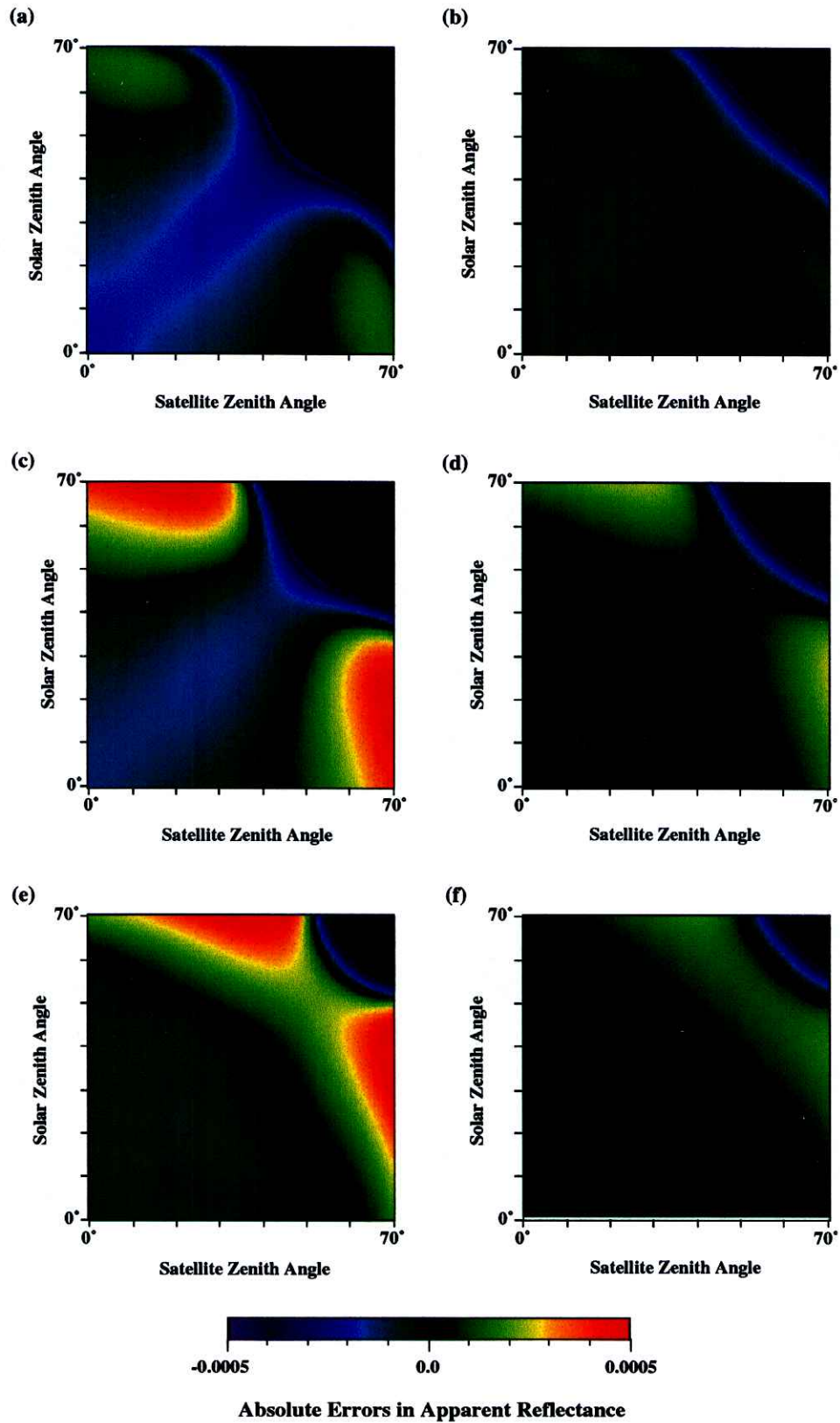
(10)

Fig. 2   Same as in Fig. 1(a), but for syntheses by Eq. (6) with $N = 4$ (a) and 5 (b);
Eq. (12) with $N = 4$ (c) and 5 (d); Eq. (13) with $N = 4$ (e) and 5 (f).

25

where ω, τ, and P are the single scattering albedo, optical thickness and scattering phase function of the atmospheric layer, respectively. As compared with Eq. (6), the decomposition by Eq. (9) is further efficient for making a look-up table of radiances, since the multiple scattering component R_m, is a weak function of angular parameters for large zenith angle.

We further divide R_m into the multiple scattering components by Rayleigh scattering $R_{r,m}$ and by aerosols $R_{a,m}$, because the polarization effect is mostly caused by the Rayleigh multiple scattering as described later. $R_{r,m}$ is expressed by a three term Fourier expansion similar to Eq. (3),

$$R_{r,m} = \sum_{m=0}^{2} R_{r,m}^{(m)} \cos m\phi. \tag{11}$$

Formulating $R_{a,m}$ by a polynomial function of τ_a as follows,

$$R_{a,m} = R_t - R_s - R_{r,m} - R_g = \sum_{n=1}^{N} c_n \tau_a^n, \tag{12}$$

absolute error distributions in $R_{a,m}$ by the approximation Eq. (12) with $N = 4$ and 5 are shown in Fig. 2(c) and (d), respectively, as same as in Fig. 1(a). For comparison, results with the approximation Eq. (6) with $N = 4$ and 5 are shown in Fig. 2(a) and (b). The approximation Eq. (12) increases the accuracy in the whole angular region with decreased area of the absolute error larger than 0.005 in magnitude, although large errors start appearing in the region of θ_0 (θ) > 60° and θ (θ_0) < 40°. These experiments suggest that the behaviour of the optical thickness dependence of the aerosol multiple scattering is close either to Eq. (5) or to Eq. (6) depending on the angular geometries. Therefore we try the following formula by adding a small correction term with the same exponential dependence as the exact single scattering,

$$R_{a,m} = R_t - R_s - R_{r,m} - R_g = \frac{1}{\mu\mu_0}\left\{\sum_{n=1}^{N-1} c_n \tau_a^n + c_N\left[1 - \exp\{-\tau_a(1/\mu + 1/\mu_0)\}\right]\right\}. \tag{13}$$

Note that the order for the polynomial function is N-1 instead of N as compared with Eqs. (6) and (12). Results for $R_{a,m}$ with the approximation Eq. (13) with $N = 4$ and 5 are shown in Figs.

26

2(e) and (f). The introduction of the exponential correction term improves the accuracy as compared with Fig. 2(c) or 2(d) even with the $(N-1)th$ order polynomial function. Figure 2(f) shows that Eq. (13) with $N = 5$, absolute errors are reduced significantly to values less than ±0.0001 in the following angular region,

$$\theta + \theta_0 \leq 125°, \tag{14}$$

especially at the large solar and satellite zenith angles. It is very interesting to observe that the last exponential term is needed to improve the approximation significantly.

Due to the assumption of a rough ocean surface as a boundary condition, components in Eq. (9) depend on u_{10}. By analogy of that the strong angular dependence of R_t is caused mostly by the single scattering component, the dependence of R_t on u_{10} can be decomposed into a main contribution from R_g and small corrections in other terms. Figure 3 shows absolute errors in R_t for various wind conditions ($u_{10} = 1, 2, 7, 10, 15$ m/s), when the radiance is calculated by Eq. (9) with a fixed wind velocity $u_{10} = 7$ m/s ignoring the dependence on u_{10} except for the term R_g. Wind velocity dependence of R_g is given by an analytical formula as in Nakajima and Tanaka (1983). Errors caused by this approximation are almost less than
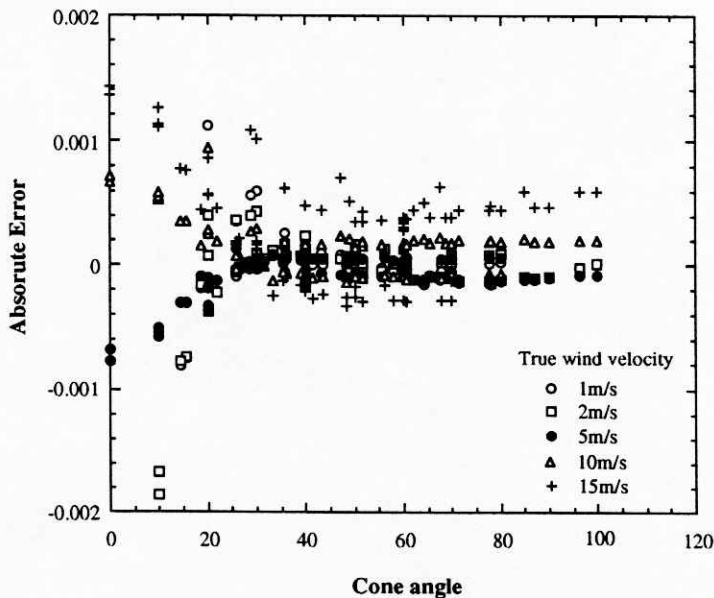
Fig. 3   Absolute errors in R_t synthesized with the multiple scattering components calculated with $u_{10} = 7$ m/s ignoring the wind velocity dependence. Wind velocities for exact calculation are for $u_{10} = 1(\bigcirc)$, $2(\square)$, $5(\bullet)$, $10(\triangle)$, and 15 m/s(+).

±0.0002 when $u_{10} \leq 10$ m/s, except for the sun-glitter region with the half cone angle $\Psi < 30°$ around the specular reflectance angle. Errors exceed ±0.0002 for most of the angular region when $u_{10} \geq 15$ m/s, so that such data are avoided in the aerosol retrieval algorithm (Higurashi and Nakajima, 1997). According to Fig. 3, it is found that the dependence of R_t on u_{10} is mainly caused by R_g. By the decomposition as in Eq. (13), therefore, it makes possible to reduce the number of parameters, on which each term in Eq. (13) depends.

3. 2. 2 Influence of polarization

The polarization effect in the satellite-received total radiance is as small as less than 5%, and is ignored in the most applications of satellite remote sensing. However, this effect cannot be ignored when a small difference of radiances or a color ratio of two channel radiances becomes an important issue in the application, such as ocean color remote sensing and the Ångström exponent retrieval in aerosol remote sensing. Since the polarization effect has been studied extensively in the past studies (Gordon and Wang, 1992; Ogawa et al., 1989), we want to study briefly in this subsection the accuracy of Eqs. (9)-(11) for simulating the polarization effect. The difference in R_t between with and without polarization effect is shown
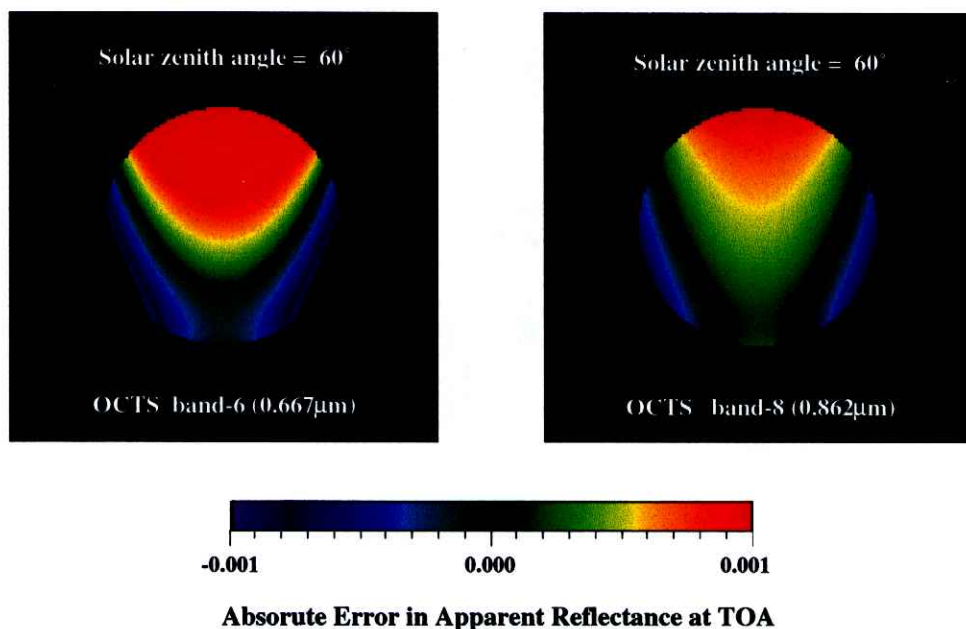
Fig. 4   Absolute errors in R_t when the polarization effect is ignored at 0.667 and 0.862 μm for $\theta_0 = 60°$.

28
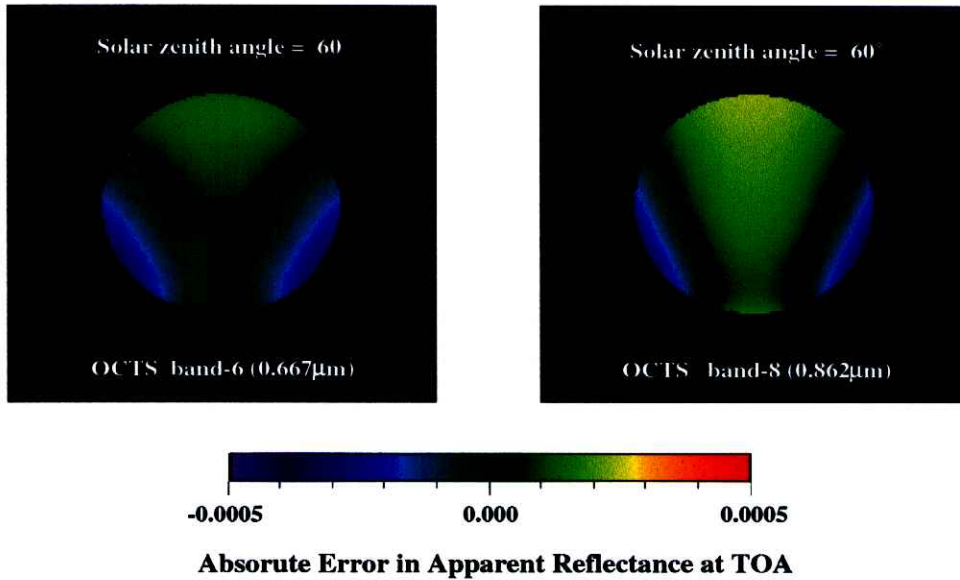
Fig. 5 Same as in Fig. 4, but when the polarization effect is ignored only in the aerosol
   scattering component.

in Fig. 4, $\theta_0 = 60°$ at $\lambda = 0.667$ and 0.862μm, which correspond to band-6 and -8 of ADEOS / OCTS, respectively. True radiance values with polarization effect have been calculated made by *PSTAR-1b*, which is the vector version of *RSTAR-5b*. The condition for the simulation is as same as in section 3.2.1. The polarization effect causes a positive difference around the solar point and a negative difference around $\phi = 90°$ and the magnitude of differences depends on wavelength, that is, ranges from -0.0015 to +0.0026 at 0.667μm and from -0.0008 to +0.0011 at 0.862μm. Since the polarization effect is mainly caused by Rayleigh scattering, the synthesized radiance by Eq. (9) will be improved efficiently by taking into account the polarization for only the contribution of Rayleigh scattering as shown in Fig. 5. By this approximation, errors reduce to ±0.0002 in most regions.

3. 2. 3 Effects of gaseous absorption

It is necessary to take into account the gaseous absorption, if some absorption bands are included in the spectral range of a channel under study. Visible and near infrared channels used for aerosol remote sensing, such as channel-1 (0.63μm) and -2 (0.84μm) of NOAA / AVHRR, band-6 (0.670μm) and -8 (0.865μm) of ADEOS / OCTS, are affected by the gaseous absorption of ozone, water vapor, and oxygen. Especially, the channel-2 of AVHRR is strongly

influenced by water vapor absorption, because it has a very broad band width including strong water vapor absorption bands. Since the spatial and temporal variation of water vapor and ozone amounts are large, it is desirable to separate these effects in the following formula,

$$R_t = T_{o_3} T_{H_2O} R_t^*, \tag{15}$$

where T_{O_3} and T_{H_2O} describe the correction factors for the ozone and water vapor absorption, respectively, and R_t^* is the apparent reflectance at TOA without ozone and water vapor absorption.

According to numerical simulations, T_{O_3} is approximated by

$$T_{o_3} = exp\left[-\tau_{o_3}(1/\mu + 1/\mu_0)\right], \tag{16}$$

where τ_{o3} is the ozone optical thickness, as shown in Fig. 6, provided T_{H_2O} is ignored. This means that a simple two way transmittance is enough to correct the ozone absorption because ozone exists in the upper atmosphere. On the other hand, the influence of water vapor absorption is more complicated and difficult to formulate. We have tabulated the ratio of the apparent reflectance with and without water vapor absorption, as a correction factor for water
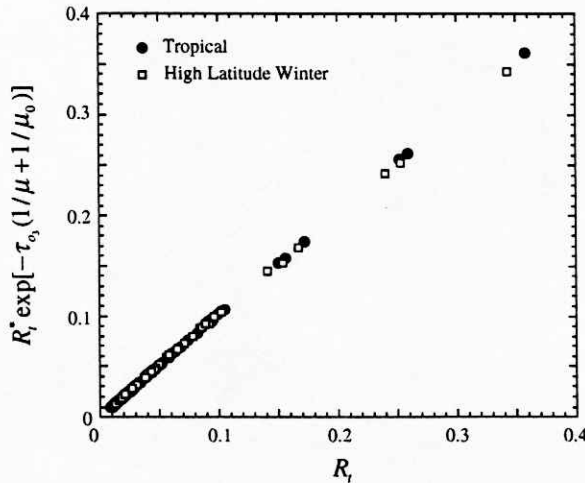

Fig. 6   The correlation between R_t and approximated values with the ozone absorption correction by Eq. (16) in channle-2 of NOAA / AVHRR for atmospheric model of tropical(●) and high latitude winter(□) in LOWTRAN-7. Note the ozone amount is smallest in tropical atmosphere and largest in high latitude winter.
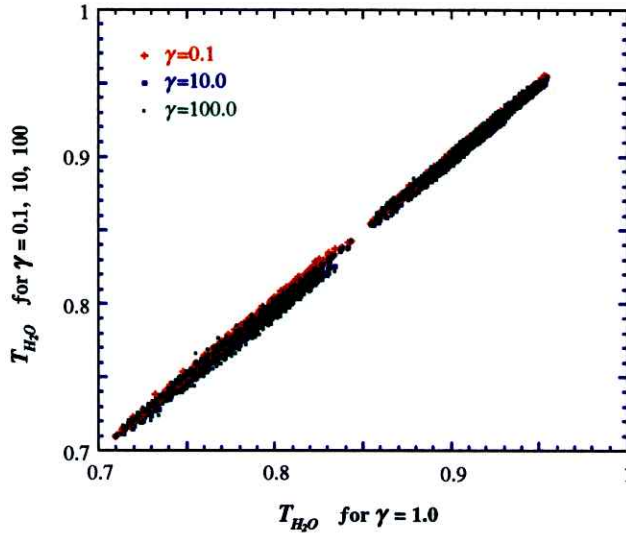
Fig. 7 The correlation between the correction factor for channel-2 of AVHRR with $\gamma = 1$ and those with $\gamma = 0.1(+)$, $10(\times)$, and $100(\blacksquare)$, for various conditions, i.e., $\theta_0 = 0°$ (10°) 70°, $\theta = 0°$ (10°) 50°, $\phi = 0°$ (30°) 180°, $\tau_a = 1.0E{-}10$, 0.001, 0.01, 0.02, 0.1, 0.4, 1, 2, and $w = 0$, 0.04, 0.1, 0.2, 0.4, 1, 2, 4, 6, 10 g/m².

vapor absorption, for eight solar zenith angles ($\theta_0 = 0°$ (10°) 70°), six satellite zenith angles ($\theta = 0°$ (10°) 50°), seven azimuth angles ($\phi = 0°$ (30°) 180°), eight cases for τ_a (1.0E-10, 0.001, 0.01, 0.02, 0.1, 0.4, 1, 2), and ten cases for water vapor amount ($w = 0$, 0.04, 0.1, 0.2, 0.4, 1, 2, 4, 6, 10 g/m²). Although the correction factor also depends on γ its effects are not significant as found in Fig. 7, which shows the correlation between the correction factor for channel-2 of NOAA / AVHRR with $\gamma = 1$ and those with 0.1, 10., and 100. Therefore, γ is fixed as 1.0 for the correction factor of water vapor absorption adopted in the operational version of the present algorithm.

In the above mentioned numerical simulations, the method for wavelength integration of spectral radiances with the response function of the satellite-borne radiometer as a quadrature weight is significant for accurate calculation of the apparent reflectance in each channel, especially which includes gaseous absorption bands. We adopt theoretical satellite-received radiances spectrally integrated with 105 and 233 wavelength grids and with 2.5 nm intervals in channel-1 and -2 of NOAA / AVHRR, as reference values for comparison of various wavelength integrations. Performing such numerical simulations, we have adopted 15 and 33 wavelength grids for channel-1 and -2, respectively, to calculate the correction factor of water vapor absorption, and 11 and 20 grids to calculate the multiple scattering component to keep the accuracy less than 0.1%.

31

3. 3 Reconstruction of the radiance field

In the preceding sections, we have discussed the structure of the radiance field in the atmosphere-ocean system and obtained efficient formulae to synthesize the TOA radiance as proposed by Eqs. (9), (10), (11), and (13). In this section, we discuss the angular interpolation of the coefficients appeared in those formulae for tabulation, which is needed for operational application to large volume data analyses. For tabulation of the coefficients, we should select angular grid points as less as possible, but keeping accuracy. In order to select a proper system of angular grid points, we examine the accuracy of the synthesized R_m with an interpolation of various grid points. Concerning the azimuth angle, we investigate, cases with changing angular step for interpolation by three order Lagrange's formula, i.e., $\Delta\phi =$ 2.5°, 5°, 10°, 15°, and 20° in the range from 0° to 180°, for $\theta_0 = 60°$, $\tau_a = 0.1$, and $u_{10} = 0.1$ as shown in Fig. 8(a) to (e). Although $\Delta\phi = 10°$ is accurate enough for interpolation in the region of $\phi > 40°$, a narrower interval, 5° or 2.5°, is needed in the forward scattering region ($\phi < 40°$). We, therefore, adopt an angular gridding with variable intervals, i.e., 23 azimuth angles as ϕ = 0° (5°) 40°; 40° (10°) 180°. As shown in Fig. 8(f), absolute errors in the interpolated field with this gridding are less than 1.0E-4 except around sun glint. This azimuthal angle gridding will be enough accurate, since data within 30° half cone angle around the specular reflectance angle are avoided from analyses.

To decide griddings of satellite and solar zenith angles, we examine in Fig. 8(g) and (h) the accuracy of interpolation with intervals $\Delta\theta$, $\Delta\theta_0 = 2.5°$ and 3.5°, fixing 25 azimuth angles $\phi = 0°$ (2.5°) 10°; 10° (5°) 40°; 40° (10°) 180°, which are slightly finer azimuthal angle grids slightly finer than those of the operational algorithm determined in the preceding paragraph to secure the accuracy for interpolation regarding azimuth angles. A three term Lagrange's interpolation formula is also used in these examinations. Figure 8(h) shows that the accuracy is not good at high zenith angles and in forward direction, associated with an oscillation in the reconstructed field due to the interpolation.

As a result of the above discussion, we make tables of coefficients, c_n, in Eq. (13) for the present algorithm, at 29 solar zenith angles ($\theta_0 = 0°$ (2.5°) 70°), 21 satellite zenith angles ($\theta =$ 0° (2.5°) 50°), and 23 relative azimuthal angles ($\phi = 0°$ (5°) 40°; 40° (10°) 180°), and 11 cases of the peak ratio ($\gamma = 0.1, 0.2, 0.5, 1, 2, 3, 5, 10, 20, 50, 100$), assuming $u_{10} = 7$ m/s. Figure 9 shows absolute errors in R_t by the approximation of Eq. (13) and interpolation for all possible
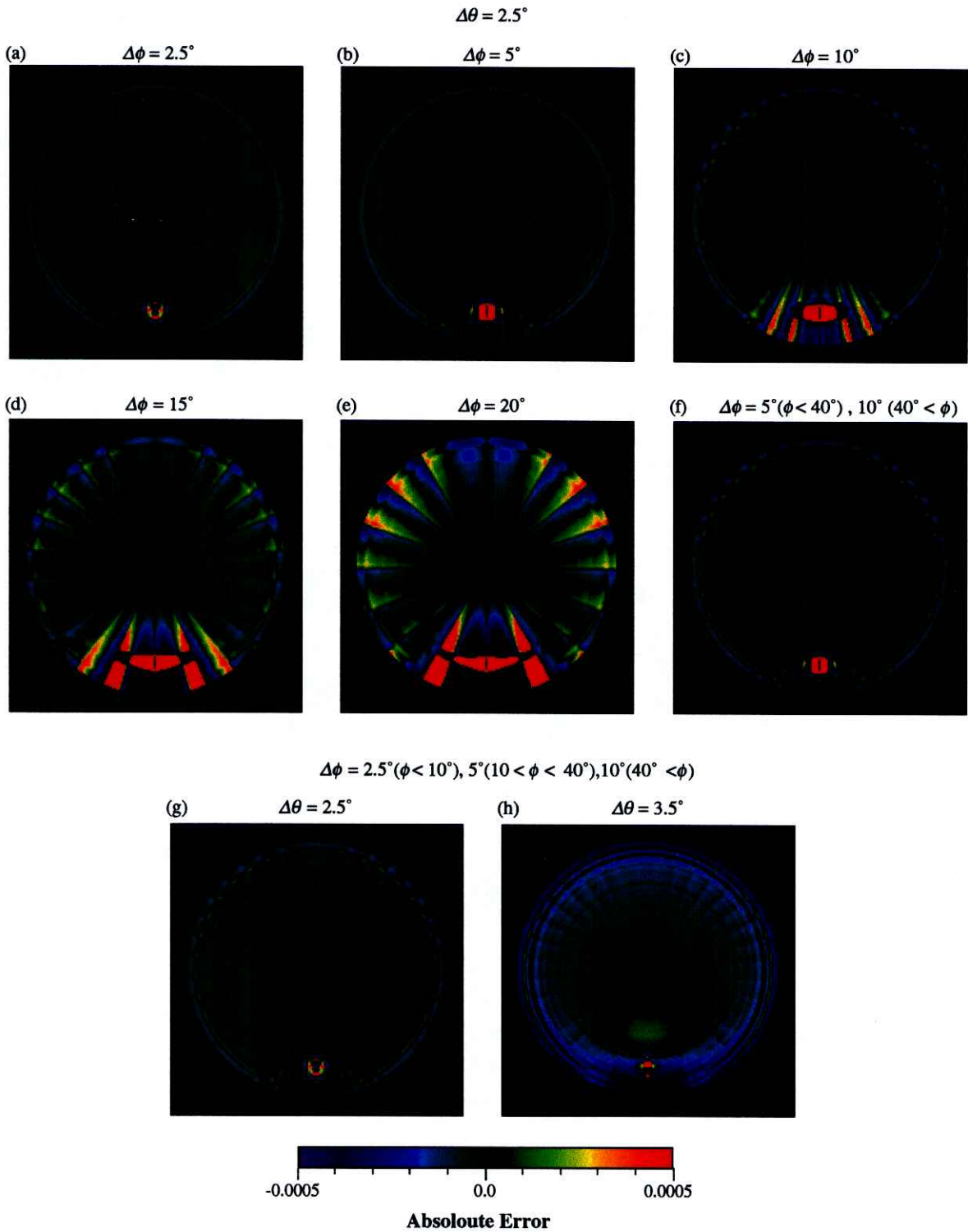
Fig. 8 Absolute errors in R_t caused by angular interpolation regarding ϕ with $\Delta\phi$= 2.5°, 5°, 10°, 15°, and 20° (a-f); interpolation regarding θ with $\Delta\theta$= 2.5° and 3.5° (g-f), for θ_0= 60°, τ_a= 0.1, and u_{10}= 0.1.
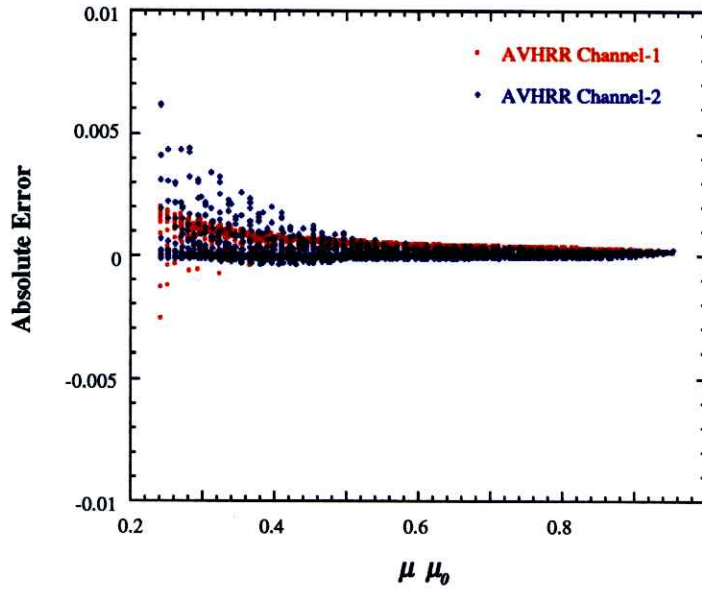
Fig. 9 Total absolute errors in R_t synthesized by Eq. (13) with $N = 5$ and angular interpolation for angular geometries in the whole sky except for $\Psi < 30°$ for channel-1(red dots) and -2(blue dots) of NOAA / AVHRR.

angular geometries except for the region $\Psi < 30°$ for channel-1 and 2 of NOAA / AVHRR. Although almost all errors are less than 0.0005, they are increasing with decreasing $\mu\mu_0$, i.e., with increasing atmospheric path length. This reason may be that the optical thickness used in the calculation of exact single scattering by Eq. (10) is incorrect. τ in Eq. (10) consists of the optical thickness of aerosols, molecular, ozone, water vapor, and oxygen integrated in each channel with a weight of the response function. This spectrally averaaged optical thickness is not necessarily the most suitable equivalent optical thickness which produces spectrally integrated reflectances with Eq. (10). We do not perform, however, further tuning of the spectrally averaged optical thickness in Eq. (10), since generated errors are not significant for the retrieval.

3. 4 Conclusions

In this paper we have discussed the structure of the TOA radiance field in the atmosphere-ocean system in order to obtain a formulation for effective syntheses of satellite-received radiances.

We decompose R_t into the exact single and multiple scattering components, taking into

34

account that strong angular dependence of R_t is caused by single scattering and of which analytic formula is known. An introduction of the exact single scattering solution instead of linearized single scattering approximation improves significantly the accuracy of synthesized apparent reflectance, only when an exponential term is added to the polynomial function of τ_a as shown in Eq. (13). This exponential term is introduced to cancel the exponential dependence in the exact single scattering component which is not suitable in the angular region of $\theta_0 (\theta)$ > 60° and $\theta (\theta_0) < 40°$. If we adopt Eq. (6), higher order coefficients are needed to keep the accuracy of synthesized radiances synthesized by Eq. (13), especially for large zenith angles. It is interesting to observe in Fig. 2 that the optical thickness dependence of the aerosol multiple scattering becomes a linear type or an exponential type depending on the angular geometries. Note that the size of the two channel look-up table for the aerosol multiple scattering formula by Eq. (13) with $N = 5$ is 6.2 M bytes, with 21 θ_0 s, 29 θs, 23 ϕs, 11 γs. The table size will increase by 1.2 M bytes as the order N increases to $N+1$.

Since the polarization effect and the dependence of u_{10} on R_t are mainly caused by $R_{r.m}$ and R_g in Eq. (13), respectively, a separation of these components from R_t, reduces significantly the dependence of coefficients on geophysical and angular parameters. The total accuracy of the synthesized R_t by the proposed formula Eq. (13) and angular interpolation is almost less than 0.0005 in absolute error. This is accurate enough for synthesizing AVHRR channel-1 and 2 radiances, because quantization errors with the A/D coverter of AVHRR is $\Delta\rho_t \approx 0.001$. This is also accurate enough for ocean color remote sensing, since, for example, the required accuracy for SeaWiFS is $\Delta\rho_w \approx 0.001$ (Gordon and Wang, 1994).

References

Chandrasekhar, S., 1949: Radiative transfer. 393pp., Dover, New York.

Durkee, P. A., F. Pfeil, E. Frost, and R. Shema, 1991: Global analysis of aerosol particle characteristics. *Atmos. Environ*, **25A**, 2457-2471.

Gordon, H. R., and M. Wang, 1992: Surface - roughness considerations for atmospheric correction of ocean color sensors. I: The Rayligh - scattering component. *Appl. Opt.*, **31**, 4247-4260.

Gordon, H. R., and M. Wang, 1994: Retrieval of water-leaving radiance and aerosol optical thickenss over the ocean s with SwaWiFS: a preliminary algorithm. *Appl. Opt.*, **33**, 443-452.

Gordon, H. R., D. K. Clark, J. W. Brown, O. B. Brown, R. H. Evans, and W. W. Broenkow, 1983: Phytoplankton pigment concentrations in the Middle Atlantic Bight: comparison of ship determinations and CZCS estimates. *Appl. Opt.* **22**, 20-36.

Herman, J. R., P. K. Bharita, O. Torres, C. Hsu, C. Seftor, and E. Celarier, 1997: Global distribution of UV-absorbing aerosols from Nimbus 7 / TOMS data. *J. Geophys. Res.* **102**, 16911-16922.

Higurashi, A., and T. Nakajima, 1997: Development of a two chaneel aerosol retrieval algorithm on global scale using NOAA / AVHRR. *J. Atmos. Sci.* accepted.

Huser, R. B., J. M. Prospero, and L. L. Stowe, 1997: Characterization of tropospheric aerosols over the oceans with the NOAA advanced very high resolution radiometer optical thickness operational product. *J. Geophys. Res.* **102**, 16889-16909.

Kneizys, F. X., E. P. Shettle, L. W. Abreu, J. H. Chetwynd, G. P. Anderson, W. O. Gallery, J. E. A. Selby, and S. A. Clough, 1988: Users Guide to LOWTRAN 7. AFGL-TR-88-0177.

Mitchell, J. F. B., T. C. Johns, J. M. Gregory, and S. F. B. Tett, 1995: Climate response to increasing levels of greenhouse gases and sulphate aerosols. *Nature*, **376**, 501-504.

Moulin, C., F. Dulac, C. E. Lambert, P. Chazette, I. Jankowiak, B. Chatenet, and F. Lavenu, 1997: Long-term daily monitoring of Saharan dust load over ocean using Meteosat ISCCP-B2 data 2. Accuracy of the method and validation using sun photometer measurements. *J. Geophys. Res.*, **102**, 16959-16969.

Nakajima, T., and M. Tanaka, 1983: Effect of wind-generated waves on the transfer of solar radiation in the atmosphere-ocean system. *J. Quant . Spectrosc. Radiat. Transfer* **29**, 521-537.

Nakajima, T., and M. Tanaka, 1986: Matrix formulations for the transfer of solar radiation in a plane-parallel scattering atmosphere. *J. Quant, Spectrosc. Radiat. Transfer* **35**, 13-21.

Nakajima, T., and M. Tanaka, 1988: Algorithms for radiative for intensity calculations in moderately thick atmospheres using a truncation approximation. *J. Quant . Spectrosc. Radiat. Transfer* **40**, 51-69.

Ogawa, H., M. Tanaka, and T. Nakajima, 1989: A simple expression for the additional sky radiance produced by polarization effects. *J. Meteor. Soc. Japan*, **67**, 877-888.

Stowe, L. L., R. M. Carey, and P. P. Pellegrino, 1992: Monitoring the Mt. Pinatubo Aerosol Layer With NOAA / 11 AVHRR Data. *Geophys. Res. Lett.* **19**, 159-162.

Wang, M., and H. R. Gordon, 1993: Retrieval of the columnar aerosol phase function and single-scattering albedo from sky radiance over the ocean: simulations. *Appl. Opt.* **32**, 4598-4609.

Chapter 4

Development of a Two Channel Aerosol Retrieval Algorithm on Global Scale Using NOAA / AVHRR

4 Development of a Two Channel Aerosol Retrieval Algorithm on Global Scale Using NOAA / AVHRR

ABSTRACT

This study proposes a two channel satellite remote sensing algorithm for retrieving the aerosol optical thickness and Ångströme exponent which is an index for the aerosol size distribution. An efficient look-up table method is adopted in this algorithm to generate spectral radiances in channel-1 and -2 of NOAA / AVHRR over ocean areas. Ten day composite maps of the aerosol optical thickness and Ångström exponent have been obtained from AVHRR GAC data in January and July of 1988. Aerosol optical thickness maps show that the major aerosol sources are located off the west coast of north and south Africa, and Arabian Peninsula. The most important contributor is soil-derived particles from Saharan desert which cross the Atlantic Ocean. Our optical thickness values tend to be larger than values given by the NOAA operational algorithm. A ten day composite maps of Ångström exponent show man-made air polluted regions, such as the Mediterranean Sea, the Black Sea, and east coasts of north America and China, have large values suggesting small particles are dominant in these regions.

4. 1 Introduction

The impact of atmospheric aerosols on the earth's climate has been recognized as an important problem for understanding the climate formation, especially after several studies pointing out that aerosols are the source of greatest uncertainties in evaluating climate forcing (Hansen and Lacis, 1990; Shi et. al., 1994). Aerosols directly influence the climate through perturbation of the radiation budget by scattering solar radiations back to space (leading to negative radiative forcing) and by absorbing solar and thermal radiations (leading to positive forcing). Acting as CCN (Cloud Condensation Nuclei) or IC (Ice Nuclei), aerosol particles modify the cloud microphysics (Twomy, 1977; Kaufman and Nakajima, 1993), and hence, aerosol particles also indirectly have an effect on climate. In contrast to the greenhouse gases, which act only on the longwave radiation process, aerosol particles can influence both

38

shortwave and longwave radiation. The magnitude of the effects also depends on their composition and size.

Radiative forcing of sulfate aerosols has been studied extensively by many investigators with a recognition that they are climatologically most important for evaluating the anthropogenic global warming trend. Their globally averaged direct effect is estimated as -0.3 to -0.9 Wm^{-2} (Charlson et al, 1992; Kiehl and Briegleb, 1993; Taylor and Penner, 1994), and the indirect one as about -1.3 Wm^{-2} (Jones et al., 1994). These studies suggest, therefore, the total sulfate aerosol forcing is comparable in magnitude to the current anthropogenic greenhouse gas forcing, but in opposite sign. There is, however, a large uncertainty in the evaluation of both direct and indirect effects of the sulfate aerosols. The forcing mechanism with aerosols is highly complex and needs more studies before leading a clear conclusion. For example, aerosols originated from dimethyl sulfate may change cloud microphysics significantly. Such indirect effect will be temperature dependent, and hence, may make a feedback loop with the global warming process. Some studies have suggested recently that mineral dust aerosols generated from disturbed soil are importance as a climate forcing agent that need to be included among the climate forcing factors influenced by human activities (Li et al., 1996; Tegen et al., 1996).

In order to reduce the above mentioned large uncertainties in evaluation of the aerosol forcing, it is necessary to improve our knowledge of aerosol characteristics, such as the total content, composition and so on, on global scale. A use of satellites is very effective to study aerosol optical properties on large scale. Most of aerosol remote sensing studies have been made using NOAA (National Oceanic and Atmospheric Administration) / AVHRR (Advanced Very High Resolution Radiometer) channel-1 and/or -2. Stowe et al. (1992) produced global maps of the aerosol optical thickness at wavelength of 0.5 μm over ocean area using channel-1 radiances of AVHRR. Although the one channel algorithm is appreciated as for showing the global distribution of the aerosol optical thickness, there is some tendency toward underestimation of the optical thickness by due to fixed aerosol particle size distribution and refractive index as shown by Ignatov et al. (1995a, 1995b). Durkee et al. (1992) pointed out importance of the impact of the phase function assumed in the one channel algorithm, and introduced a two term Henyey-Greenstein phase function to solve this problem. They obtained a global map of an index of size distribution, which is the ratio of channel-1 and -2 radiances

of AVHRR, in addition to the optical thickness obtained from channel-1 radiance. To simplify the problem, they adopted the single scattering approximation in the transfer calculation of their algorithm. Such an approximation is, however, questionable for thick absorbing aerosol cases such as Saharan desert aerosols. Moreover, they did not report how to treat water vapor absorption in channel-2 of AVHRR, which significantly affect the channel-2 radiance (Stowe et al., 1997). Kaufman et al. (1990) proposed an algorithm to estimate the aerosol optical thickness, the particle geometrical mean mass radius, and single scattering albedo from channel-1 and -2 of AVHRR. Nakajima and Higurashi (1996) retrieved aerosol optical thickness, Ångströme exponent, and single scattering albedo of aerosols for the Persian Gulf oil fire event in 1991 by a method similar to Kaufman et al. (1990). Those two algorithms are significant for the aerosol remote sensing, because it is possible to retrieve almost all important parameters to describe the aerosol optical properties over land and ocean. Their applications are limited to local area data so far, and extension to global analysis algorithms is not so trivial. The algorithm using a reflectance contrast of images between clear and hazy day has to find an automatic detection algorithm for the contrast, and the local has to find look-up table models of radiances have to be studied in order to find an efficient synthetic method of radiances.

We will reinvestigate in this paper the structure of the radiance field in aerosol-loaded atmosphere-ocean systems in Section 2. With these analyses, we will propose an efficient look-up table method to synthesize satellite-received radiances accurately and efficiently with careful correction of multiple scattering and gaseous absorption in channel-1 and -2 radiances. The proposed algorithm will be tested by extensive numerical simulations as shown in Section 3. Finally it will be applied to real AVHRR GAC data in January and August of 1988 for generating global aerosol maps.

4. 2 Radiance fields in aerosol-loaded atmosphere-ocean systems

The satellite-received shortwave radiance emerges from an atmosphere-ocean system as a result of interaction with atmosphere, ocean surface, and ocean body. It is important to study the dependence of the radiance on inherent parameters describing the optical properties of the atmosphere-ocean system in order to develop a look-up tables (LUT) approach, which is efficient for global remote sensing analyses.

40

4. 2. 1 The structure of radiance fields

The satellite signal over ocean area is composed of contributions from atmospheric path radiance and water leaving radiance. The water leaving radiance is further composed of reflection by the ocean surface, scattering by foams, and upwelling radiance from the ocean body. The latter two components can be ignored for most applications at wavelengths of AVHRR channel-1 and -2 ($\lambda = 0.64$ and 0.83 μm) due to large water absorption.

The traditional method of the atmospheric correction (Gordon and Wang, 1992) introduces a linearized single scattering approximation R_{as}, to synthesize the apparent reflectance R detected by a satellite radiometer as,

$$R \approx R_{as} + R_{mol} + R_g, \tag{1}$$

where R_{mol} and R_g are apparent reflectances for the molecular atmosphere without aerosol loading and for sun-glint component, respectively. We define the apparent reflectance as,

$$R = \frac{\pi L}{\mu_0 F_0}, \tag{2}$$

with the satellite-received radiance L, the extraterrestrial solar incident flux F_0 and the cosine of solar zenith angles, $\mu_0 = \cos \theta_0$. The linearized aerosol single scattering component is expressed as,

$$R_{as} = \frac{\pi \omega_a P_a(\Theta)}{\mu \mu_0} \tau_a, \tag{3}$$

where ω_a, τ_a and $P_a(\Theta)$ are the aerosol single scattering albedo, optical thickness and phase function, respectively, and μ is the cosine of zenith angle of the emergent radiation θ. Equation (1) with Eq. (3) has a large error in the synthesized reflectance for large optical thickness and/ or absorbing aerosol cases.

Trying to improve the approximation, Wang and Gordon (1993) have found that the multiple aerosol-molecular scattering component is almost proportional to the linearized aerosol single scattering reflectance as follows,

$$R - R_{mol} - R_g = \sum_{n=0}^{2} c_n R_{as}^{\ n} . \tag{4}$$

They successfully reduced the error involved in synthesized radiances with Eq. (4). Introducing Eq. (3) into Eq. (4) we lead the following expression for the multiple aerosol-molecular scattering component,

$$R - R_{mol} - R_{as} - R_g = \frac{1}{\mu\mu_0} \sum_{n=0}^{2} c_n \tau_a^n . \tag{5}$$

This formula is in some sense convenient for retrieving the aerosol optical thickness τ_a, since Eq. (5) is in a form of series expansion of τ_a. Also it should be noted that it is not suitable to expand the multiple scattering component, which is a weak function of angular variables, by the linearized single scattering component R_{as}, which is a strong function of angular variables with the aerosol phase function $P(\Theta)$. On the other hand, this part is suitably separated in Eq. (5) by R_{as} in the left hand of equation. The ADEOS OCTS (Ocean Color and Temperature Scanner) operational algorithm has adopted this formulas (Nakajima et al., 1996).
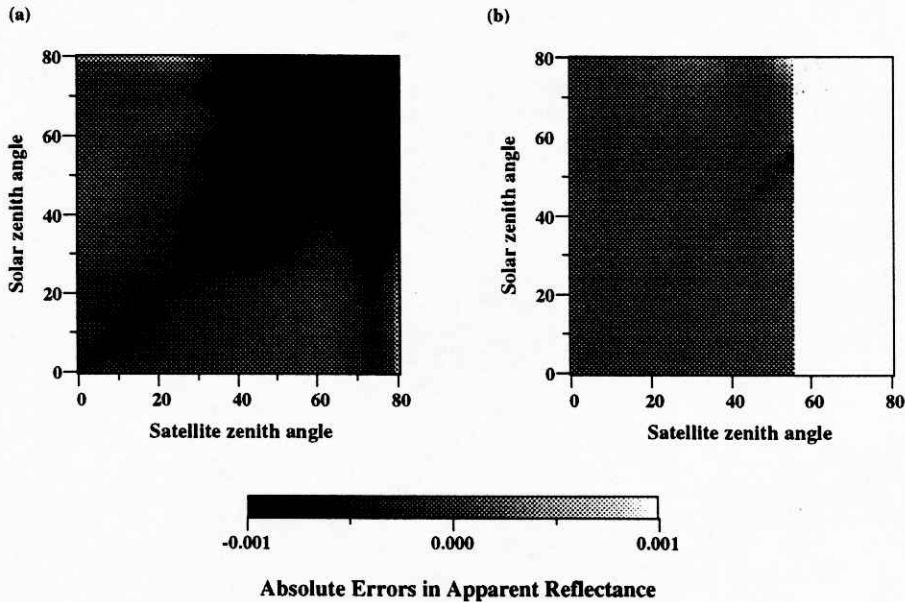

Fig. 1 (a) Absolute errors in the apparent reflectance at the top of the atmosphere (TOA) synthesized by Eq. (5) for various solar and satellite zenith angles. $\tau_a = 0.1$. (b) Same as in Fig. 1, but synthesized by Eq. (9).

Although the approximations Eqs. (4) and (5) will be accurate enough for most applications, one can find large errors exceeding 0.1% at large zenith angles as well as at sun-glint angles as shown in Fig. 1(a), which indicates absolute errors in apparent refletctances for various solar and satellite zenith angles at the azimuth angle of 0° and at the aerosol optical thickness of 0.1. In the figure the exact values have been calculated by a general radiative transfer code for atmosphere-ocean system, *Rstar*-5b, which is developed by Center for Climate System research (CCSR), Univ. of Tokyo. This code acounts for multiple scattering in the atmosphere by molecules and aerosol particles, and bidirectional surface reflection (Nakajima and Tanaka, 1986, 1988). The ocean surface reflection is calculated using a rough ocean model (Nakajima and Tanaka, 1983). The gaseous absorption is taken into account with Lowtran-7 absorption model (Kneizys et al., 1988). In this experiment, we assumed the US-standard atmosphere and the log-normal volume spectrum for aerosol size distribution as,

$$\frac{dV}{d\ln r} = C\exp\left[-\frac{1}{2}\left(\frac{\ln r - \ln r_m}{\ln s}\right)^2\right],$$ (6)

where V is the aerosol volume density, r_m is the mode radius in μm, and $\ln(s)$ is the standard deviation of $\ln(r)$. r_m and s are set to 0.2 and 1.5, respectively. As shown by Fig. 1(a), large errors appear at large angles as well as in sun-glint region. Numerical simulations have shown that these large errors are caused by the linearized single scattering approximation Eq. (3) adopted in Eq. (5), which is not suitable at such large zenith angles.

The above observation in Fig. 1(a) makes us think about an exact solution for single scattering (Chandrasekhar, 1960) for synthesizing the satellite-received reflectance,

$$R_s = \frac{\pi\omega P(\Theta)}{\mu\mu_0 F}\frac{1 - \exp\{-\tau(1/\mu + 1/\mu_0)\}}{1/\mu + 1/\mu_0}.$$ (7)

where ω, τ and $P(\Theta)$ is the single scattering albedo, optical thickness and phase function of the atmospheric layer, respectively. In the actual coding we have taken into account the inhomogenity of the atmosphere by setting multi layers (Nakajima and Tanaka, 1988). With the definition of Eq. (7), we have the following expression for the apparent reflectance at the top of the atmosphere (TOA) into single and multiple scattering contributions as,
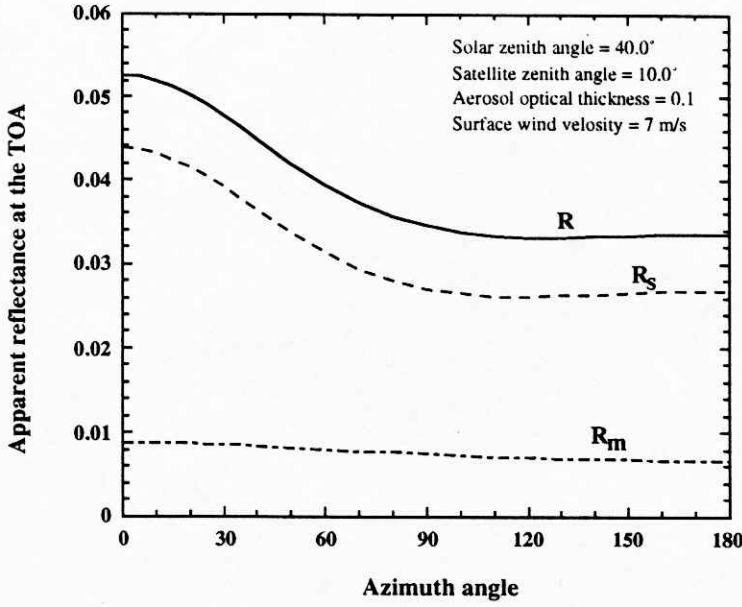
Fig. 2 The angular dependence of the apparent reflectance at TOA for single scattering
component R_s, multiple scattering components R_m, and total value R.

$$R = R_s + R_m.$$ (8)

Figure 2 show each component in Eq. (8) as a function of azimuth angles. It is found from
Fig. 2 that the large angle dependence in the reflectance is caused by the single scattering
component, and hence it is effective to tabulate the multiple scattering component for making
the LUT. Some further consideration and numerical tests have suggested that tabulation of
the coefficients in the following expansion is effective more than using Eq. (5),

$$R - R_s - R_g = \frac{1}{\mu\mu_0}\left[\sum_{n=0}^{3}c_n\tau_a^n + c_4\exp\{-\tau_a(1/\mu+1/\mu_0)\}\right].$$ (9)

The exponent term in the right hand side of Eq. (9) is introduced to take into account the fact
suggested by Gordon and Wang (1993), i. e., the multiple scattering component has a similar
optical thickness dependence to the linearized single scattering approximation Eq. (3) even
though the exact single scattering Eq. (7) has an exponential function dependence. The cubic
polynomial expansion is also introduced to improve the approximation for large optical

44

thickness cases. Figure 1(b) shows that the approximation with Eq. (9) is much better than with Eq. (5) shown in Fig. 1(a), especially for larger zenith angle cases. Detailed investigation (Higurashi et al., 1997) has found that the exponential term in both sides of Eq. (9) is needed to improved the approximation.

4. 2. 2 Optical models of aerosols

A suitable assumption of the aerosol optical model is another important point for realizing a good aerosol retrieval algorithm, since the inversion is not unique for retrieving the parameters to model the aerosol optical properties. With two wavelengths in our situation, a reasonable strategy will be to assume a suitable size distribution which is enough applicable for various conditions and simple enough to have a small number of parameters to model the aerosol size distribution.

Aerosol size distributions have been measured under various conditions since early seventies. Junge (1969) and Toon and Pollack (1976) proposed a power law size distribution is representative for stratospheric and tropospheric aerosols. Whitby (1973) showed that a multi-mode log-normal size distribution is observed for atmospheric aerosols generated by different physical processes. He introduced three mode: (1) the nucleation mode which is produced by gas-to-particle conversion, (2) the accumulation mode by coagulation and heterogeneous condensation, and (3) the coarse mode originating from the earth's surface. Patterson and Gillette (1977) confirmed the common feature of the aerosol size distribution is the multi-mode log-normal size distribution. Although the power law size distribution is certainly representing the general features of aerosols, bi-modal or tri-modal log-normal size distributions will be more general to describe the optical properties of aerosols, if we put more emphases on inversion results of optical remote sensing data such as Kondratyev et al. (1981), Nakajima et al. (1989), Shiobara et al. (1991), Kaufman et al. (1994), Remer et al. (1997) and so on. Those optically equivalent size distributions have common features such as a saddle point around $0.6\ \mu m$ reflecting in situ measured size distributions. Most of features of phase functions and optical thickness spectra can be simulated by bi-modal functions, rather than by power law functions.

With the above mentioned rationale, we introduce in this study a bi-modal log-normal volume spectrum for modeling the aerosol size distribution,

45

$$\frac{dV}{d\ln r} = \sum_{n=1}^{2} C_n \exp\left[-\frac{1}{2}\left(\frac{\ln r - \ln r_{m,n}}{\ln s_n}\right)^2\right], \tag{10}$$

where subscript n indicates the mode number. Table 1 lists r_m and σ for measured volume spectra. Averaging the tabulated values we adopt $r_{m.1} = 0.17$, $r_{m.2} = 3.44$, $s_1 = 1.96$, and $s_2 = 2.37$ for the parameters of the modeled volume spectrum in our retrieving scheme. Two undetermined parameters in Eq. (10), c_1 and c_2, can be determined from two channel satellite radiances. Equivalently we determine the aerosol optical thickness and the peak ratio of the bi-modal size distribution, $\gamma (=c_2/c_1)$. It should be noted that the peak ratio γ, which represents large concentration of large particles, can be related to the Ångströme exponent α defined as,

$$\alpha = -\frac{d\ln\tau_{a,\lambda}}{d\ln\lambda}. \tag{11}$$

The Ångström exponent α is approximately constant in visible spectral region since the optical thickness spectrum is approximately log-linear as a function of log (λ) for most of observed

Table 1 Parameters for the aerosol size distribution fitted to two term log-normal functions.

Reference	r_{m1}	s_1	r_{m2}	s_2	r_{m3}	s_3	memo
Patterson and Gillete	0.14	1.56	2.29	2.11			light aerosol loading
1977			2.84	1.90	35.5	1.38	moderate
			3.08	2.20	35.1	1.37	heavy
Fujimura and Hashimoto	0.41	1.36	2.3	1.65			at Morioka, in winter
1977	0.36	1.58					at Yokohama
Slinn, 1983	0.17	1.61					continental background
	0.19	1.64					urban pollutant
Tanaka et al., 1983	0.14	2.6					yearly averaged
Fitch and Cress, 1981	-.—	1.5					
Nakajima et al., 1986	0.13	1.8			10.0	2.6	
Shiobara et al, 1991	0.16	1.79	4.48	3.47			winter in Sendai
	0.17	1.69	2.78	3.06			spring in Sendai
	0.21	1.97	2.98	2.17			summer in Sendai
	0.15	1.96	3.96	3.12			autumn in Sendai
Whitdy, 1975	0.17	2.05	4.375	2.33	(0.0215	.74)	m=1.5-0.006i
Nilsson, 1979	0.175	2.34	3.41	2.23			
	0.205	2.23	4.09	2.23			
	0.189	2.12	3.41	2.23			
	0.174	2.01	4.09	2.23			
	0.196	2.01	4.09	2.23			

size distributions as many investigators have pointed out. Defining the mean Ångström exponent α for regular sunphotometer wavelengths, 0.368, 0.500, 0.675, 0.862, and 1.050 µm, the peak ratio γ can be translated to α as shown by Fig. 3. Retrieving the set of (τ_a, α) is more essential since the satellite-received radiance is not sensitive to the detailed structure of the size distribution, but depends nearly uniquely on (τ_a, α).

To calculate the phase function, single scattering albedo and the wavelength dependence of the aerosol optical thickness, we simply assume Mie particles with the size distribution Eq. (10) and the complex refractive index of $m = 1.5-0.005i$. Introduction of the aerosol absorption is important for successful retrievals of the aerosol optical thickness (Ignatov et al., 1995a, 1995b; Nakajima and Higurashi, 1996). The NOAA operational aerosol maps show that dust aerosols have a largest optical thickness the most significant aerosol type contributing to the global atmospheric turbidity. The averaged imaginary index of refraction of dust aerosols is in the range from 0.003 to 0.005 for shortwave spectral region (Patterson and Gillette, 1977; Carlson and Benjamin, 1980). Urban type aerosols also tend to have a large absorption (WCP, 1983; Shettle and Fenn, 1979; Tanaka et al., 1983; Hayasaka et al., 1992). The averaged value of imaginary index of refraction is in the range from 0.005 to 0.01. Ohta et al. (1996) measured the imaginary index of aerosols in the free atmosphere as 0.005 to 0.01 at the top of Mt. Lemmon, Arizona. Although we have prefix the aerosol complex refractive index as 1.5-0.005i in our algorithm, next generation algorithms can adopt more sophisticated
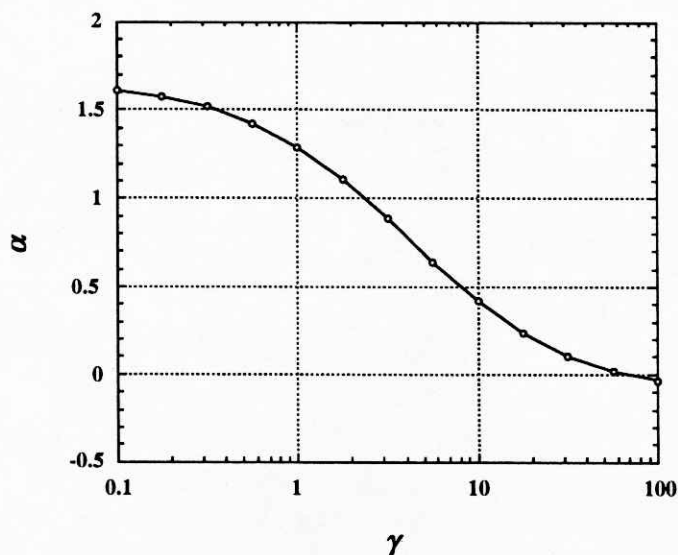

Fig. 3 The relationship between Ångström exponents and peak ratios of bi-modal size distributions.

algorithms for an automatic determination of aerosol types with recent and near-future multi-channel radiometers such as SeaWiFS, ADEOS / OCTS and EOS-AM1 / MODIS (Gordon, 1994; Fukushima and Toratani, 1997; Kaufman and Tanré, 1994).

4. 2. 3 Application to the remote sensing of AVHRR

For analyzing radiances in the visible and near infrared channel of AVHRR, we have to take into account the gaseous absorption by ozone, oxygen, and water vapor with the specific spatial and temporal distribution, especially for ozone and water vapor. Extensive numerical simulations have shown that the effect of gaseous absorption on the AVHRR-received radiances can be approximated by correction factors for ozone absorption t_{o3} and water vapor t_{H2O} as

$$R = t_{o3}t_{H_2O}R', \tag{12}$$

where R' is the reflectance with the gaseous absorption by other than ozone and water vapor, which are fixed with US-standard model in AFGL Lowtran-7, and t_{o3}, is given by

$$t_{o3} = exp\{-\tau_{o3}(1/\mu + 1/\mu_0)\}. \tag{13}$$

The formula Eq. (13) is understandable since ozone exists in the upper atmosphere and a simple correction with two way transmittance will be enough.

The correction for the water vapor absorption is more complicated. In our algorithm, we have tabulated the value of t_{H2O} as the ratio of the apparent reflectance with water vapor to that without water vapor for eight solar zenith angles ($\theta_0 = 0°$ (10°) 70°), six satellite zenith angles ($\theta = 0°$ (10°) 50°), seven relative azimuth angles ($\phi = 0°$ (30°) 180°), eight cases for τ_a (1.0E-10, 0.001, 0.01, 0.02, 0.1, 0.4, 1, 2), and ten cases for water vapor amount ($w = 0$, 0.04, 0.1, 0.2, 0.4, 1, 2, 4, 6, 10). In the calculations, we have applied a wavelength integration over the width of the response function of AVHRR with 15 wavelength grids for channel-1 and 22 grids for channel-2 that are set respectively for water vapor and oxygen band absorption. The aerosol size distribution is fixed at $\gamma = 1$ since the size distribution effect is not significant in the results. The accuracy is discussed in detail in Higurashi et al. (1997).

4. 2. 4 Construction of LUT

The coefficients in Eq. (9) depend on the geometry, i.e., θ_0, θ, and ϕ, the aerosol optical property, γ, and surface wind velocity, u_{10}. Figure 4 shows relative errors in the apparent reflectances at TOA when the dependence on the wind velocity is ignored in calculating Eq. (9) other than the term R_s for various geometries. We have assumed the wind velocity at 10 m above the sea surface as $u_{10} = 7$ m s^{-1} to calculate the multiple component in synthesizing the TOA reflectance for various conditions ($u_{10} = 1, 2, 7, 10, 15$ m s^{-1}). According to Fig. 4, the dependence of the TOA apparent reflectance on the wind velocity is mainly caused by the single scattering component.

We, therefore, assume $u_{10} = 7$ m s^{-1} for constructing the LUT which include the coefficients in Eq. (9) for 29 solar zenith angles ($\theta_0 = 0°$ (2.5°) 70°), 21 satellite zenith angles ($\theta = 0°$ (2.5°) 50°), and 23 relative azimuthal angles ($\phi = 0°$ (5°) 40°; 40° (10°) 180°), and 11 cases of the peak ratio ($\gamma = 0.1, 0.2, 0.5, 1, 2, 3, 5, 10, 20, 50, 100$). Figure 5 shows errors in R by approximation of Eq. (9) and interpolation for geometries on the whole sky at $\theta_0 = 60°$. The
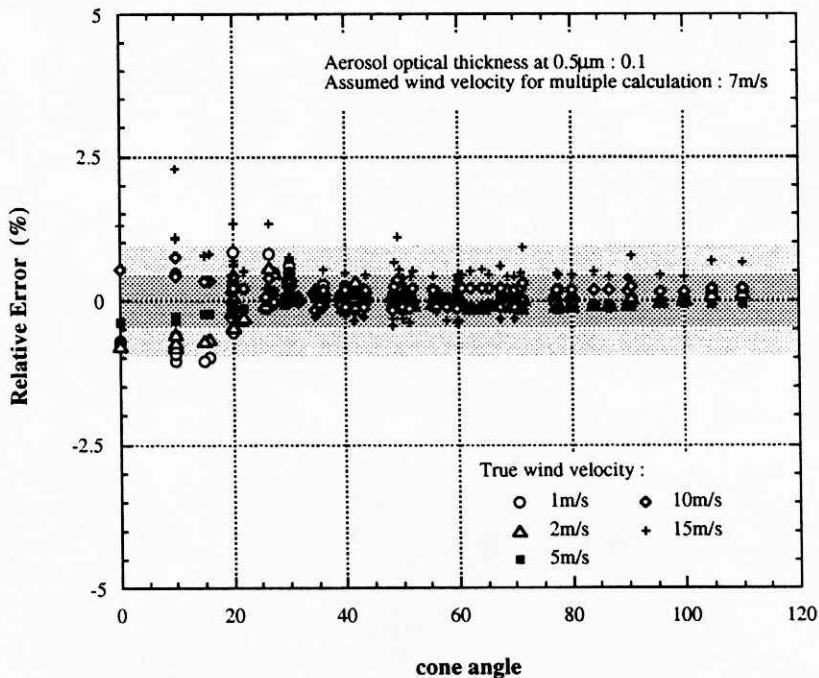

Fig. 4 Relative errors in the apparent reflectance at TOA synthesized with the multiple scattering components ignoring the dependence of the wind velocity, i.e., $u_{10} = 7$ m s^{-1}, for various geometries $0 < \theta_0 < 70, 0 < \theta < 45, 0 < \phi < 180$. Wind velocities for exact calculation are for $u_{10} = 1, 2, 5, 10,$ and 15 m s^{-1}.

$\phi = 180°$

$\phi = 90°$ $\phi = 90°$

$\phi = 0°$

-0.001   0.000   0.001

Absolute Error in Apparent Reflectance
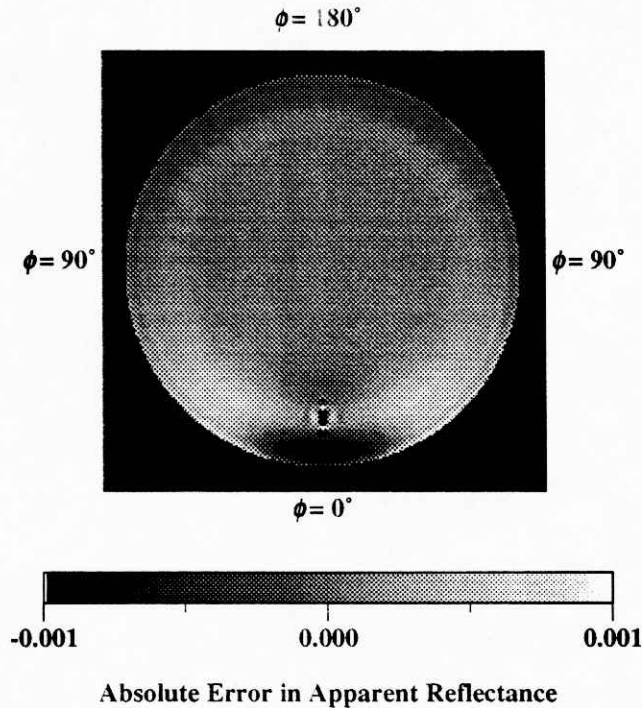
Fig. 5   The angular distribution of absolute errors in the apparent reflectance caused
by the approximation Eq. (9) and angular interpolations at $\theta_0 = 60°$.

figure shows the maximum error is less than 0.0007 except for the sun-glint region.

The water-leaving reflectance depends on the atmospheric turbidity and the ocean pigment
concentrations. It also has a strong dependence on wavelength and is very sensitive to the
pigment concentration in the region of weak absorption of water. In other spectral region, the
reflectance is almost unaffected by the pigment concentration in Case 1 water (Gordon and
Clark, 1981), whereas the upwelling reflectance from the ocean body is not small in Case 2
water. We ignore this upwelling reflectance in this study, because more than 98% of the
world ocean waters are presumably of Case 1 water. The effect of the reflection by foam,
which called whitecaps becomes large as the surface wind velocity increases. We avoid data
from analyses that u_{10} is grater than 15 m s^{-1} to ignore the white cap effect.

4. 3   Retrieval algorithm

Our algorithm for aerosol retrieval is based on look-up table (LUT) approach. Measured
radiances in channel-1 and -2 of AVHRR are compared with theoretical values which are
reconstructed from LUT for trial values of aerosol parameters.

50

4. 3. 1 Retrievals of aerosol optical parameters

The basis of retrieval is the characteristic relationship between apparent reflectances of AVHRR channel-1 and -2 for various values of the aerosol optical thickness at 0.5 μm τ_a and the peak ratio γ of the size distribution as shown in Fig. 6, which is caused by the difference of the extinction efficiency in each channel. The figure suggests that the aerosol optical parameters, i.e., τ_a and γ, are retrieved by comparing measured reflectances and theoretical reflectances which is obtained from LUT. In the sun-glint region, however, it is difficult to retrieve the aerosol optical parameters by this principle, since the relationship between two channel reflectances becomes complicated due to increasing contribution of directly reflected radiation by ocean surface (Nakajima and Higurashi, 1996).

Differences between reflectances in channel-1 for $\tau_a = 0.0$ and 0.1 are shown in Fig. 7 as a function of cone angles Θ', which is defined as the angle between the direction for specular reflection and the viewing direction,

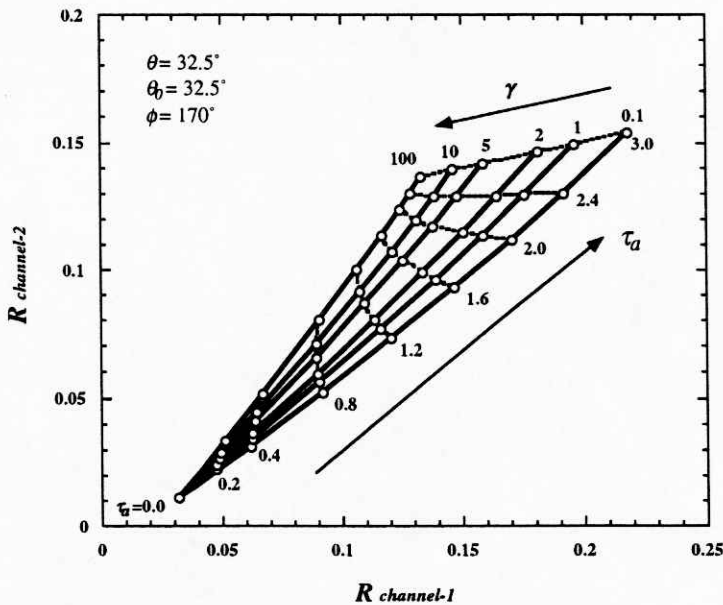$$cos\,\Theta' = -\mu\mu_0 + \sqrt{1-\mu^2}\sqrt{1-\mu_0^2}\,cos\,\phi. \tag{14}$$

Fig. 6 The relationship between apparent reflectances of NOAA / AVHRR channel-1 and -2 for various aerosol loading conditions. $\tau_a = 0, 0.2, 0.4, 0.8, 1.2, 1.6, 2.0, 2.4$, and 3.0; $\gamma = 0.1, 1, 2, 5, 10$, and 100; $\theta_0 = 32.5°$, $\theta = 32.5°$, and $\phi = 170°$.
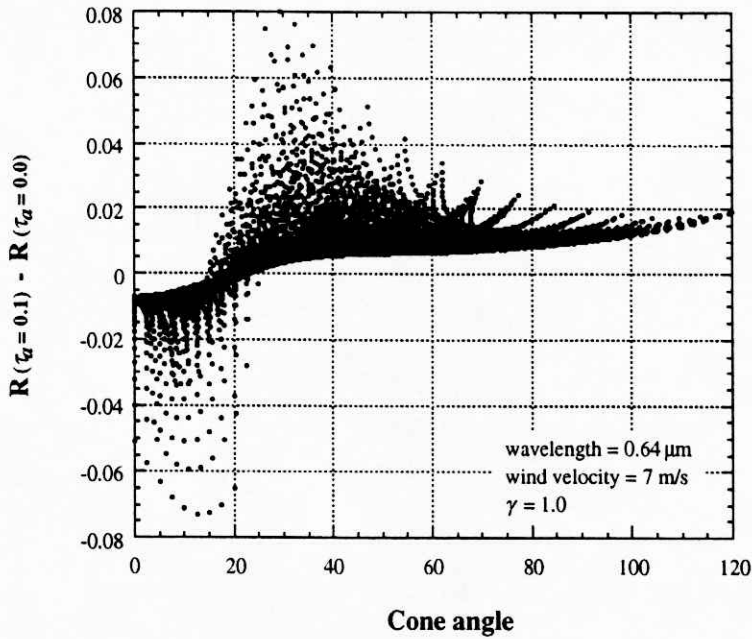
Fig. 7 Increases of the apparent reflectance with increasing optical thickness as a function of the cone angle. Values for various angular conditions are shown simultaneously.

In the figure table values are assumed for θ_0, θ and ϕ; $u_{10} = 7$ m s^{-1} and $\gamma = 1$. As explained above, the reflectance decreases with increasing optical thickness for $\Theta' < 20°$. It should be noted that a large increase of reflectance appears at $20° < \Theta' < 60°$, indicating the optical thickness can be effectively retrieved in this cone angle range. The sensitivity decreases with further increase in cone angle, indicating the optical thickness retrieval becomes difficult for large cone angles. An increase in the multiple scattering contribution is not significant for large emergent zentih angles. We regard the region of which $\Theta' < 25°$ as the sun-glint region and data in this region are excluded from the retrieval. Although we fixed 25° for all our analyses in this paper, data avoiding in the region of $\Theta' < 40°$ may be better for thin atmosphere case and for taking into account the error in assumed wind velocity.

Reflectances in channel-1 and -2 of AVHRR outside the sun-glint region are compared with theoretical values which are reconstructed from LUT for trial values of τ_a and γ. The optimal values of τ_a and γ, that minimize the root mean square deviation ε between observed and theoretical reflectances, are searched by an iteration method until ε becomes less than 0.0001 for each channel and each grid values of γ. If we couldn't get the accuracy after 20 times iterations, the data are exclude from the analysis. The peak ratio is then determined so that τ_a estimated from channel-1 and -2 agree with each other.

4. 3. 2 The accuracy of the retrieval

We investigate in Figs. 8 and 9 errors in retrieved values of the aerosol optical thickness and the Ångström exponent caused by the retrieval algorithm by numerical experiments. In these experiments, we assume table values at a grid point as test reflectance data and evaluate errors caused only by the inversion process. Other parameters are assumed as $w = 4.0$ g cm^{-2} and $u_{10} = 7$ m s^{-1}. Figure 8 shows that the retrieval error for aerosol optical thickness is less than ± 0.01 in most region. Although the accuracy for optically thin cases seems to be better than thick cases in Fig. 9, errors in radiometric calibration for obtaining the reflectance will cause a large retrieval error as shown by the small optical thickness region in Fig. 6. The retrieval error in α is less than ± 0.05 except for small cone angles, and become worse as the
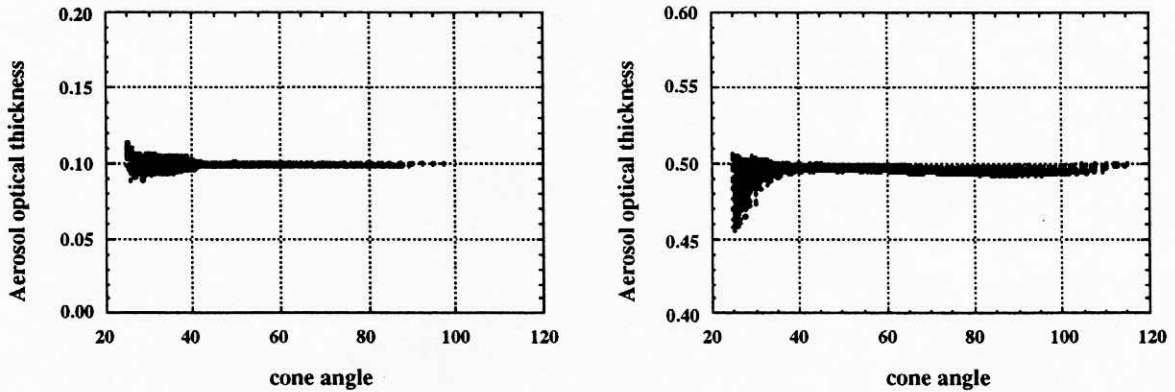
Fig. 8   The accuracy of retrieved aerosol optical thicknesses as a function of the cone angle. The true values are set as $\tau_a = 0.1$ and 0.5 with $\alpha = 1.29$.
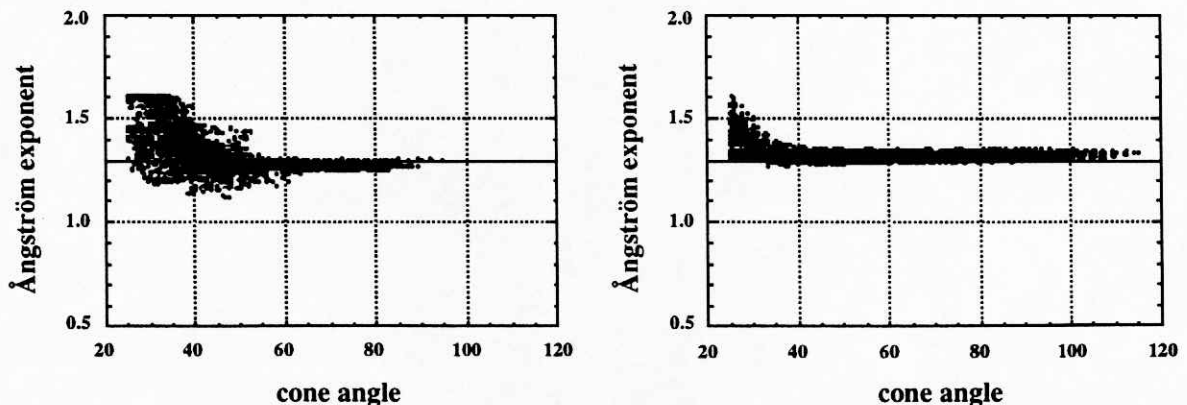
Fig. 9   The accuracy of retrieved Ångström exponents as a function of the cone angle. The true value is set as $\alpha = 1.29$ with $\tau_a = 0.1$ and 0.5.

optical thickness decreases due to the same reason as for optical thickness retrieval. It is more difficult to keep the accuracy of Ångström exponent retrieval than to keep the accuracy of optical thickness retrieval, because small differences of reflectances in channel-1 and -2 significantly affects the retrieval.

We also have to consider the water vapor effect affecting significantly on the Ångström exponent retrievals. If such an error becomes large, a use of a prescribed phase function according to some aerosol models may be better for optical thickness retrievals than a use of a adjusted phase function retrieved from the two channel algorithm. This will be especially true for optically thin aerosol layers. For thinner aerosol cases, we need to develop in future an automatic switching algorithm between two channel adjusted phase function or prescribed climate values.

4. 4 Global data analysis

4. 4. 1 Data sets

We apply the present retrieval algorithm to NOAA-9 AVHRR GAC (Global Area Coverage) data in January and July of 1988. To analyze global data efficiently without missing the global feature of aerosol characteristics, we make $1.5°$ grided segment data sets of AVHRR radiances in the region from $60°$N to $60°$S. Each $1.5°$ by $1.5°$ segment includes 10 by 10 pixels. One clear sky pixel data are selected out of 100 pixels through the following screening steps: 1) Avoid data that $\theta > 45°$ and $\theta_0 > 70°$, and data with $u_{10} > 15$ m s^{-1} to avoid the effect of whitecaps, and $\Theta' < 25°$ to exclude sunglint. 2) Screen out cloudy pixels above threshold values, i.e., $R_1 > 0.45$ or the brightness temperature for channel-4 T_{BB} less than 275K. 3) judge the remaining pixels to be suitable, if they consist of more than 40 pixels and the 30th reflectance of channel-1 from the lowest in remaining pixels is less than 0.2, and the standard deviation of reflections of remaining pixels is less than 0.02. 4) Then, select the third reflection of channel-1 from the lowest in the remaining pixels.

Our algorithm requires three ancillary data, i.e., total ozone amount, total water vapor amount, and surface wind velocity. Those data are obtained from TOMS girded ozone data provided by NASA Goddard Ozone Processing Team, ECMWF objective analysis data, and SSM/I derived data, which is produced by Robert Atlas and Joseph Ardizzone (NASA Goddard Space Flight Center).

4. 4. 2 Sensor calibration

Since the visible channel sensors of AVHRR have been degrading from the pre-launch calibration after the launch, a correction is necessary to reduce the retrieval error due to a calibration error. There have been persisting efforts for monitoring the calibration constants as a function of time (e. g., Che and Price, 1992; Holben et al., 1990; Kaufman and Holben, 1993). Most investigators use the following transformation formula of digital counts to radiances:

$$L_i = \alpha_i (C_i - C_{oi}),$$ (15)

where L_i is the spectral radiance detected by the sensor in channel-i ; C_i is the digital count value on a data tape; α_i is the calibration coefficient; C_{oi} is the deep space count for channel-i. Kaufman and Holben (1993) have proposed $C_{01} = 37.8$, $C_{02} = 39.0$, $\alpha_1 = 0.71$, and $\alpha_2 = 0.46$ for January and July of 1988.

For aerosol remote sensing, especially for thin aerosol layer cases, sensor calibration is a serious problem, because a small error in radiances may cause a large error in retrieved results

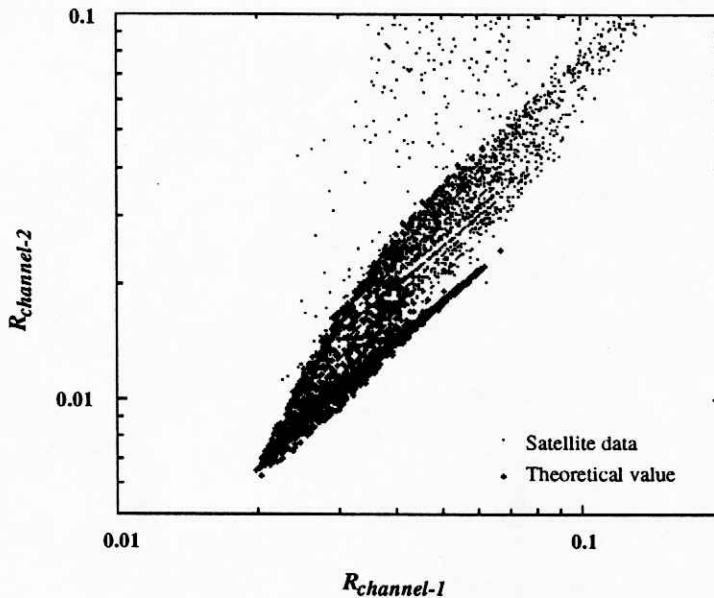Fig. 10 The distribution of minimum radiances in 1.5°×1.5° segments over globe. Circles show AVHRR data in channel-1 and -2 and dots show corresponding theoretical values without aerosol loading. Radiances are transformed from digital data by Eq. (15) with $C_{01} = 37.8$, $C_{02} = 39.0$, $\alpha_1 = 0.71$, and $\alpha_2 = 0.46$.

55

as indicated in Fig. 6. It is, therefore, desirable to investigate the validity of the assumed calibration constants for our retrieval scheme. Figure 10 plots the observed minimum reflections among clear sky pixels in each segment obtained with Kaufman and Holben's calibration constants against the theoretical minimum values that corresponds to no aerosol loading cases for each segment. The figure shows that calibrated satellite radiances with Kaufman and Holben's calibration constants fall within the theoretical region as a whole, suggesting that the calibration constants can generate consistent values of reflectance with our optical model. It should be noted that small changes in the calibration constants from the assumed values will cause intolerable modifications of the data region from the shown pattern in Fig. 10. Observed data points outside theoretical region have systematically larger reflectances in channel-2, indicating that those points had a cloud and/or whitecap contamination or other effects other than molecular scattering and surface reflection.

4. 4. 3 Results

We have applied the retrieval algorithms and calibration constants to the AVHRR GAC data for 10 days of January and July, 1988. 10 day composite is made by taking a mean value of the result we could retrieve in 10 days for each segment. Figure 11 shows 10 day composite of retrieved aerosol optical thickness in January and July of 1988. Due to the restriction on the solar zenith angle $\theta_0 < 70°$, there is no retrievals in mid and high latitudes of the winter hemisphere. It is found in Fig. 11 that there are several specific regions of large optical thickness off the west coast of North Africa, Arabian Peninsula, and the west coast of South Africa. Saharan dust particles form the largest aerosol layer off the west coast of North Africa extending across the Atlantic Ocean along the trade wind. The tongue of aerosol layer becomes dispersed shifting to south in January as compared with that in July. This seasonal change in aerosol loading pattern is consistent with the flow pattern of the surface wind fields used in retrievals as shown in Fig. 12. The aerosol layer off the west coast of South Africa in July also can be explained with wind field. Herman et al. (1996) has pointed out that these aerosols are caused by a biomass burning in the South African region. Those features have been found by NOAA operational aerosol products (Stowe et al, 1997), but it should be noted that the mean optical thickness is as large as twice the NOAA values. This difference may be caused by several differences in both algorithms, i. e., assumed size distribution, lower

56

January, 1988

July, 1988

0.0   0.5   1.0   1.5   2.0
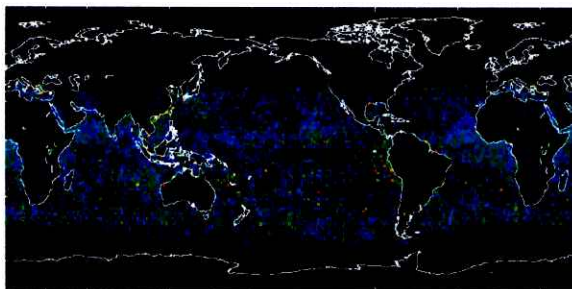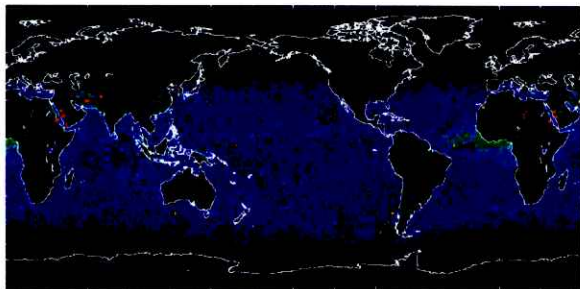
Aerosol Optical Thickness at 0.5 μm
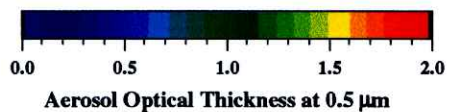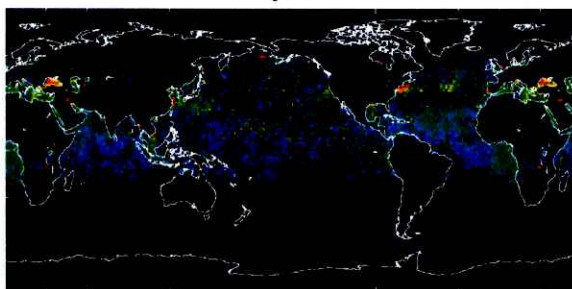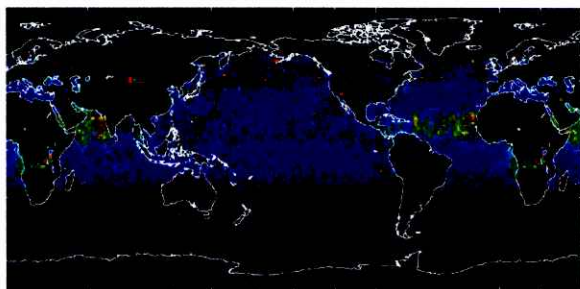
Fig. 11   The 10 day composite of retrieved aerosol optical thickness at 0.5 μm in January and July, 1988.

January, 1988

July, 1988

0.0   0.5   1.0   1.5

Ångström Exponent

Fig. 13   The 10 day composite of retrieved Ångström exponents in January and July, 1988.

January, 1988

July, 1988

0   5   10   15
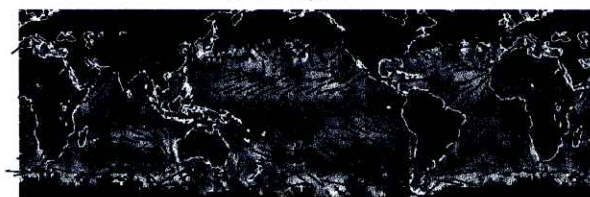
Surface wind velocity (m/s)

Fig. 12   Averaged surface wind velocities for the analyses shown in Fig. 11.

57

boundary condition for radiative transfer, cloud screening algorithm, calibration constants. We will need more comparison to confirm this difference in the retrieved values of optical thickness.

Figure 13 shows the distribution of the Ångström exponent corresponding to the retrieved optical thickness distribution shown in Fig. 12. Pixels with optical thickness less than 0.2 are masked, because retrieved Ångström exponents for thin optical thickness are uncertain, as noted in Fig. 9. Ångström exponents for optically thick region is about 0.5 off the west coast of North Africa and off Arabian Peninsula, and around 0.7 for the west coast of South Africa. A remarkable feature in Fig. 13 is that there are large Ångström exponent regions in July around Black Sea, off the east coast of North America around New York, and off the east coast of South China around Shanghai. Since those regions correspond to world's large industrial areas, it is highly possible large Ångström exponents in these regions are caused by small particles originating with anthropogenic pollutant. A closed comparison of aerosol optical thickness maps with Ångström exponent maps, we can recognize slight increases in the optical thickness in these regions. It will be possible by such comparison to evaluate the optical thickness increase due to anthropogenic aerosols.

4. 5 Discussion and Conclusions

We have obtained global distributions of aerosol optical thickness and Ångström exponent as our main results as shown in Figs. 11 and 13, applying the proposed algorithm to 10 day AVHRR GAC data sets. The spatial pattern of the optical thickness distribution is similar to the NOAA operational products, but the magnitude tends to be twice as large as NOAA products (Husar et al., 1997). As listed in the preceding section, there are significant differences between our algorithm and the NOAA operational algorithm, so that we have to be careful before drawing the final conclusion to the evaluation. There are some problems with our products as compared with NOAA products. Figure 11 shows an aerosol plume over the Arabian Sea extending to south-east in the July case, whereas the wind flow direction is rather north-east. One possible explanation is a contamination by whitecaps generated by the strong wind in this season. To study this point, we plot in Fig. 14 the aerosol optical thickness against the surface wind velocity in a region from 80°E to 100°W and from 60°N to 60°S including the Pacific Ocean and the eastern Indian Sea. The figure shows that the minimum

Pacific Ocean (80°E-100°W,60°N-60°S)
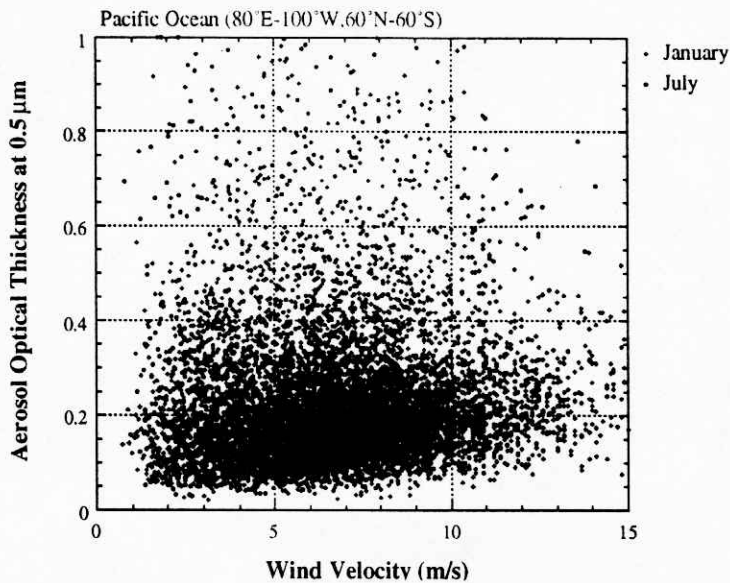
Fig. 14   Retrieved aerosol optical thicknesses plotted against the surface wind velocity
in a Pacific Ocean area (80°E - 100°W, 60°N - 60°S).

value of optical thickness for each wind velocity slightly increases with increasing wind velocity. This fact suggests that retrieved optical thicknesses may have contributions from whitecap and/or injected particles from roughened ocean. It should be noted, however, that this effect seems to be less than 0.1 in optical thickness for the wind velocity less than 15 m s⁻¹ and is unlikely to be the reason for the large optical thickness around the region. We will need a future ground truth for understanding the feature.

To see the validity of the optical properties thus obtained, relationships between aerosol optical thickness and Ångströme exponents are shown in Fig. 15 for six particular areas in July of 1988, i.e., the west coast of North African, the west coast of South Africa, the Black Sea, Mediterranean Sea, the east coast of North America, and the east coast of South China. Longitudes and latitudes of the regions are listed in Table 2. The figure shows that off the west coast of North Africa the Ångström exponent increases from about 0.3 to 0.5 with increasing optical thickness and is almost constant after reaching at 0.5. In this regions, the Ångströme exponent stay at small values due to large desert dust particles.

For the region off the west coast of South Africa, the Ångströme exponent is larger in the range from 0.5 to 0.7 with the maximum at optical thickness around 0.5. If those aerosols are of biomass burning origin as Herman et al. (1996) suggested, the value of the Ångström exponent is expected to be a rather small with a bi-modal feature of the aerosol size distribution

59
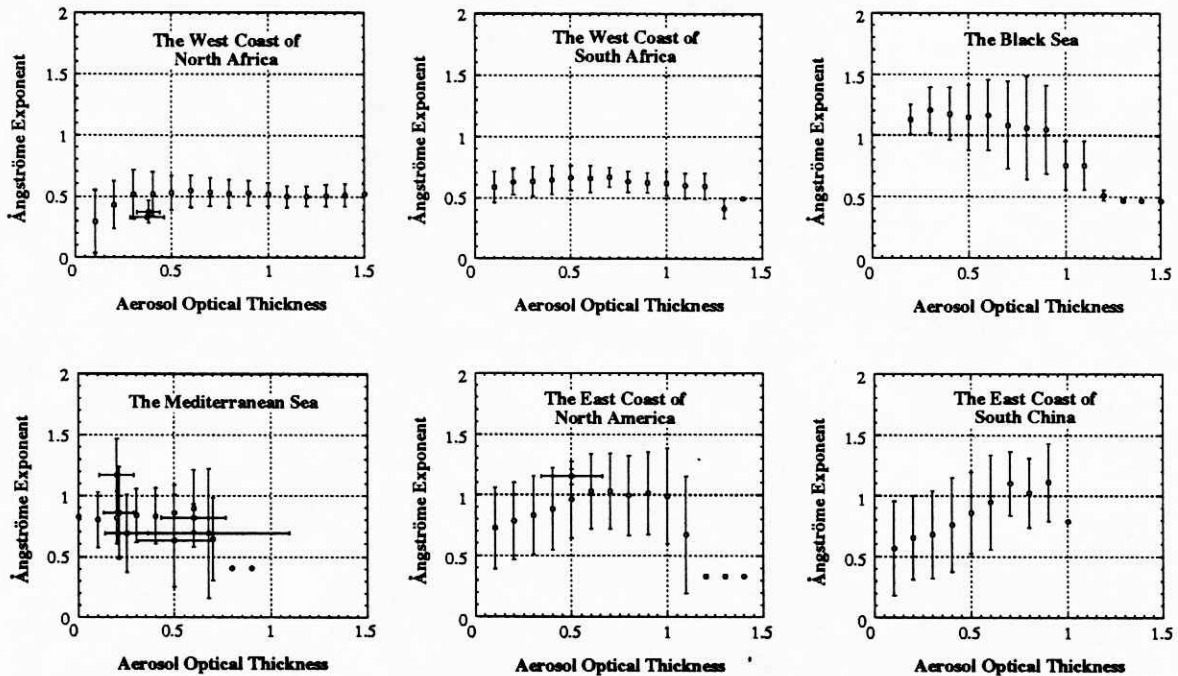
Fig. 15 Correlations between τ_a and α for 6 peculiar areas of the results in July, 1988, i.e., west coast of North African, west coast of South Africa, Black Sea, Mediterranean Sea, east coast of North America, and east coast of South China. Satellite derived values (circles) and ground based measurement values (dots) by several investigators listed in Table 3 are shown.

with both the accumulation and smoldering mode aerosols (Holben et al., 1997). It is also possible that there is a contribution from soil particles originating from the Kalahari desert. Therefore the characteristic dependence of the Ångströme exponent on the aerosol optical thickness is caused by a correlation between the accumulation mode and the large coarse particle mode attributed to soil or ash particles.

Table 2   Areas for analyses shown in Fig. 15.

Latitude		Longitude		memo
25° N	10° N	40° W	10° W	off the west coast of North Africa
20° N	10° N	60° W	40° W	
10° N	15° S	0° E	15° E	off the west coast of South Africa
50° N	40° N	25° E	45° E	Black sea
50° N	30° N	0° E	25° E	Mediterranean Sea
40° N	30° N	25° E	30° E	
45° N	35° N	80° W	60° W	off the east coast of North America
35° N	25° N	120° E	125° E	off the east coast of South China

In the regions on the Black Sea, off the east coast of North America, and off the east coast of South China, where are expected to be affected by anthropogenic pollutant, the Ångströme exponent tends to increase with increasing τ_a until α reaches around 1 and it decreases as τ_a increases further. This characteristic dependence of α on τ_a was also found with in situ measurement data for urban type atmospheres (Kaufman et al., 1996). The first increase of α corresponds to an increasing contribution of accumulation mode particles relative to the contribution from background aerosols. The decrease of α with further increase in optical thickness can be caused by particle growth due to water vapor uptake.

We overlay in Fig. 15 and Table 3 ground truth data by several investigators. Our results agree with the ground based measurements within the tolerance of uncertainties and errors associated with various measurement techniques. For the Mediterranean Sea, however, the agreement looks poor. In this region there are several aerosol sources with largely different Ångström exponents, i.e., Saharan desert dust, maritime particles, and urban aerosols from Europe, so that the Ångström exponent value may change significantly and may be difficult to be validated.

To our knowledge, only one previous retrieval of the global distribution of an aerosol size parameter is of Durkee et al. (1991). It is very interesting to compare our result with theirs. They found that the aerosol optical thickness and size parameter show marked differences between the Northern and Southern Hemispheres. They suggested this feature is consistent with Northern Hemispheric continental sources of small particles. It is difficult to see a

Table 3   Aerosol optical thicknesses (τ_a) at 0.5 μm and Ångström exponents (α) measured by several investigators for comparison with Fig. 15. σ and σ_α are root mean square deviations of measured τ_a and α.

Reference	Period of time	τ_a	σ	α	σ_α	Area
Villevalde et al. (1984)	17/07/83-30/07/83	0.50	0.20	0.63	0.38	Mediterranean Sea
Shifrein et al. (1985)	04/06/83-17/06/83	0.25	0.11	0.69	0.32	Mediterranean Sea
Deuze et al. (1988)	26/07/83-29/07/83	0.68	0.42	0.69	0.53	Mediterranean Sea
Volgin et al. (1988)	11/08/86-16/09/86	0.20	0.09	1.17	0.30	Mediterranean Sea
Zibordi et al. (1988)	28/05/83-01/06/83	0.60	0.17	0.82	0.11	Mediterranean Sea
Yershov et al. (1990)	25/06/88-22/07/88	0.21	0.08	0.86	0.38	Mediterranean Sea
Reddy et al. (1990)	06/05/88-12/05/88	0.37	0.09	0.33		Saharan dust
	30/08/88-31/08/88	0.38	0.06	0.37	0.09	Saharan dust
	16/07/88-04/08/88	0.50	0.16	1.15	0.06	North American air

similar phenomenon in our results. Durkee et al. (1991) also claimed that they have detected small DMS aerosols around the equator, whereas our results do not show such small aerosol particles in the region. Such differences in the two studies may be attributed to difference in the observation period. It should be noted, however, that there might be some effect from water vapor in the result of Durkee et al., since the water vapor correction of channel-2 radiance is very difficult and delicate. A significant discontinuity in their retrieval results at edges of scan lines shows some problems in their interpretation of the satellite-received radiances. We need a ground truth to explain these differences.

Although there are several unsolved problems as mentioned above, it is found that our look-up table method with NOAA AVHRR channel-1 and -2 radiances is sufficiently useful to depict global distributions of different aerosol types through aerosol optical thickness and Ångström exponent. The obtained distributions show that the majority of atmospheric aerosols originate from desert dust, biomass burning and human activities. Particularly, the loading of desert dust particles are conspicuously strong and its impacts extend broadly by long distance atmospheric transport. Although anthropogenic aerosols don't strongly contribute to the atmospheric turbidity as compared with desert dust, they can be clearly identified with the Ångströme exponent with significantly large values exceeding 1.0.

In the future, we have to estimate more detailed optical parameters, such as mode radii of the size distribution, composition and so on, using multi channel radiance data from advanced radiometers, such as ADEOS / OCTS, EOS-AM1 / MODIS, and ADEOS2 / GLI.

Acknowledgment

Sports and Culture; OCTS / GLI projects of the National Space Development Agency of Japan.

References

Atlas, R., and S. C. Bloom, 1989: Global surface-wind vectors resulting from the assimilation of satellite wind-speed data in atmospheric general circulation models. *OCEANS '89 Proceedings*, IEEE Publication Number 89CH2780-5, 260-265.

Atlas, R., S. C. Bloom, R. N. Hoffman, J. V. Ardizzone, and G. Brin, 1991: Space-based surface-wind vectors to aid understanding of air-sea interactions. *Eos Transactions, American Geophysical Union*, 72, 18.

Carlson, T. N., and S. G. Benjamin, 1980: Radiative heating rates for Saharan dust. *J. Atmos. Sci.*, **37**, 193-213.

Chandrasekhar, S., 1960: Radiative Transfer, pp393, *Dover,* New York.

Charlson, R. J., S. E. Schwartz, J. M. Hales, R. D. Cess, J. A. Coakley, Jr., J. E. Hansen, and D. J. Hofmann, 1992: Climate forcing by anthropogenic aerosols. *Science*, **255**, 423-430.

Deuze, J. L., C. Devaux, M. Herman, R. Santer, and D. Tanré, 1988: Saharan aerosols over the South of France: characterization derived from satellite data and ground based measurements. *J. Appl. Meteorol.*, **27**, 680-686.

Durkee, P. A., F. Pfeil, E. Frost, and R. Shema, 1991: Global analysis of aerosol particle characteristics. *Atmos. Environ.*, **25A**, 2457-2471.

Fukushima, H. and M. Toratani, 1997: Asian dust aerosol: Optical effect on satellite ocean color signal and a scheme of its correction and a scheme of its correction. *J. Geophys. Res*, **102**, 17119-17130.

Gordon, H. R. and D. K. Clark, 1981: Clear water radiances for atmospheric correction of coastal zone color scanner imagery. *Appl. Opt.*, **24**, 4175-4180.

Gordon, H. R. and M. Wang, 1992: Surface-roughness considerations for atmospheric correction of ocean color sensors. I: The Rayleigh-scattering component. *Appl. Opt.*, **31**, 4261-4267.

Gordon, H. R. and M. Wang, 1994: Retrieval of water-leaving radiance and aerosol optical thickness over the oceans with SeaWiFS: a preliminary algorithm. *Appl. Opt.*, **33**, 443-452.

Hansen, J. E. and A. A. Lacis, 1990: Sun and dust versus greenhouse gases: an assessment of their relative roles in global climate change. *Nature*, **346**, 713-719.

Hayasaka, T., T. Nakajima, S. Ohta, and M. Tanaka, 1992: Optical and chemical properties of urban aerosols in Sendai and Sapporo, Japan. *Atmos. Environ*, **26A**, 2055-2062.

Herman, J. R., P. K. Bhartia, O. Torres, C. Hsu, C. Seftor, and E. Celarier, 1996: Global distribution of UV-absorbing aerosols from Nimbuls-7/TOMS data. submitted to *J. Geophys. Res.*

Higurashi, A., T. Nakajima, and T. Tanaka, 1997: A study on synthesizing satellite-received radiances for aerosol and ocean color remote sensing. *submitting to Appl. Opt.*

Holben, B. N., T.F. Eck, I. SlutskerD. Tanré, J.P. Buis, A. Setzer, E. Vermote, J.A. Reagan, Y.J. Kaufman, T. Nakajima, F. Lavenu, I. Jankowiak, and A. Smirnov, 1997: Automatic Sun and Sky Scanning Radiometer System for Network Aerosol Monitoring. *Rem. Sens. Environ.*, in press.

Husar, R. B., J. M. Prospero, and L. L. Stowe, 1997: Characterization of tropospheric aerosols over the oceans with the NOAA advanced very high resolution radiometer optical thickness operational product. *J. Geophys. Res.*, **102**, 16889-16909.

Ignatov, A. M., L. L. Stowe, S. M. Sakerin, and G. Korotaev, 1995: Validation of NOAA/NESDIS satellite aerosol product over the North Atlantic in 1989. *J. Geophys. Res.*, **100**, 5123-5132.

Ignatov, A., L. Stowe, R. Singh, S. Sakerin, D. Kabanov, and I. Dergileva, 1995a: Validation of NOAA/AVHRR aerosol retrievals using sun-photometer measurements from R/V AKADEMIK VERNADSKY in 1991. *Adv. Space Res.*, **16**, 95-98.

Jones, A., D. L. Roberts, and A. Slingo, 1994b: A climate model study of indirect radiative forcing by anthropogenic sulfate aerosols. *Nature*, **370**, 450-453.

Junge, C. E., 1969: Comments on " Concentration and Size Distribution Measurements of Atmospheric Aerosols and a Test of the Theory of Self-Preserving Size Distributions". *J. Atmos. Sci.*, **26**, 603-608.

Kaufman, Y.J. and B. N. Holben, 1993: Calibration of the AVHRR visible and near-IR bands by atmospheric scattering, ocean glint and desert reflection. *Int.J.Rmote Sensing*, **14**, 21-52.

Kaufman, Y.J. and B. N. Holben, 1996: Hemispherical backscattering by biomass burning and sulfate particles derived from sky measurements. *J. Geophys. Res.*, **101**, 19433-19445.

Kaufman, Y. J., and T. Nakajima, 1993: Effect of Amazon Smoke on Cloud Microphysics and Albedo - Analysis from Satellite Imagery. *J. Appl. Meteor.*, **32**, 729-744.

Kaufman, Y. J., and D. Tanré, 1994: Algorithm for remote sensing of tropospheric aerosol from MODIS: Optical thickness over land and ocean and aerosol size distribution over the ocean. MODIS ATBD.

Kaufman, Y. J., R. S. Fraser, and R. A. Ferrare, 1990: Satellite Measurements of Large - Scale Air Pollution: Methods, *J. Geophys. Res.*, **95**, 9895-9909.

Kaufman, Y.J. , A. Gitelson, A. Karnieli, E. Ganor, R. S. Fraser, T. Nakajima, S. Mattoo, B. N. Holben, 1994: Size distribution and scattering phase function of aerosol particles retrieved from sky brightness measurements. *J. Geophys. Res.*, **99**, 10341-10356.

Kiehl, J. T., and B. P. Briegleb, 1993: The relative roles of sulfate aerosols and greenhouse gases in

climate forcing. *Science*, **260**, 311-314.

Kneizys, F. X., E. P. Shettle, L. W. Abreu, J. H. Chetwynd, G. P. Anderson, W. O. Gallery, J. E. A. Selby, and S. A. Clough, 1988: Users Guide to LOWTRAN 7. AFGL-TR-88-0177.

Koepke, P, 1984: Effective reflectance of oceanic whitecaps. *Appl. Opt.*, **23**, 1816-1824.

Kondratyev, K. Ya., R. M. Welch, S. K. Cox, V. S. Grishechkin, V. A. Ivanov, M. A. Prokofyev, V. F. Zhvalev and O. B. Vasilyev, 1981: Determination of vertical profiles of aerosol size spectra from aircraft radiative flux measurements. 1. Retrieval of spherical particle size distribution. *J. Geophys. Res.*, **86**, 9783-9793.

Li, X., H. Maring, D. Savoie, K. Voss, and J. M. Prospero, 1996: Dominance of mineral dust in aerosol light-scattering in the North Atlantic trade winds. *Nature*, **380**, 416-419.

Nakajima, T., and H. Fukushima , 1996 : Development of radiance tables for aerosol remote sensing. Annual Report for the OCTS Sensor Team in 1996. National Space Development Agency of Japan.

Nakajima, T., and A. Higurashi, 1996: AVHRR remote sensing of aerosol optical properties in the Persian Gulf region, the Summer of 1991. *J. Geophys. Res.,* **102**, 16935-16946.

Nakajima, T., and M. Tanaka, 1983: Effect of wind-generated waves on the transfer of solar radiation in the atmosphere-ocean system. *J. Quant. Spectrosc. Radiat. Transfer*, **29**, 521-537.

Nakajima, T. and M. Tanaka, 1986: Matrix formulations for the transfer of solar radiation in a plane-parallel scattering atmosphere. *J. Quant. Spectrosc. Radiat. Transfer*, **35**, 13-21.

Nakajima, T. and M. Tanaka, 1988: Algorithms for radiative intensity calculations in moderately thick atmospheres using a truncation approximation. *J. Quant. Spectrosc. Radiat. Transfer*, **40**, 51-69.

Nakajima, T., M. Tanaka, M. Yamano, M. Shiobara, K. Arao and Y. Nakanishi, 1989: Aerosol optical characteristics in the yellow sand events observed in May, 1982 in Nagasaki - Part II Model. *J. Meteor. Soc. Japan*, **67**, 279-291.

Ohta, S., M. Hori, N. Murao, S. Yamagata, and K. Gast, 1996: Chemical and optical properties of lower tropospheric aerosols measured at Mt. Lemmon in Arizona. *J. Global Environ. Eng.*, **2**, 67-78.

Patterson, E. M. and D. A. Gillette, 1977: Commonalities in measured size distributions for aerosols having a soil-derived component. *J. Geophys. Res.*, **82**, 2074-2082.

Patterson, E. M., D. A. Gillette, and B. H. Stockton, 1977: Complex index of refraction between 300 and 700 nm for Saharan aerosols. *J. Geophys. Res.*, **82**, 3153-3160

Reddy, P. L., F. W. Kreiner, J. J. DeLuisi, and Y. Kim, 1990: Aerosol optical depths over the Atlantic derived from shipboard sunphotometer observations during the 1988 global change expedition. *Global Biogeochem. Sycles,* **4**, 225-240.

Remer,L., S.Gasso, D.Hegg, Y.Kaufman, and B.Holben, 1997: Urban/industrial aerosol: Ground-based Sun/sky radiometer and airborne in situ measurements. *J. Geophys. Res.*, **102**, 16849-16859.

Shi, G. Y., J. D. Guo, X. B. Fan, B. Wang, and L. X. Wang, 1994: Climate change and its causes. *Proc. International cof. Regional Environment and climate Change in east Asia.*

Shettle, E. P, and R. W. Fenn, 1979: Models for the aerosols of the lower atmosphere and the effects of humidity variations on their optical properties. AFGL-TR-79-0214, 20 Sept 1979.

Shiobara, M., T. Hayasaka, T. Nakajima and M. Tanaka, 1991: Aerosol monitoring by use of a scanning spectral radiometer in Sendai, Japan. *J. Meteor. Soc. Japan*, **69**, 57-70.

Shifrin, K. S., V. M. Volgin, B. N. Volkov, O. A. Yershov, and A. V. Smirnov, 1985: Optical depth of atmospheric aerosol over the sea, Issledovanie Zemli iz kosmosa, 2, N4, 21-30 (English Transl. *Soviet Journal of Remote Sensing*, **5(4)**, 591-605, 1989)

Smirnov, A., O. Yershov, Y. Villevalde, 1995: Measurement of aerosol optical depth in the Atlantic Ocean and Mediterranean Sea. *Proc. of EUROPTO* Paris, France, 27-28, September 1995, SPIE, 2582, 203-214 (Edit. by Santer, R. P, Atmospheric Sensing and Modeling II).

Stowe, L. L., R. M. Carey, and P. P. Pellegrino, 1992: Monitoring the Mt. Pinatubo aerosol layer with NOAA / 11 AVHRR data. *Geophys. Res. Lett.*, **19**, 159-162.

Tanaka, M., T. Takamura and T. Nakajima, 1983: Refractive index and size distribution of aerosols as estimated from light scattering measurements. *J. Climate Appl. Meteor.*, **22**, 1253-1261.

Taylor, K. E., and J. E. Penner, 1994: Response of the climate system to atmospheric aerosols and greenhouse gases. *Nature*, **369**, 734-737.

Tegen, I., A. A. Lacis, and I. Fung, 1996: The influence on climate forcing of mineral aerosols from disturbed soils. *Nature*, **380**, 419-422.

Toon, O. B., and J. B. Pollack, 1976: A Global Average Model of Atmospheric Aerosols for Radiative Transfer Calculations. *J. Appl. Meteor.*, **15**, 225-246.

Towmey, S., 1977: The influence of pollution on the shortwave albedo of clouds. *J. Atmos. Sci.*, **34**, 1149-1152.

Villevalde, Y. V., K. S. Lamden, and A. V. Smirnov, 1984: The results of maritime atmospheric spectral transmittance measurements (abstract) (in Russian), in VIII all-union symposium on laser and acoustic soundings of the atmosphere, part 1, pp.111-113, Institute of Atmospheric Optics, Tomsk.

Volgin, V. M., O. A. Yershov, A. V. Smirnov, and K. S. Shifrin, 1988: Optical depth of aerosol in typical sea areas. *Izv, Acad. Sci. USSR Atmos. Oceanic Phys.*, Engl. Transl., **24**, 272-277.

Wang, M. and H. R. Gordon, 1993: Retrieval of the columnar aerosol phase function and single-scattering albedo from sky radiance over the ocean: simulations. *Appl. Opt.*, **32**, 4598-4609.

WCP(World Climate Programme), 1983: Report of the experts meeting on aerosols and their climatic

effects, Williansburg, Virginia, 28-30 March 1983. (edited by Deepak, A. and H. E. Gerber) WMO-ICSU WCP-55.

Whitby, K. T., 1978: The physical characteristics of sulfur aerosols. *Atmos. Environ.,* **12**, 135-159.

Yershov, O. A., A. V. Smirnov, and K. S. Shifrin, 1990: Spectral transparency and solar halo in the atmosphere above the ocean. *Izv. Acad. Sci. USSR Atmos. Oceanic Phys., Engl. Transl.,* **26**, 287-292.

Zibordi, G., and G. Maracci, 1988: Determination of atmospheric turbidity from remotely-sensed data: A case study. *Int. J. Remote Sensing,* **9**, 1881-1894.

Chapter 5

A Global Characterization of Aerosols with a Two Channel Remote Sensing

5 A Global Characterization of Aerosols with a Two Channel Remote Sensing

Abstract

Global distributions of the aerosol optical thickness and Ångström exponent are estimated from NOAA (National Oceanic and Atmospheric Administration) / AVHRR (Advanced Very High Resolution Radiometer) channel-1 and -2 radiances for four months in 1990. Global distributions of those Ångström parameters are consistent with our knowledge on the distributions of desert-derived, biomass-burning, and anthropogenic pollutant aerosols obtained by ground-based and aircraft measurements. Especially, it is found that thin anthropogenic aerosols can be identified with large Ångström exponent values around the east coast of North America, Europe, the east Asia, and so on. Satellite-retrieved values of Ångström parameters are further validated with measured spectral optical thickness obtained by the NASA (National Astronautics and Space Administration) AERONET (AEerosol RObotic NETwork) sky radiometer network.

5. 1 Introduction

Aerosol monitoring on global scale is essential for evaluating the aerosol radiative effects reflecting the solar radiation back to the space (Kiehl and Briegleb, 1993; Taylor and Penner, 1994) and its influence on the cloud albedo (Twomey et al., 1984; Kaufman and Nakajima, 1993), of which climate effect is one of the greatest uncertainties in climate modeling (IPCC95, 1996). The total aerosol radiative forcing has been evaluated to be almost equal but with sign opposite to that of the forcing by greenhouse gases. They, however, will not offset each other and generate a complex impact on climate (Mitchell et al., 1995; Santer et al., 1996), because the aerosol distribution in concentration and composition have strong spatial and temporal variations, causing a significant difference in radiative forcing. Early studies of such effects have focused on anthropogenic aerosols, which are believed to exert a substantial cooling effect due to their high light-scattering efficiency (Charlson et al, 1992; Kiehl and Briegleb, 1993; Taylor and Penner, 1994). On the other hand, recent attention has been paid to mineral

dust, especially originating from a change in land-use, because of its large contribution to the atmospheric aerosol loading and its large absorption of solar radiation (Tegen et al, 1996; Li et al., 1996; Sokolik and Toon, 1996).

To fully understand these climate effects of aerosols, the aerosol characteristics, such as concentration, size distribution, composition, and optical properties, have to be determined on global scale. Measurements at ground-based stations have given us an important information about aerosol physical and chemical properties in detail, though the global scale behavior of aerosols will not be assessed from such ground-based measurement data alone, due to the strong spatial and temporal variabilities of aerosol properties. This recognition motivates us to use satellite remote sensing techniques for evaluation of the aerosol climate forcing, since satellite retrievals can generate spatially and temporally homogeneous global distributions of aerosol parameters. Present satellite retrievals are limited, however, mainly to estimation of the aerosol optical thickness, which corresponds to the column total aerosol cross section, from one or two channels of polar orbiters, e.g., NOAA / AVHRR, and geostationary satellites, e.g., Meteosat, (Stowe et al, 1991; Durkee et al., 1991; Moulin et al., 1997). In these algorithms, an aerosol model for deriving the aerosol optical thickness has to be assumed. Extending these algorithms, a two channel algorithm have been developed recently for retrieving the Ångström parameters, i. e., the aerosol optical thickness at wavelength of 0.5 μm and Ångström exponent, simultaneously to reproduce the observed radiances in the two channels (Higurashi and Nakajima, 1997; Higurashi et al., 1997).

This two channel algorithm, applied to NOAA AVHRR radiance data, has derived characteristic distributions of small and large aerosol particles of different aerosol origins. As studied in Higurashi and Nakajima (1997) and Higurashi et al. (1997), however, retrievals are sensitive to many assumptions made in the algorithms, such as calibration constants, water vapor absorption correction and so on. It is, therefore, highly necessary to study the retrieval results in detail to see if the results are reasonable as compared with our knowledge of spatial and temporal distributions of aerosol characteristics. For this purpose, we present in this paper four months analyses of Ångström parameters obtained by our two channel algorithm. Global distributions and seasonal variations of the parameters will be obtained and discussed in detail. We will further compare the results with ground-based measurement data of aerosol optical thicknesses obtained by the NASA AERONET (AEerosol RObotic

70

NETwork) sky radiometer network.

5. 2 Procedure of satellite data analyses

We have developed a two channel algorithm in order to derive Ångström parameters (τ_a, α) defined by the following Ångström's law,

$$\tau_{a,\lambda} = \tau_a (\lambda / 0.5)^{-\alpha}, \tag{1}$$

where λ and $\tau_{a,\lambda}$ are wavelength and aerosol optical thickness at λ. Since the detailed description of the retrieval algorithm is found in Higurashi and Nakajima (1997) and Higurashi et al. (1997), we present in this section a brief overview of the procedure used in the present data analyses.

In this study, τ_a and α are estimated from the relationship between channel-1 and -2 radiances of NOAA-11 AVHRR, which are calculated by an accurate yet efficient look-up table method simulating the band-averaged satellite-received radiances in atmosphere-ocean systems. We assume $1.5-0.005i$ for the aerosol refractive index and the following bimodal size distribution,

$$\frac{dV}{d\ln r} = \sum_{n=1}^{2} c_n e^{-\frac{1}{2}\left[\frac{\ln(r/r_{m,n})}{\ln s}\right]^2}. \tag{2}$$

We adopt $r_{m,1} = 0.17\mu m$, $r_{m,2} = 3.44\mu m$, $s_1 = 1.96$ and $s_2 = 2.37$ as typical climate values of parameters for the size distribution. Although τ_a and the peak ratio, $\gamma (= c_2 / c_1)$, are variables in the algorithm, τ_a and α are finally retrieved because γ is uniquely transformed to α, which is a more inherent parameter for radiation transfer processes. In practice, Ångström parameters are obtained by a regression fitting to the spectral optical thicknesses $\tau_{a,\lambda}$ at regular sunphotometer wavelengths, 0.368, 0.500, 0.675, 0.862, and 1.050μm.

The algorithm corrects satellite-received radiances for ozone absorption using daily TOMS retrieval data and for water vapor absorption and surface reflectance by assuming a rough-ocean surface with NCEP objective analyses data. To avoid solar specular reflection from the ocean surface, data within 30° half cone angle around the specular reflectance angle are excluded from the analyses. Also, we except data with high wind speed at 10m above the

71

ocean surface, i.e., $u_{10} > 12$ m/s, from the analyses to avoid the effect of reflection by foam. In the calculation of radiances, the polarization effect is taken into account, because it spoils the wavelength dependence of radiances and thus causes a serious error in the retrieved results, especially α, which is estimated with the relationship between channel-1 and -2 radiances.

5. 3   Validation

5. 3. 1   Ground based measurements

For validation of the retrieved results obtained by the present retrieval algorithm, we use AERONET data set, although the period of comparison is different as shown later. It was difficult for us to collect other worldwide ground-based measurement data for validation in the satellite analysis year, i. e., 1990. The AERONET is a ground-based aerosol monitoring network consisting of many automatic sun-sky scanning spectral radiometer stations of which data are transmitted to the data center at NASA GSFC (Goddard Space Flight Center) (Holben et al, 1997). From the direct solar and sky radiance data, aerosol spectral optical thicknesses at $\lambda = 0.340$, 0.440, 0.670, and 1.020 μm and size distributions are derived by an inversion algorithm of Nakajima et al. (1996). Retrieved results are opened to the public through the world wide web.

We selected stations on a island or on the coast in AERONET data set as listed in Table 1 and shown in Fig. 1 for comparing with satellite-derived results over the ocean. From daily-mean spectral aerosol optical thickness at 0.340, 0.440, 0.670, and 1.020 μm at the selected stations, we calculated the aerosol optical thickness at 0.5 μm and Ångström exponent with Eq. (1). The period of archived AERONET data set is after 1994 and most stations have started after 1996. Although the period of satellite retrievals in this study, 1990, dose not agree with that of AERONET ground-based measurements, we compare monthly mean values of Ångström parameters, expecting monthly mean values will reflect the mean aerosol characteristics in the region without a significant dependence on the year of measurements. Table 1 lists the monthly mean aerosol optical thickness at 0.5 μm $\tau_{a.gr}$ and Ångström exponent α_{gr} calculated from daily mean values at each station.

72

Fig. 1 Locations and names of selected AERONET stations for validation of the present satellite retrievals shown by closed circles and italic characters. Rectanguls show regions for which monthly regional averages of τ_a and α are calculated.

73

Table 1 Ångström parameter values for selected AERONET data for validation. Locations and archived periods are also shown.

Stations	Lat.	Lon.	$\tau_{a,gr}$				α_{gr}				Archived period
			Jan.	Apr.	Jul.	Oct.	Jan.	Apr.	Jul.	Oct.	
Ascension Island	7.58' S	14.24'W	-.--	0.157	0.139	0.420	-.--	0.687	0.877	0.636	Mar. - Dec. 1996
Barbados	13.00'N	60.00'W	0.118	0.142	0.358	-.--	0.086	0.154	-0.066	-.--	May, Sep. - Oct, Dec. 1996 - Jul. 1997
Bermuda	32.22'N	64.41'W	-.--	0.449	0.310	0.251	-.--	0.862	0.710	0.655	Mar. - Nov. 1996
Cabo Verde	16.43'N	22.56'W	0.298	0.263	0.648	0.306	0.010	0.015	0.009	-0.031	Oct. 1994; May 1995; Oct. 1996 - Jun. 1997
Dry Tortugas	24.36'N	82.47'W	-.--	0.284	0.346	-.--	-.--	0.789	0.486	-.--	Mar. - Oct. 1996; Jun. - Jul. 1997
Guadeloupe	16.00'N	58.30'W	-.--	0.106	-.-	-.--	-.--	0.020	-.--	-.--	Mar. - Apr. 1996
Izana	28.18'N	16.18'W	-.--	-.--	0.196	-.--	-.--	-.--	0.647	-.--	Jun. - Jul. 1996
Lanai	20.49'N	156.59'W	0.284	0.253	0.076	0.098	0.549	0.550	0.331	0.530	Nov. 1995 - Dec. 1996; Jul. 1996
Male	04.11'N	73.31'E	-.--	0.267	0.383	0.706	-.--	0.775	0.471	0.159	Sep. 1996 - Apr. 1997
Sandy Hook	40.26'N	73.59'W	-.--	-.--	0.355	-.--	-.--	-.--	1.284	-.--	May - Sep., 1996
St Nicolas	33.19'N	119.30'W	-.--	-.--	0.080	-.--	-.--	-.--	1.034	-.--	Jun. - Jul. 1996
Tromelin	15.53' S	54.31'E	-.--	-.--	0.282	0.392	-.--	-.--	0.090	0.055	Jul. - Nov. 1996
Wallops	37.56'N	75.28'W	-.--	-.--	0.507	-.--	-.--	-.--	1.176	-.--	Aug. - Sep. 1995; Jul. - Aug. 1996

74

5. 3. 2 Comparison between satellite and ground-based measurements

We apply the retrieval algorithm to NOAA-11 / AVHRR GAC (Global Area Coverage) data in January, April, July, and October 1990. For efficient analyses of global data, we segment the region from 60°S to 60°N into 0.5° x 0.5° latitude-longitude boxes and bin 10 x 10 pixels into each box. A clear pixel for the analysis is selected out of the 100 pixels with the cloud-screening process of Higurashi and Nakajima (1997).

Figure 2 compares ground-based measurement values of Ångström parameters ($\tau_{a.gr}$, α_{gr}) with coincident AVHRR-derived values ($\tau_{a.sat}$, α_{sat}), which are averages of 5 x 5 monthly mean segment values in the region of 2.5° x 2.5° centered at the location of each station. Even though the dispersion of the correlation is large, especially for τ_a, due to disagreement of the analyzed period, they are consistent with each other except for the retrieved results for $\alpha_{gr} <$ 0.2, as shown in Fig. 2. From Table 1, it is found that those small Ångström exponent values are mostly from stations influenced by Saharan dust, such as Cabo Verde and Barbados. As discussed below, there are several possible causes for the overestimation of small α (< 0.2) by satellite remote sensing, such as errors involved in the calibration constants of the radiometer, the aerosol model (size distribution and complex refractive index) and so on.
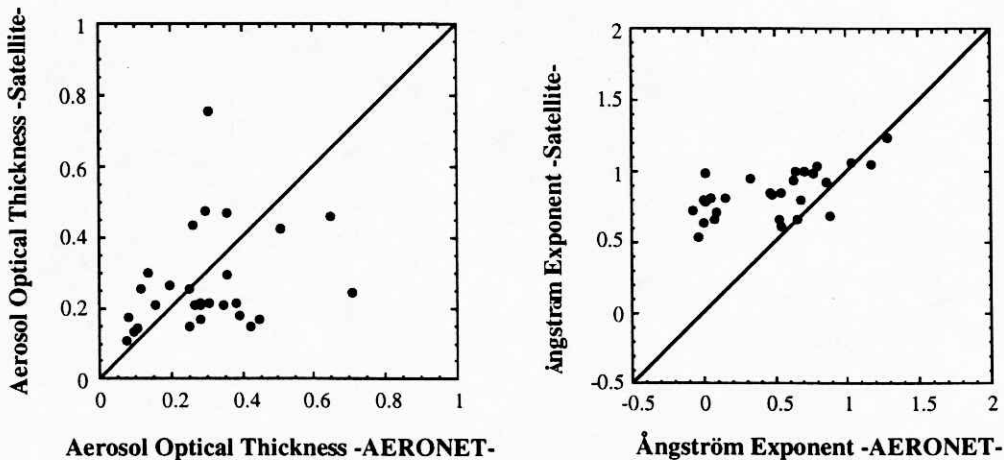

Fig. 2   The correlation between ground-based and satellite derived τ_a and α with calibration constants 'case-1' and $r_{m,1} = 0.17$, $r_{m,2} = 3.44$, $s_1 = 1.96$, and $s_2 = 2.37$ for assumed bimodal size distribution.

5. 3. 2. 1 Aerosol size distribution

In the present algorithm, γ is the only one adjustable parameter to describe the difference in the aerosol size distribution with fixed r_m and s for accumulation and coarse modes of the bimodal size distribution. To investigate the influence of the size distribution parameters, r_m and s, we perform sensitivity tests of channel-1 and -2 radiances of AVHRR for a change in the parameters $r_{m.1}$, $r_{m.2}$, s_1, and s_2. Figure 3 (a), (b), (c), and (d) show the results of four sensitivity tests with parameter changes: $r_{m.1} = 0.10$ and 0.17; $s_1 = 1.30$, 1.50 and 1.96; $r_{m.2} = 3.44$, 6.0, and 10.0; $s_2 = 2.37$ and 2.75. Other parameters are fixed at reference values as $r_{m.1} = 0.17$, $s_1 = 1.96$, $r_{m.2} = 3.44$, $s_2 = 2.75$, respectively. In these calculations, we set solar

Fig. 3 Sensitivity tests with size distribution parameter changes: (a) $r_{m.1} = 0.10$ and 0.17; (b) $s_1 = 1.30$, 1.50 and 1.96; (c) $r_{m.2} = 3.44$, 6.0, and 10.0; (d) $s_2 = 2.37$ and 2.75. Othrer parameters are fixed at reference values as $r_{m.1} = 0.17$, $s_1 = 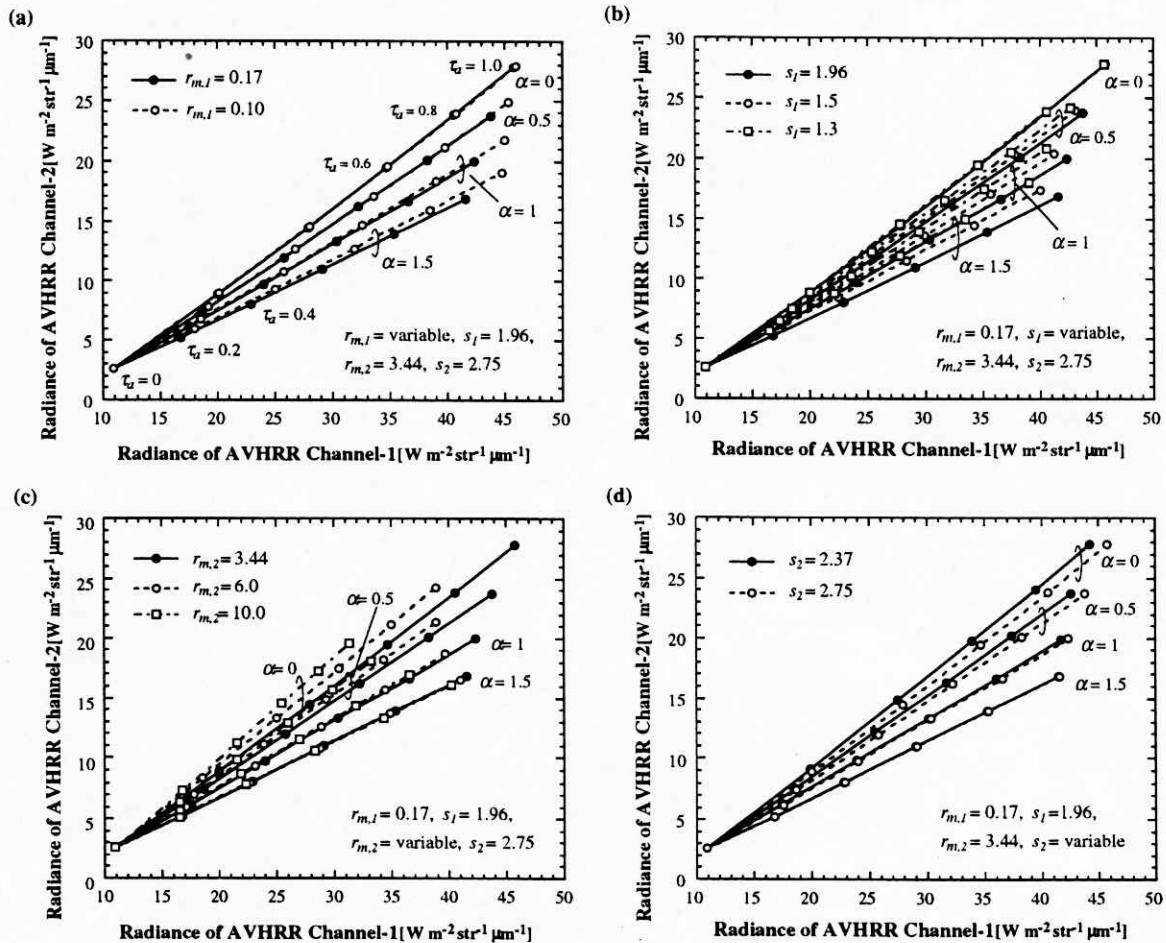1.96$, $r_{m.2} = 3.44$, $s_2 = 2.75$, respectively. $\theta_0 = 40°$, $\theta = 30°$, $\phi = 150°$; $u_{10} = 7$m/s; $\tau_a = 0$ (0.2) 1.0, $\alpha = 0$ (0.5) 1.5.

76

zenith angle $\theta_0 = 40°$, satellite zenith angle $\theta = 30°$, azimuth angle $\phi = 150°$, $u_{10} = 7$m/s, $\tau_a = 0$ (0.2) 1.0, and $\alpha = 0$ (0.5) 1.5.

Shifting the mode radii of accumulation mode and coarse mode toward smaller values, radiances in both channels for the same τ_a and α increase in both cases. On the contrary, the wavelength dependence of two channel radiances, i. e., the slope of two channel plot, is rather insensitive to the changes in mode radii. In order to understand this behavior, we introduce the linearized single scattering approximation of radiances in each channel as

$$L = \frac{\omega \tau P}{\mu}, \tag{3}$$

where μ, ω and P show the cosine of satellite zenith angle, the single scattering albedo and scattering phase function of the atmospheric layer, respectively. Values of P in the range of scattering angles ($\Theta = 75°$ - $150°$) used in most of the NOAA-11 satellite measurements increase with increasing contribution of small particles, which will be the reason for the increase in radiances with a decrease in mode radii. The wavelength dependence of radiances is mainly caused by the wavelength dependence of τ_a, which increases with increasing contribution of small particles in the test range of the radius change in Fig. 3. In case of fixed γ, a decrease in the mode radius is equivalent to an increase in the contribution of small particles, but it is not the case if α is fixed because γ has to be increased so as to keep α constant. Therefore, the expected change in the wavelength dependence in radiances are smaller in fixed-α cases than that in fixed-γ cases. This is another reason why we selected α for a size index rather than γ which is more directly related with the shape of the size distribution. Even though there is such an invariability, Fig. 3 indicates that the wavelength dependence of radiances for small α is sensitive to a change in the mode radius of the coarse mode.

On the other hand, the influence of increasing the dispersion of each mode is more complicated. The dispersion of the coarse mode does not affect noticeably on the radiances in the large particle limit, as well known in cloud remote sensing (e. g., Nakajima and King, 1990). It is interesting to see that the dispersion of the accumulation mode affects strongly the wavelength dependence of two channel radiances for all the α values. To understand this phenomenon, we have to note typical values for the size parameter of the accumulation mode

particles are 1.7 and 1.1 in the two channels, respectively, whereas the first maximum peak of the scattering efficiency factor as a function of size parameter is located around a size parameter of 4 for the refractive index assumed in this study (van de Hulst, 1957). This means the scattering efficiency decreases rapidly with decreasing size parameter. Even when we fix α, i. e., the wavelength dependence of τ_a, the wavelength dependence of the phase function will be caused in this process. Therefore, a difference in the dispersion of the accumulation mode size distribution makes a large change in the wavelength dependence of two channel radiances, because the size parameter range for integration of scattering cross section changes significantly with a wavelength change.

Preceding numerical experiments show that a tuning of size distribution parameters can change retrieved values of the Ångström exponent significantly. Note that a-values decrease from 0.8 to 0.4 for a given set of two channel radiances, for example, when we increase the mode radius of the coarse mode and decrease the dispersion of the accumulation mode.

5. 3. 2. 2 Calibration coefficients of AVHRR sensor

We will begin with the notations used in the calibration procedure. The spectral radiance L_i detected by channel-i is related with digital count C_i as follows,

$$L_i = S_i(C_i - C_{0,i}), \tag{4}$$

where $C_{0,i}$ is the deep space count and S_i is the calibration coefficient for channel-i. The sensor calibration is a serious problem in using satellite data, especially which are not calibrated

Table 2 Calibration coefficients and deep space counts for AVHRR-11 channel-1 and -2 in 1990.

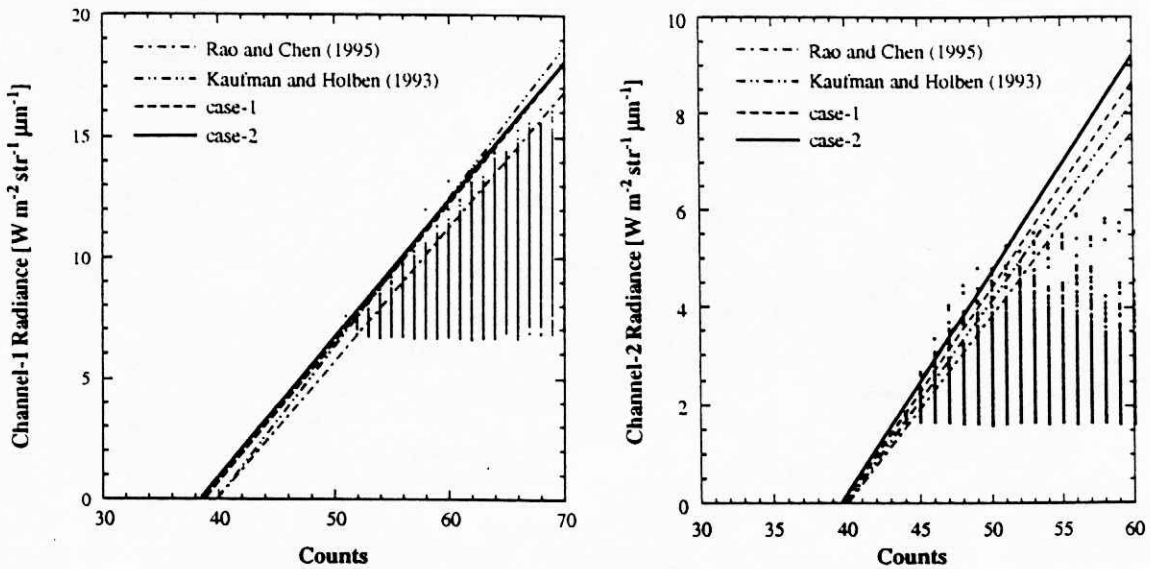| Source	S_1	$C_{0,1}$	S_2	$C_{0,2}$
Pre flight	0.492	40.000	0.356	33.930
Rao and Chen (1995)	0.56±0.01	40.000	0.38±0.01	40.000
Kaufman and Holben (1993)	0.59±0.02	40.000	0.41±0.02	40.000
Che and Price (1992)	0.580	—.—	0.394	—.—
this study case-1	0.578	38.750	0.425	39.750
this study case-2	0.570	38.388	0.450	39.625

Fig. 4 The relationhip between minmumm degital counts in NOAA-11 / AVHRR channel-1 and -2 in each segment data and corresponding theoretical values for the molecular atmosphere.

on board such as data in AVHRR channel-1 and -2. Some calibration coefficients for NOAA-11 channel1-1 and -2 are proposed by several researchers (Che and Price, 1992; Kaufman and Holben, 1993; Rao and Chen, 1995) as shown in Table 2. It is important to note the large variation in reported values. In order to determine calibration coefficients, we plot the minimum counts in each segment (a latitude-longitude box of 0.5° x 0.5°) versus theoretical values of the molecular atmosphere as shown in Fig. 4. It is found that the calibration coefficient and deep space counts may be determined by a linear regression of the minimum envelope of the plot, although the variation in the observed minimum digital counts is significantly large for such a linear regression, due to a small aerosol loading even with the minimum radiance pixels.

The calibration coefficients and deep space counts labelled 'case-1' are used in the previous analysis in Fig. 2 are determined as $S_1 = 0.578$, $C_{0.1} = 38.75$, $S_2 = 0.4255$, and $C_{0.2} = 39.75$, considering Fig. 4 and past investigations. Note that the calibration coefficients are similar to values by Kaufman and Holben (1993), but deep space counts are different, especially for channel-1. Although deep space counts are thought to be stable at 40, our retrieved results have a dependence on the solar zenith angle in case of fixed deep space counts at 40. Therefore, we have determined the deep space counts by a linear regression labelled 'case-1' in Fig. 4
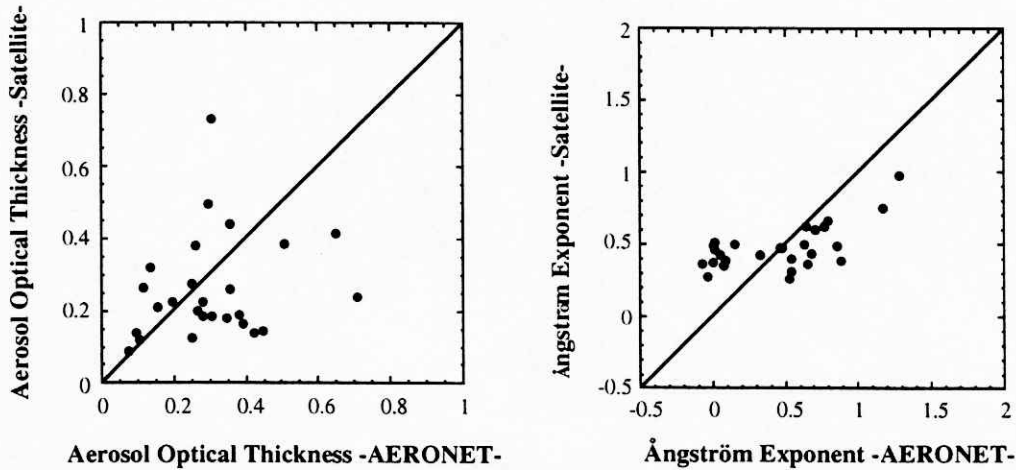
79

Fig. 5   Same as in Fig. 2, but with calibration constants 'case-2', $r_{m,1} = 0.17$, $r_{m,2} = 3.44$, $s_1 = 1.96$, and $s_2 = 2.37$ for bimodal size distribution, and complex refractive index of 1.5-0.005i.

keeping the slope unchanged. On the other hand, the calibration coefficients and deep space counts labelled 'case-2' have been simultaneously determined by linear regression as in Fig. 4. The results with this calibration constants are shown in Fig. 5 as same as Fig. 2. With increasing calibration coefficient for channel-2, radiances in channel-2 increase and, as a results, retrieved Ångström exponent values decrease regardless of the values.

The above discussion may suggest that a simultaneous tuning of the size distribution parameters and calibration constants may bring the retrieved Ångström exponent values close to the ground-based measurement values. If we adopt the calibration constants 'case-2', parameters of the size distribution should be modified so as to decrease α_{sat} corresponding to
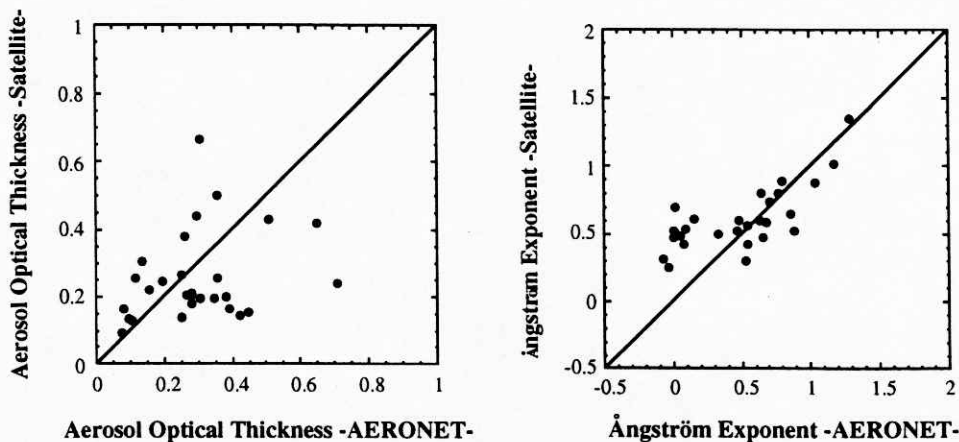

Fig. 6   Same as in Fig. 2, but with calibration constants 'case-2', $r_{m,1} = 0.17$, $r_{m,2} = 3.44$, $s_1 = 1.3$, and $s_2 = 2.75$ for bimodal size distribution, and complex refractive index of 1.5-0.005i.

80

large α_{gr} and to increase α_{sat} for small α_{gr}. Figure 3 suggests that such a tuning can be realized by decreasing $r_{m.1}$ or s_1 and increasing s_2. Figure 6 shows the results with calibration constants 'case-2' and tuned size distribution parameters, $r_{m.1} = 0.17$, $r_{m.2} = 3.44$, $s_1 = 1.3$, and $s_2 = 2.75$. Although α_{sat} for $\alpha_{gr} < 0.2$ are still overestimated by the present method, the agreement between them is improved as compared with Fig. 2.

5. 3. 2. 3 Complex refractive index

Other issue for improving the retrieval results is the assumption of complex refractive index. We assumed 1.5-0.005i for the aerosol complex refractive index, supposing the mean refractive index of absorbing and non-absorbing aerosols. In the NOAA phase-1 operational algorithm, the aerosol complex refractive index is assumed at 1.5-0.0i, whereas Ignatov et al. (1995) have pointed out that this value is not suitable and proposed 1.5-0.01i from a validation using sunphotometer measurements off the west coast of North Africa and in Mediterranean Sea. Moulin et al. (1997) also proposed 1.5-0.01i for desert aerosol model from comparison between Meteosat-derived and sunphotometer-derived aerosol optical thicknesses. On the other hand, the imaginary part of the complex refractive index for desert dust obtained by ground-based measurements is 0.005 ± 0.002 in the spectral range from 0.5 to 1.0 μm with some wavelength dependence (Sokolik et al., 1993; Patterson et al., 1977; Carlson and Caverly, 1977; Tomasi, C., V. Vitale and E. Caroli, 1983). The imaginary part of refractive index of Saharan dust has a sharp decrease and takes the minimum value around 0.6 to 0.7 μm and then slowly increases for longer wavelengths. According to this fact, it may be better to
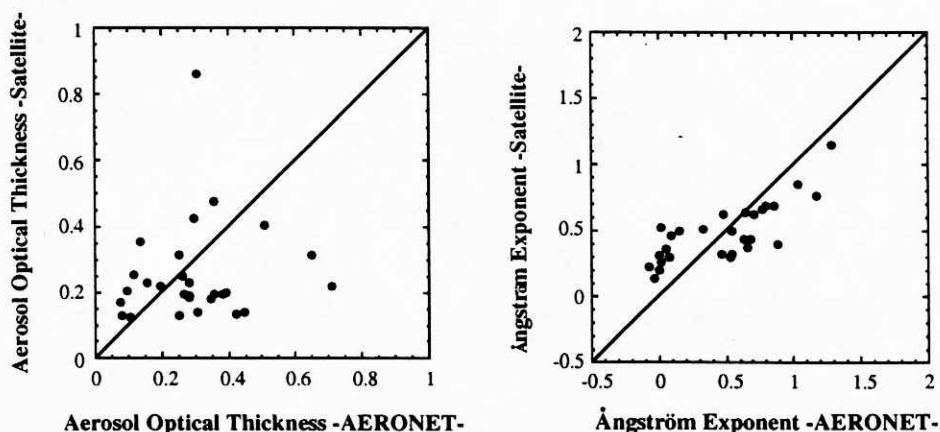

Fig. 7   Same as in Fig. 6 but with a complex refractive index 1.5-0.006i for channel-2.

assume an imaginary index for channel-2 larger than that for channel-1. Figure 7 shows the results with same parameters as in Fig. 6 but with an imaginary index for channel-2 as 0.006. The increase of the imaginary index for channel-2 improves the agreement of α_{sat} with $\alpha_{gr} <$ 0.2, whereas α_{sat} significantly underestimate $\alpha_{gr} > 0.2$. This experiment suggests that the retrievals are improved if the imaginary index in channel-2 is increased selectively for mineral dust aerosols. Neglecting the spectral dependence of the complex refractive index may be one of reasons of disagreement between satellite-derived and ground-based Ångström exponents for mineral dust practices.

5. 3. 3   A modified aerosol model

As a conclusion of discussion in the preceding sections, we adopted size distribution parameters as $r_{m.1} = 0.17$, $r_{m.2} = 3.44$, $s_1 = 1.3$, and $s_2 = 2.75$ and calibration constants 'case-2', which lead the results as shown in Fig. 6. In the present study we didn't assume a wavelength dependence in the imaginary index of refraction which is suggested in the discussion in Section 5.3.2.3, since it is difficult for us to introduce an automatic classification of mineral dust aerosols in the process of data analyses with only two channel radiances. It will be necessary to use more spectral channels to distinguish the aerosol types automatically. Recent or future sensors, such ADEOS / OCTS, SeaWiFS, EOS / MODIS, and ADEOS2 / GLI which have many spectral channels in visible and near infrared spectral regions, will make such a treatment possible.

5. 4   Global distributions of Ångström parameters

5. 4. 1   Overview

Figure 8 presents the global distributions of τ_a and α obtained from NOAA-11 / AVHRR with the present two channel retrieval algorithm in January, April, July, and October 1990. Note that as compared with the results of Higurashi and Nakajima (1997) the results show more detailed features of aerosol characteristics with longer averaging time and finer spatial resolution.

Distributions of τ_a in Fig. 8 show the most prominent contribution to the aerosol loading

January   **January**

April   **April**

July   **July**

October   **October**

0.0   0.5   1.0   0.1 0.5 1.0 1.5

Aerosol Optical Thickness at 0.5μm   **Ångström Exponent**
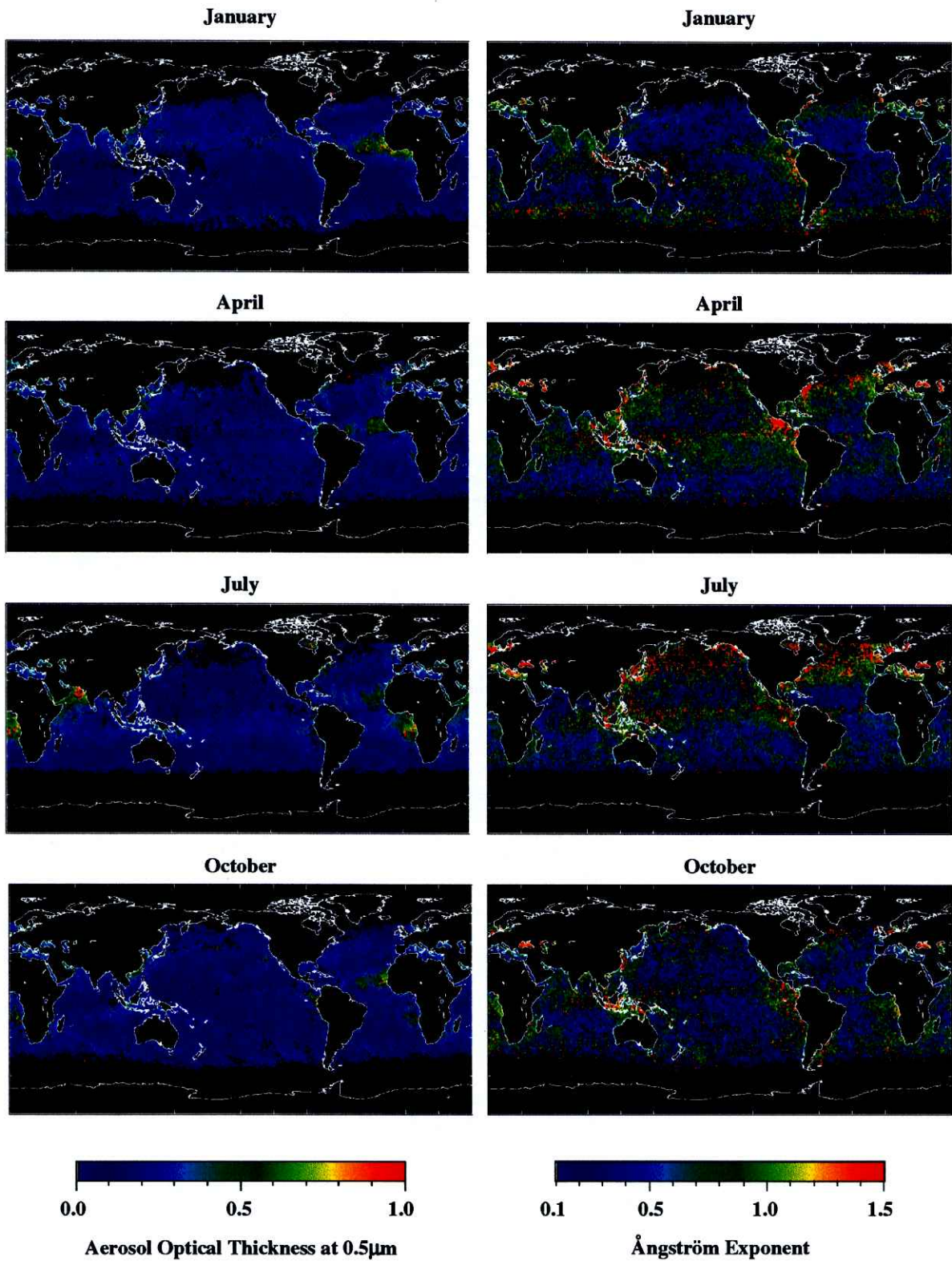
Fig. 8 Global Distributions of τ_a and α in January, April, July and October 1990.

83

is caused by mineral dust aerosols. We find a large quantity of mineral dust aerosols off the west coast of North Africa through the year and at the Arabian Sea in July. Saharan dust are transported over the North Atlantic Ocean through the trade wind, and reach the Caribbean Sea in July. Small α values in these regions consist with this fact, because a small α indicates a large contribution of coarse particles. Large τ_a are also found off the west coast of South Africa in July and October, and which are caused by an influence of biomass burning as Herman et al. (1997) pointed out from analyses of Nimbus-7 / TOMS (Total Ozone Mapping Spectrometer) data. A remarkable feature seen in the distributions of α is that large α appear in the northern middle latitudes, in which most anthropogenic aerosol emissions are concentrated, especially off the coast of east North America, Europe, and East Asia, in April and July. This seasonal dependence is reasonable since submicron accumulation mode particles are actively generated by gas-to-particle conversion processes in summer season in these regions. We also find large α in Central America in April. This phenomenon agrees with the fact that the biomass burning occurs in Central America in spring as reported by NASA space shuttle observation (Andreae, 1993).

5. 4. 2   Regional features of aerosol optical properties

To understand the aerosol optical properties further, we discuss seasonal variabilities of τ_a and α, and their correlation in each region illustrated in Fig. 1. Note these regions are same as in Huser et al. (1997). The regional monthly means of τ_a and α, in January, April, July, and October, and the four month averages are shown in Table 3.

5. 4. 2. 1   Open seas   (NE, NW, EC, WC & SE Pacifics; N Atlantic; S Indian Sea; New Zealand)

The variability of τ_a is small over open seas, especially in the Southern Hemisphere, as compared with in other regions, while α increases in spring and summer seasons. Correlations between τ_a and α in the regions 'SE Pacific', 'NW Pacific' and 'North Atlantic' are shown in Fig. 9. Figure 9(a) shows α initially increases with increasing τ_a and then decreases with further increase of τ_a exceeding 0.2 - 0.4 in spring and summer. The peak reaches a value close to 1. Since the atmosphere over the open sea is expected to be affected mostly by oceanic aerosols, the correlation patterns mentioned above may be caused by accumulation

Table. 3 Regional averages of satellite-retrieved aerosol optical thickness at 0.5 μm, τ_a, and Ångström exponent, α, in January, April, July, and October 1990.

| Reagion name	τ_a					α				
	Jan.	Apr.	Jul.	Oct.	ave.	Jan.	Apr.	Jul.	Oct.	ave.
Open Sea										
NE Pacific	0.18	0.19	0.13	0.19	0.17	0.41	0.71	0.80	0.57	0.58
NW Pacific	0.22	0.25	0.18	0.19	0.19	0.49	0.74	0.79	0.58	0.63
N Atlantic	0.19	0.23	0.20	0.19	0.20	0.68	0.94	1.00	0.60	0.77
EC Pacific	0.22	0.17	0.15	0.14	0.17	0.51	0.67	0.67	0.52	0.56
WC Pacific	0.22	0.14	0.12	0.10	0.14	0.35	0.63	0.73	0.56	0.55
SE Pacific	0.16	0.18	0.12	0.17	0.17	0.61	0.48	0.35	0.50	0.54
S Indian Sea	0.15	0.17	0.14	0.19	0.16	0.62	0.51	0.46	0.55	0.57
New Zealand	0.15	0.17	0.11	0.14	0.14	0.62	0.52	0.45	0.52	0.56
North America										
W US	0.16	0.16	0.15	0.20	0.17	0.49	0.90	0.73	0.52	0.58
E US	0.18	0.31	0.41	0.22	0.24	0.90	1.24	1.04	0.61	0.78
SE US	0.21	0.20	0.26	0.23	0.22	0.71	0.90	1.03	0.78	0.80
Central America										
C America	0.21	0.20	0.20	0.15	0.19	0.71	1.03	0.77	0.76	0.74
Caribbean	0.24	0.20	0.25	0.15	0.23	0.49	0.74	0.41	0.57	0.49
South America										
Peru	0.20	0.25	0.29	0.27	0.25	1.02	0.92	0.79	0.95	0.95
NE Brazil	0.34	0.29	0.21	0.20	0.25	0.46	0.62	0.63	0.57	0.56
E Brazil	0.11	0.18	0.15	0.17	0.15	0.43	0.60	0.70	0.54	0.60
Africa and Middle East										
W Africa	0.30	0.25	0.32	0.33	0.32	0.43	0.62	0.43	0.46	0.44
Guinea	0.48	0.34	0.34	0.24	0.37	0.37	0.60	0.59	0.69	0.55
SW Africa	0.18	0.23	0.40	0.26	0.28	0.48	0.68	0.57	0.73	0.58
SE Africa	0.13	0.20	0.19	0.28	0.20	0.51	0.62	0.68	0.77	0.68
Arabia	0.23	0.19	0.61	0.23	0.28	0.78	0.68	0.31	0.63	0.65
Asia										
Bengal	0.28	0.26	0.31	0.17	0.25	0.78	0.82	0.46	0.70	0.73
Indonesia	0.14	0.17	0.20	0.23	0.21	0.75	0.83	0.81	0.72	0.77
New Guinea	0.13	0.17	0.24	0.16	0.19	0.60	0.86	0.81	0.80	0.78
S Chian Sea	0.35	0.28	0.20	0.28	0.29	0.65	1.01	0.82	0.72	0.72
China	0.36	0.36	0.25	0.36	0.31	0.76	1.02	1.09	0.86	0.92
Japan	0.24	0.27	0.23	0.21	0.22	0.51	0.92	1.12	0.55	0.68
Europe										
W Europe	0.16	0.30	0.21	0.17	0.18	0.78	0.86	0.82	0.54	0.72
NW Europe	0.14	0.34	0.29	0.19	0.24	0.90	1.04	1.26	0.67	0.96
Mediterranian	0.21	0.27	0.29	0.29	0.26	0.86	0.99	1.11	0.59	0.85
Black Sea	0.19	0.36	0.43	0.33	0.34	1.11	1.35	1.61	1.32	1.40
Caspian	0.21	0.30	0.40	0.21	0.27	1.03	1.38	1.18	1.02	1.11
N.Hemisphere	0.23	0.21	0.21	0.18	0.20	0.55	0.76	0.74	0.60	0.63
S.Hemisphere	0.14	0.18	0.18	0.17	0.17	0.57	0.61	0.56	0.57	0.59
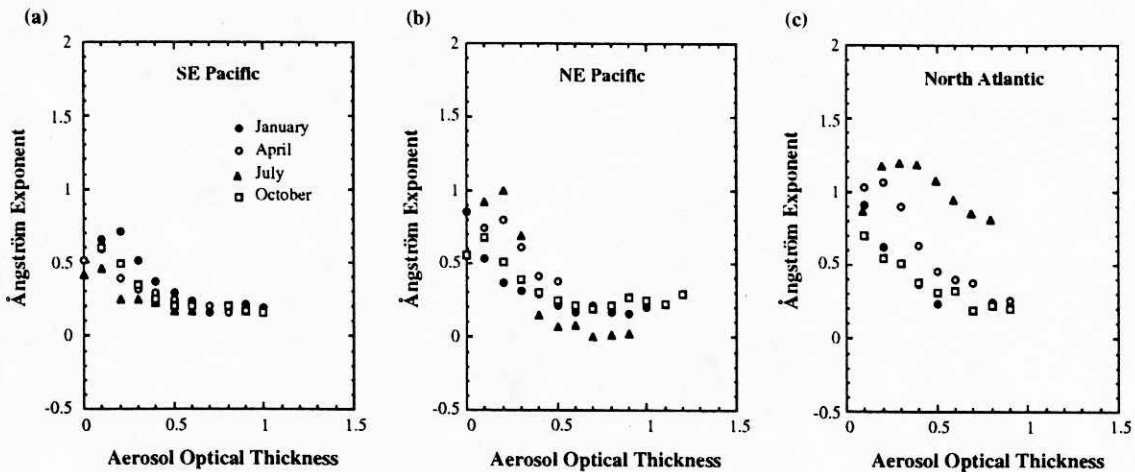
Fig. 9   Correlation patterns between τ_a and α in South East Pacific (a), North East Pacific (b), and North Atlantic (c) as illustrated in Fig. 1.

and growth processes of sulfate particles generated by ocean biological activities. Actually, gas-to-particle conversion and accumulation process of aerosols cause an increase in both τ_a and α, i.e., a positive correlation, whereas a growth process of aerosols absorbing water vapor causes an increase in τ_a and α decrease in a , i.e., a negative correlation (Nakajima et al., 1989; Kaufman and Holben, 1996). A typical α value associated with those processes is around 1. On the other hand, the broad negative correlation with small α values in Fig. 9 may be attributed to the growth process of sea-salt particles. Typical sea-salt particles are much larger than gas-to-particle conversion aerosols, and are associated with a values close to 0 (Gordon and Wang, 1994).

An influence of anthropogenic aerosol emissions also may not be ignored, however, over the open sea in the Northern Hemisphere, especially in the North Atlantic Ocean, as suggested by the fact that τ_a and α in the Northern Hemisphere are larger than in the South Hemisphere. The seasonal variability of τ_a is different from that in the same regions obtained by Huser et al. (1997), which has the maximum in summer and the minimum in winter, as shown in Table 3. This difference may be caused by the difference in α in summer and winter from the fixed value of α used in the NOAA algorithm, i.e., ~1.0.

5. 4. 2. 2   North America, Europe, and East Asia

In East America, Europe, and East Asia, where strong sources of anthropogenic pollutant
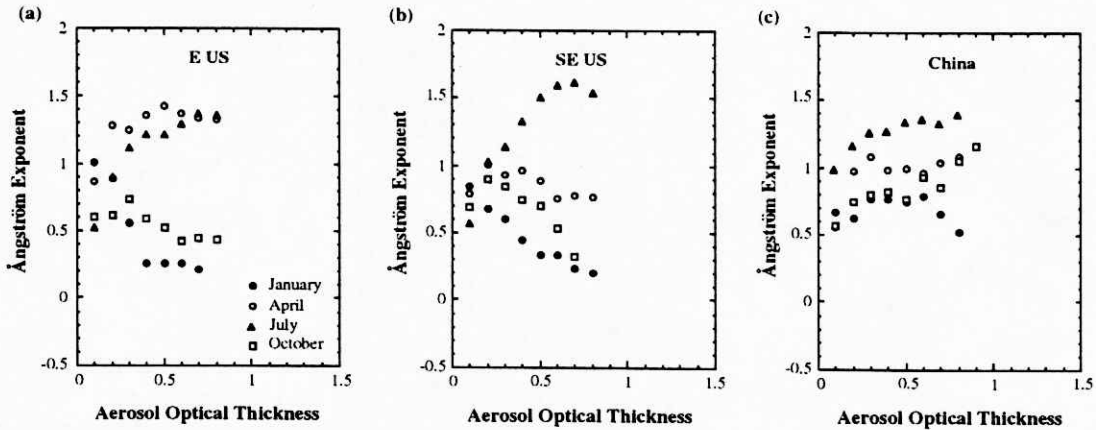
86

Fig. 10 Same as in Fig. 9 but for the regions 'E US' (a), 'SE US' (b), and 'China' (c).

exist, both τ_a and α remarkably increase in spring and/or summer as shown in Fig. 10. In this case, α reaches a value as large as 1.5. This suggests a strong activity of an accumulation process in these regions. On the other hand, the correlation between τ_a and α in areas such as East America, West Europe, and Japan in winter is similar to that of the open sea. The correlation in conspicuously polluted areas, such as China, Black Sea, and Caspian Sea, is similar at all seasons suggesting an accumulation process is dominant through the year.

5. 4. 2. 3 Africa and Middle East

The impact of Saharan dust is significant over a large portion of the North Atlantic Ocean with long distance transportation by trade wind. Figure 11 shows that τ_a of West Africa is constantly large throughout the year, while α takes almost a constant value about 0.5, which is characteristically small reflecting the large loading of desert dust. Such a characteristic relationship between τ_a and α has been observed by ground-based sunphotometry (Nakajima et al., 1989). The position of the Saharan dust plume shifts from south to north with the seasonal march of ITCS (Intertropical Convergence Zone) from winter to summer. This is one of the reasons why τ_a of Gulf of Guinea increases in January as shown in Table 3. Another reason for the increase in τ_a will be an influence of biomass burning. It is reported that fires were observed by the DMSP (Defense Meteorological Satellite Program) imagery in the savannas south of the Sahara desert (Cahoon et al., 1992). Also, Cahoon et al. (1992) showed that from July to October the fire activity moves from west to east of South Africa. This seasonal change in fire locations seems to be consistent with the characteristic increase of τ_a
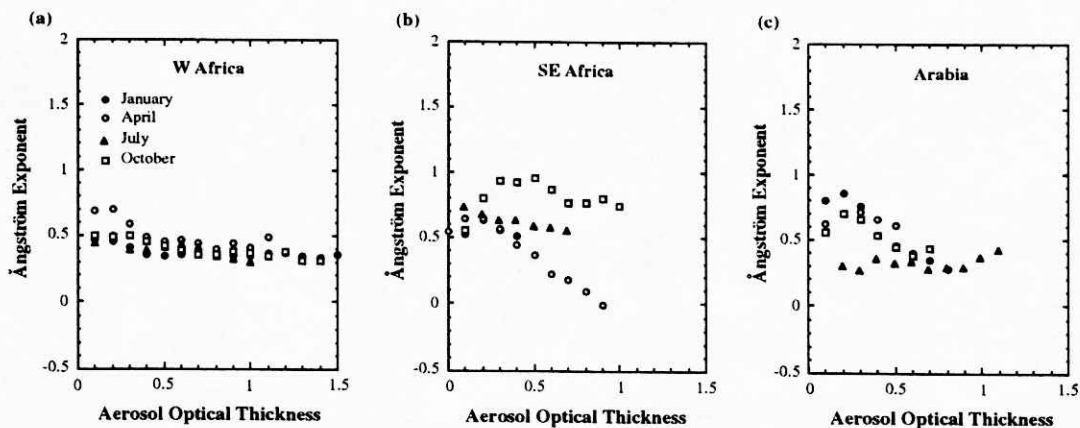
87

Fig. 11   Same as in Fig. 9 but for the regions 'W Africa' (a), 'SE Africa' (b), and 'Arabia' (c).

and α in region 'SE Africa' in October (Fig. 11(b), Table 3) suggesting a generation of small accumulation mode particles. Figure 11 clearly shows that the aerosol properties over the Arabian Sea in July is different from others, indicating mineral dust aerosols becomes dominant, taking the place of anthropogenic or oceanic aerosols.

5. 4. 2. 4   Central and South America

In April, we find conspicuously large α in Central America which can be explained by an influence of biomass burning from the distribution of fires seen from space (Andreae, 1992) and the analyses of UV-absorbing aerosols using TOMS (Herman et al., 1997). It is difficult to attribute the large α to industrial aerosols since TOMS does not sense sulfate aerosols,
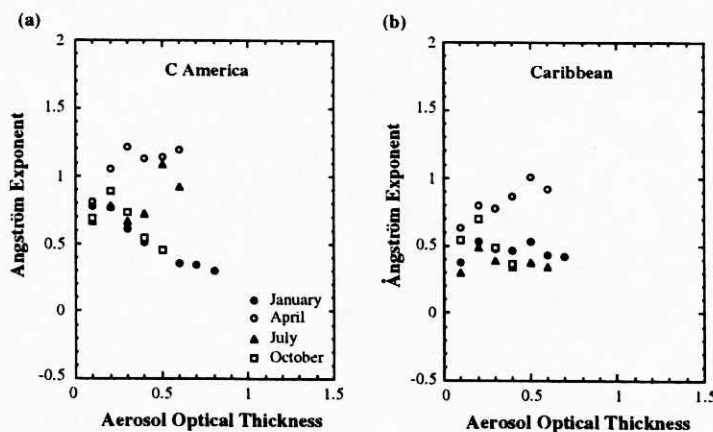

Fig. 12   Same as in Fig. 9 but in the regions 'C America' (a) and 'Caribbean' (b).

88

which do not absorb UV radiation significantly. Such an agreement of aerosol classification by τ-α correlation pattern and TOMS UV absorbing aerosol distributions is also found in the Caribbean Sea shown in Fig. 12, where both methods suggest that this region is influenced by Saharan dust transported with the trade wind.

5. 4. 3 Zonal mean of τ_a and α

The zonal mean values of τ_a and α for each month are shown in Fig. 13. Some peaks of τ_a appear in the low latitude zone between 20°S - 20°N, where there are large deserts and many biomass burning areas. Another peaks occur in the high latitude zone to the north of 40°N, where there are sources of anthropogenic aerosol emission from industrial areas. τ_a in the polluted zone increase strongly reaching a value as large as 0.25, in spring and summer. The average of τ_a in the Northern Hemisphere is larger than that in the Southern Hemisphere by about 0.05. As compared with τ_a, α stay in a relatively narrow range around 0.5 in most of latitudes other than northern high latitudes. The most interesting observation in the zonal
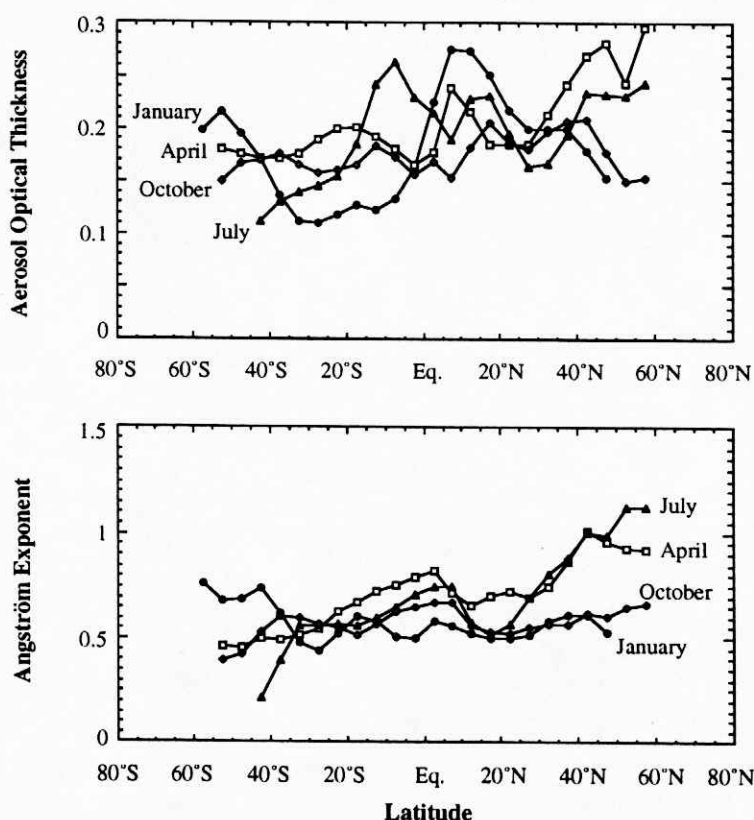

Fig. 13 Latitudal zonal mean profiles of Ångström parameters as a function of latitude.

mean profiles of α is its seasonal variations in the tropical zone between 20°S - 20°N and the high latitude zone to the north of 40°N. α as well as τ_a, remarkably increases in the high latitude zone in spring and summer when a gas-to-particle conversion process is expected to be dominant. The zonal mean of α in the tropical zone tends to have a peak around the equator and its pattern is different from that of τ_a. Both τ_a and α increase in July in the southern part of the zone, whereas τ_a increases and α decreases in January in the northern part of the zone. These characteristic seasonal changes indicate a difference in the dominant source for the peaks in the tropical zone. The northern peak of τ_a may be caused by mineral dust aerosols, whereas the southern peak caused by biomass burning aerosols. The increase of τ_a and α in January in the zone to the south of 30°N may be also caused by biological activities, as suggested by Chin et al. (1996).

5. 5 Discussion and Conclusions

A validation study of our aerosol retrieval algorithm, which retrieves the aerosol optical thickness and Ångström exponent from NOAA/AVHRR channel-1 and -2 radiance data, has been made by comparison with ground-based measurement data, which are selected from AERONET sunphotometry data set. We first observed that our retrieved Ångström exponents largely overestimate the ground-based values when the ground-based values are smaller than 0.2 corresponding to mineral dust aerosols. We modified parameters not only for size distribution but also for sensor calibration to improve such overestimation. As a result, satellite-retrieved values of α are decreased coming close to the ground-based values with a slight overestimation. It is also found a further improvement may be possible by assuming a wavelength dependent imaginary index of refraction. Such an experience suggests that it is difficult to find a simple model to approximate various aerosol optical properties for global scale remote sensing of aerosols only by changing the peak ratio of bimodal size distribution with fixed mode radii and dispersions. We need further investigation to fully understand the problem.

We obtained global distributions of aerosol optical thickness and Ångström exponent in January, April, July, and October 1990 with the modified aerosol model and sensor calibration constants. The most prominent aerosol layers detected from space are of mineral dust and biomass burning aerosols. Analyses of distribution patterns of τ_a and α have shown that they

90

spread over large areas with long-distance transportation of several thousand kilometers. Although not significant in the optical thickness distribution, the Ångström exponent distribution has clearly given us an evidence for aerosols originated from industrial activities in the northern middle latitudes and oceanic biological activities over open sea areas. Aerosols from industrial sources certainly have an impact on the atmospheric condition in the Northern Hemisphere, especially in middle latitudes in spring and summer. The influence of biological activities on generating aerosols is evident by an increase of Ångström exponent in the high-latitudinal southern ocean in January. As mentioned above, seasonal variation of the Ångström parameters and correlation between them are thus useful for identifying aerosols from various sources.

A long-term data analyses of NOAA AVHRR radiances with the present algorithm will make a large contribution to studies of the climate forcing of aerosols. The knowledge of aerosol size distribution is important for calculating the number of aerosols, and hence, for estimating single scattering albedo and cloud - aerosol interaction. Extension of our method to multichannel radiances from ocean color sensors, such as NUMBUS-7 / SeaWiFS, ADEOS / OCTS and SeaWiFS which have many channels in visible and near infrared spectral regions, will be another challenge we have to make in near future to widen our knowledge on aerosol impacts on the earth's climate.

References

Andreae, M. O., 1993: Global distribution of fires seen from space. *EOS Trans.*, **74**, 129-144.

Cahoon, Jr, D. R., B. J. Stocks, J. S. Levine, W. R. Cofer III, and K. P. O'Neill, 1992: Seasonal distribution of African savanna fires. *Nature*, **359**, 812-815.

Carlson, T. N. and R. S. Caverly, 1977: Radiative characteristics of Saharan dust at solar wavelengths. *J. Geophys. Res.*, **82**, 3141-3152.

Charlson, R. J., S. E. Schwartz, J. M. Hales, R. D. Cess, J. A. Coakley, Jr., J. E. Hansen, D. J. Hofmann, 1992: Climate forcing by anthropogenic aerosols. *Science*, **25**, 426-430.

Che, N. and J. C. Price, 1992: Survey of radiometric calibration results and methods for visible and near infrared channels of NOAA - 7, -9, and -11 AVHRRs. *Remote sens. Environ.*, **41**, 19-27.

Chin, M., D. J. Jacob, G. M. Gardner, M. S. Foreman-Fowler, P. A. Spiro, and D. L. Savoie, 1996: A global three-dimensional model of tropospheric sulfate. *J. Geophys, Res.,* **101**, 18667-18690.

Durkee, P. A., F. Pfeil, E. Frost and R. Shema, 1991: Global analysis of aerosol particle characteristics. *Atmos. Environ*, **25A**, 2457-2471.

Gordon, H. R., and M. Wang, 1994: Retrieval of water - leaving radiance and aerosol optical thickness over the oceans with SeaWiFS: A preliminary algorithm. *Appl. Opt.*, **33**, 443-452.

Herman, J. R., P. K. Bhartia, O. Torres, C. Hsu, C. Seftor, and E. Celarier, 1997: Global distribution of UV-absorbing aerosols from Nimbus 7 / TOMS data. *J. Geophys. Res.*, **102**, 16911-16922.

Higurashi, A., and T. Nakajima, 1997: Development of a two channel aerosol retrieval algorithm on global scale using NOAA / AVHRR. *J. Atmos. Sci. Accepted.*

Higurashi, A., T. Nakajima, and T. Tanaka, 1997: A study on synthesizing satellite-received radiances for aerosol and ocean color remote sensing. *Submitting to Appl. Opt.*

Holben, B. N., T. F. Eck, I. Slutsker, D. Tanré, J. P. Buis, A. Setzer, E. Vermote, J. A. Reagan, Y. J. Kaufman, T. Nakajima, F. Lavenu, I. Jankowiak, and A. Smirnov, 1997: Automatic sun and sky scanning radiometer system for network aerosol monitoring. *Submitted to Remote Sens. Environ.*

IPCC95, Climate Change 1995, The science of climate change, Eds. J. T. Houghton et al., Cambridge Univ. Press., 1996.

Ignatov, A. M., L. L. Stowe, S. M. Sakerin, and G. K. Korotaev, 1995: Validation of the NOAA/ NESDIS satellite aerosol product over the North Atlantic in 1989. *J. Geophys. Res.*, **100**, 5123-5132.

Kaufman, Y. J. and B. N. Holben, 1993: Calibration of the AVHRR visible and near-IR bands by atmospheric scattering, ocean glint and desert reflection. *Int. J. Remote Sensing*, **14**, 21-52.

Kaufman, Y. J. and B. N. Holben, 1996: Hemispherical backscattering by biomass burning and sulfate particles derived from sky measurements. *J. Geophys. Res.,* **101**, 19433-19445.

Kaufman, Y. J. and T. Nakajima, 1993: Effect of Amazon smoke on cloud microphysics and albedo - analysis from satellite imagery. *J. Appl. Meteor.*, **32**, 729-744.

Kiehl, J. T., and B. P. Briegleb, 1993: The relative role of sulfate aerosols and greenhouse gases in climate forcing. *Science*, **260**, 311-314.

Li, X., H. Maring, D. Savoie, K. Voss, and J. M. Prospero, 1996: Dominance of mineral dust in aerosol light-scattering in the North Atlantic trade winds. *Nature*, **380**, 416-419.

Mitchell, J. F. B., T. C. Johns, J. M. Gregory, and S. F. B. Tett, 1995: Climate response to increasing levels of greenhouse gases and sulphate aerosols. *Nature*, **376**, 501-504.

Moulin, C., F. Dulac, C. E. Lambert, P. Chazette, I. Jankowiak, B. Chatenet, and F. Lavenu, 1997: Long-term daily monitoring of Saharan dust load over ocean using Meteosat ISCCP-B2 data 2. Accuracy of the method and validation using sun photometer measurements. *J. Geophys. Res.*, **102**, 16959-16969.

Nakajima, T., and M. D. King, 1990: Determination of the optical thickness and effective radius of clouds from reflected solar radiation measurements. Part I: Theory. *J. Atmos. Sci.*, **47**, 1878-1893.

Nakajima, T., and A. Higurashi, 1997: AVHRR remote sensing of aerosol optical properties in the Persian Gulf region, the summer of 1991. *J. Geophys. Res.*, **102**, 16935-16946.

Nakajima, T., M. Tanaka, M. Yamano, M. Shiobara, K. Arao and Y. Nakanishi, 1989: Aerosol optical characteristics in the yellow sand events observed in May, 1982 in Nagasaki - Part II Model, *J. Meteor. Soc. Japan*, **67**, 279-291, 1989.

Nakajima, T., G. Tonna, R. Rao, Y. Kaufman, and B. Holben, 1996: Use of sky brightness measurements from ground for remote sensing of particulate polydispersions. *App. Opt.*, **35**, 2672-2686.

Patterson, E. M., D. A. Gillette, and B. H. Stockton, 1977: Complex index of refraction between 300 and 700 nm for Saharan aerosols. *J. Geophys. Res.*, **82**, 3153-3160.

Rao, C. R. N. and J. Chen, 1995: Inter-satellite calibration linkages for the visible and near-infrared channels of the Advanced Very High Resolution Radiometer on the NOAA-7, -9, and -11 spacecraft. *Int. J. Rem. Sens.*, **16**, 1931-1942.

Santer, B. D., K. E. Taylor, T. M. L. Wigley, T. C.Johns, P. D. Jones, D. J. Karoly, J. F. B. Mitchell, A. H. Oort, J. E. Penner, V. Ramaswamy, M. D. Schwarzkopf, R. J. Stouffer, and S. Tett, 1996: A search for human influences on the thermal structure of the atmosphere. *Nature*, **382**, 39-46.

Sokolik, I. N., and O. B. Toon, 1996: Direct radiative forcing by anthropogenic airborne mineral aerosol. *Nature*, **381**, 681-683.

Sokolik, I., A. Andronova, and T. C. Johnson, 1993: Complex refractive index of atmospheric dust aerosols. *Atmos. Environ.*, **16**, 2495-2502.

Stowe, L. L., R. M. Cavoy, and P. P. Pelliguino, 1992: Monitoring the Mt. Pinatubo aerosol layer with NOAA-11 / AVHRR data. *Geophys. Res. Lett*, **19**, 159-162.

Taylor, K. E., and J. E. Penner, 1994: Response of the climate system to atmospheric aerosols and greenhouse gases. *Nature*, **369**, 734-737.

Tegen, I., A. A. Lacis, and I. Fung, 1996: The influence on climate forcing of mineral aerosols from disturbed soils. *Nature*, **380**, 419-422.

Tomasi, C., V. Vitale and E. Caroli, 1983: Sahara dust program - II. Determination of the vertical particulate mass loading by using extinction models based on Junge-type size distributions. *J. Aerosol Sci.*, **14**, 529-539.

Twomey, S. A., M. Piepgrass and T. L. Wolfe, 1984: An assessment of the impact of pollution on global cloud albedo. *Tellus*, **36B**, 356-366.

van de Hulst, H. C., 1957: Light scattering by small particles. 470pp., Dover, New York.

Chapter 6

General Conclusion

6 General Conclusion

An algorithm for retrieving global aerosol properties from satellite data has been developed. This algorithm consists of two components: one is a look-up table algorithm of satellite-received radiances, and another is a retrieval algorithm of the Ångström parameters, i. e., aerosol optical thickness at wavelength of 0.5 μm and Ångström exponent, from two channel radiances of AVHRR radiometer.

For synthesizing satellite-received radiances, a decomposition of the total radiance into single and multiple scattering components is effective for reducing the angular dependence of coefficients for tabulation. Furthermore, it is effective for reducing the look-up table size to decompose radiances into components of aerosol, Rayleigh and specular reflection of solar direct radiation by rough ocean surface. We have studied the accuracy of synthesizing methods of the aerosol multiple scattering component by a polynomial function of aerosol optical thickness or linearized single scattering radiance. Although those methods are accurate for most angular geometries of remote sensing applications, the accuracy of synthesis is getting worse rapidly as solar and satellite zenith angles increase. In stead of those traditional formulae, it is suggested that the multiple scattering component can be synthesized by an exact single scattering solution with a polynomial function of aerosol optical thickness and an exponential correction term. This formula does not need higher order polynomial functions of aerosol optical thickness to reproduce the same accuracy for the angular geometries of $\theta + \theta_0 \le 125°$ as compared with the traditional formulae. A decomposition of the Rayleigh multiple scattering component make it easy to take into account the polarization effect in satellite-received radiances. On the other hand, a decomposition of the specular reflection of direct solar radiation by the rough ocean surface, by which the dependence of surface wind velocity of satellite-received radiances is mainly caused, makes other components insensitive to the wind velocity. Moreover, correction formulae of gaseous absorption has been proposed, especially for NOAA / AVHRR channel-2, in which strong water vapor absorbing bands are included. Correction for ozone absorbing effect is expressed by a simple two way transmittance because ozone exists in the upper atmosphere, while correction factors for water vapor

absorbing are tabulated because of its more complicated influence.

An algorithm for retrieving the aerosol optical thickness and Ångström exponent over the ocean is developed, making the maximum use of the synthesizing algorithm as mentioned above. This algorithm has been applied to NOAA-11 / AVHRR data for four months in 1990, i.e., January, April, July, and October. A validation of the results has been made by comparison with AERONET ground-based sunphotometry data. Even though the dispersion of the correlation is large, especially for aerosol optical thickness due to disagreement of the analyzed period, they are consistent with each other except for small Ångström exponent values ($\alpha < 0.2$) corresponding to cases of mineral dust aerosols. It is found that a tuning of parameters for aerosol size distribution and calibration constants can improve the agreement in such cases. It is also suggested that the wavelength dependence of imaginary index of refraction is important for successful retrievals of α for mineral dust aerosols. This issue has to receive more attention with careful validation.

Global distributions of the aerosol optical thickness and Ångström exponent obtained by the algorithm with modified parameters show that these Ångström parameters are very useful for sensing aerosols of various types such as of soil-derived, biomass burning, industrial pollutant, and ocean biological activities. Largest aerosol loading is made by mineral dust aerosols and biomass burning aerosols, that have a strong spatial and temoral homogeneities. Although the loading of industrial pollutant aerosols is found to be considerably smaller than that of mineral dust and biomass burning aerosols, the Ångström exponent is useful to study such thin anthropogenic aerosol distributions . In the Northern Hemisphere, especially middle latitudes, where there are many anthropogenic aerosol sources, the aerosol optical thickness and Ångström exponent remarkably increase in spring and summer. Another interesting observation in the Ångström parameter distributions is a signature of oceanic aerosols. The characteristic correlation patterns of the optical thickness and Ångström exponent over open sea areas suggests existence of that sea-salt aerosols and small sulfate aerosols generated from biological activities. Since such a τ- α correlation pattern cannot distinguish oceanic aerosols from anthropogenic aerosols brought over open seas by long-distant transportation, further studies will be needed to confirm this suggestion. It is also found that the aerosol optical thickness retrieved by NOAA operational algorithm may largely underestimate the optical thickness at wavelength of 0.5 μm over open ocean areas where the Ångström exponent

is much smaller than the one assumed by the NOAA algorithm ($\alpha \sim 1$).

Present and future analyses with the two channel algorithm will make a significant contribution in many ways to the study of the role of aerosols in the earth's climate. A long-term analyses of AVHRR satellite data by this algorithm will give us significant knowledges, for exmaple, on the spatial and temporal variabilities of aerosols of various types, the long-term trend of anthropogenic aerosols, and so on. Moreover, the knowledge of size distribution, which make it possible to estimate the column number of aerosol particles, will improve our knowledge on the aerosol-cloud interaction, of which climate effect is most unknown in the present climate modeling.